

UC Berkeley

UC Berkeley Electronic Theses and Dissertations

Title

Characterization of Cementitious Materials with Synchrotron-Radiation-Based Nanoprobes

Permalink

<https://escholarship.org/uc/item/67p0s4w6>

Author

Geng, Guoqing

Publication Date

2017

Peer reviewed|Thesis/dissertation

Characterization of Cementitious Materials with
Synchrotron-Radiation-Based Nanoprobes

By
Guoqing Geng

A dissertation submitted in partial satisfaction of the
requirements for the degree of
Doctor of Philosophy
in
Engineering - Civil and Environmental Engineering
in the
Graduate Division
Of the
University of California, Berkeley

Committee in charge:

Professor Paulo J. M. Monteiro, Chair
Professor Claudia P. Ostertag
Professor Hans-Rudolf Wenk

Spring 2017

Abstract

Characterization of Cementitious Materials with Synchrotron-Radiation-Based Nanoprobes

by

Guoqing Geng

Doctor of Philosophy in Civil and Environmental Engineering

University of California, Berkeley

Professor Paulo J.M. Monteiro, Chair

Portland cement (PC) based concrete is the second most consumed commodity after water, and is the foundation of modern construction industry. The present status of the cement and concrete industry is unsustainable: the production of Portland cement (PC) accounts for ~8% of global anthropogenic CO₂ emissions and the deterioration of existing reinforced concrete infrastructure is a constant, environmentally and economically costly problem. Optimizing the existing technology requires a breakthrough in the understanding of the cement hydration mechanisms, and in the structure-property correlation of the hydration products, especially at nano and atomistic scale. However despite decades of study, mechanisms underlying the cement hydration and all-stage performance remain unclear to a large extent, mainly due to the lack of experimental data at the fundamental level.

The aim of this dissertation is to provide new evidence to clarify unsolved questions along the service life timeline of PC concrete, using novel experimental methods that are based on synchrotron radiation. Three specific topics at distinct stage of concrete service life are investigated: 1) at early age the hydration mechanism of tricalcium aluminate (C₃A) in the presence of gypsum. C₃A is the most reactive clinker phase of PC whose rapid hydration greatly controls the workability of fresh concrete mixes, yet more evidence is needed to understand how C₃A hydration is retarded by gypsum; 2) at mature age, the composition-structure-property correlation of calcium (alumino)silicate hydrates (C-(A-)S-H). C-(A-)S-H is the dominant binding phase of PC concrete, and therefore determines the mechanical property and volumetric stability of modern concrete infrastructure. It is hierarchically porous down to single-nanometer, making it rather difficult to experimentally probe the intrinsic mechanical properties of pore-free C-(A-)S-H; 3) at late age, the microstructure and chemistry of hydrated tricalcium silicate (C₃S). C₃S is the major clinker phase in PC and is the major source for the creation of C-S-H. Its chemistry and structure have been extensively studied for the first few months of hydration, but the long-term (beyond 10 years) characterization is rarely done.

The research reported in the present dissertation uses synchrotron-radiation-based characterizing techniques to provide multi-scale evidence to answer the above mentioned questions. In-situ Wide and Small Angle X-ray Scattering, X-ray spectromicroscopy coupled with the single-nanometer resolved X-ray Ptychography imaging tool, and nano-

scale 3D Tomography are used, to investigate the dissolution-precipitation front of partially hydrated C_3A particles. The crystal-chemistry and 3D-morphology of the hydration products are quantified. Ettringite is found to be the only stable phase during the induction period. Regardless of the water to cement ratio, ettringite needles grow to a maximum length of 1-2 μm . Ettringite crystallization is not homogeneous on the C_3A surface, and the crystallization rate depends on the amount of relative surface site. Surface of pores/cavities inside the anhydrous C_3A particles contributes significantly to the hydration reaction, as soon as the dissolution connects them with the solution.

The knowledge of both the properties of the (pore-free) material at fundamental scale, and the multi-scale pore structure, are critical to the theoretical prediction of the macro-scale properties of concrete. Here, high pressure X-ray diffraction is utilized to study the anisotropic nanomechanical property of C-(A-)S-H, by tracking the response of the nanocrystal lattice to hydrostatic pressure up to ~ 10 GPa. For the first time, the nanomechanical properties of pore-free C-(A-)S-H are investigated as a function of chemistry and atomic configuration. The experimental results show that, contrary to the predictions of most molecular simulations, the stiffness of C-S-H increases along with its bulk Ca to Si molar ratio (Ca/Si). Under hydrostatic pressure, the c -axis (perpendicular to the layer structure) deforms much more readily, compared with the a - and b -axis (i.e. the in-plane directions of the layer structure). The densification of the interlayer spacing significantly decreases the incompressibility along the c -axis, and thus increases the overall bulk modulus. When Al is incorporated, the Al-induced crosslinking of adjacent dreierketten chains increases the stiffness of C-(A-)S-H. Molecular simulations in this dissertation unveil the atomistic mechanism for the C-S-H deformation, that the in-plane deformation of the silicate tetrahedra chain is through rigid rotation instead of the shortening of the stiff Si-O bond. Therefore neither the vacancies nor the Al incorporation in the silicate chain, alters the in-plane stiffness of C-(A-)S-H layer structure.

Lastly, Scanning Transmission X-ray Microscopy is integrated with conventional methods (lab XRD, SEM, TEM and NMR) to study the composition and structure of a late age (50 years) hydrated C_3S paste. After 50 years of curing, the mean chain length (MCL) of the C-S-H is 4.18, and the XRD reveals no resolved diffraction peaks for C-S-H. This indicates that the crystallization of C-S-H under ambient condition is negligible during concrete service life. Although the average Ca/Si of the C-S-H is ~ 1.7 , much higher than that of tobermorite (0.67-0.8) but closer to that of jennite (1.5), the coordination environment of Ca in C-S-H is similar to that of tobermorite rather than jennite.

The results in this dissertation enhance the understanding of cement chemistry, as well as provide direct validation to existing cement hydration modelling and molecular level C-(A-)S-H modelling. The work also develops protocols for systematically studying modern construction material using innovative synchrotron-radiation-based methods.

Table of Contents

1. Introduction	1
1.1 Challenges of cement industry for the new century	1
1.2 Synchrotron-radiation-based experiment methods applied to cementitious materials	3
1.3 Contents of this thesis	7
1.4 References	8
2. Existing results and open questions – a short literature survey	12
2.1 Early age – C ₃ A hydration in the presence of gypsum	12
2.2 Mature age – the chemistry-structure-property correlation of C-S-H	13
2.3 Mature age – influence of Al-incorporation on the nanomechanical property C-A-S-H	15
2.4 Late age - microstructural study of a 50-year-old hydrated C ₃ S paste	16
2.5 References	17
3. Materials and Methods	23
3.1 Materials	23
3.2 Experimental methods	25
3.3 References	28
4. Early-age hydration mechanism of cubic C ₃ A in the presence of gypsum	30
4.1 In-situ chemistry and crystallography of the initial hydration of C ₃ A in the presence of gypsum	30
4.2 Spectromicroscopy of C ₃ A hydrated in the presence of gypsum during the induction period	32
4.3 Meso-scale morphological evolution of solid hydration products using X-ray ptychographic imaging and in-situ SAXS	33
4.4 3D morphology of C ₃ A hydrated in the presence of gypsum during the induction period	36
4.5 Discussion and conclusions	38
4.6 References	39
5. Chemistry-structure-property correlation of C-S-H at atomistic scale	42
5.1 Ambient pressure XRD	42
5.2 High pressure XRD	44
5.3 Atomistic simulations	47
5.4 Discussions and conclusions	51
5.5 References	53
6. Influence of Aluminum incorporation to the mechanical property to C-A-S-H	55
6.1 XRD and ptychography at ambient pressure	55
6.2 High pressure XRD	57
6.3 Discussions and Conclusion	62
6.4 References	63
7. A nano- and micro-structural study of a 50-year-old hydrated C ₃ S paste	65
7.1 XRD	65

7.2	SEM.....	66
7.3	TEM	68
7.4	NMR.....	70
7.5	STXM.....	72
7.6	Discussions.....	78
7.7	Conclusion.....	80
7.8	References	81
8.	Concluding remarks	84
9.	Appendix	85

Acknowledgement

Five years ago I was hesitating between continuing my study in China and pursuing a Ph.D. degree in a foreign university. My wife, Zihan, decisively pushed me to apply for the graduate program in CEE of UC Berkeley. Three years ago after her own graduation, she came to Berkeley and began to take great care of our life until today. Without her courage, perspective and great sacrifice, I could never accomplish, or even start this Ph.D. program. I'd like to give my thanks to Zihan, for her relentless and selfless support in all these years.

Prof. Paulo J.M. Monteiro is the best guide I could possibly have for my academic journey. He shaped my knowledge background in material science and cement & concrete research, led me to the world of synchrotron-radiation-based experiments, provided me with every support I needed, and more importantly, demonstrated to me what a scientist and a professor should be like. I'd like to thank him for everything he did for me.

I've greatly benefited from Prof. Hans-Rudolf Wenk and Prof. Claudia P. Ostertag, in terms of building my knowledge in mineralogy and material mechanics. They've provided numerous insightful comments to this dissertation. Acknowledgment is also given to my collaborators who contribute to great extents of the experiments in this dissertation. They are Dr. Rupert J. Myers, Jiaqi Li, Dr. Mohammad Javad Abdolhosseini Qomi, Dr. Daniel Hernandez Cruz, Dr. Rae Taylor, Dr. Sungchul Bae, Timothy Teague, Dr. Eloisa Zepeda-Alarcon, Dr. Jinyuan Yan, Dr. Martin Kunz, Thomas J. Smart.

I sincerely appreciate the arguably world's BEST scientific community in UC Berkeley and Lawrence Berkeley National Lab, which paved my way of scientific research. I'd like to also thank the administration staff of CEE for their great support in the backstage – not always visible but extremely important.

Lastly I would like to thank my parents and parents-in-law. They always stand behind me, backing me up for every single decision I've made.

1. Introduction

1.1 Challenges of cement industry for the new century

Portland cement (PC) concrete, being used as the primary construction material, has cast the foundation for the modern infrastructure during the past 200 years. Its great success is largely attributed to the low cost and global availability of the raw materials used in PC manufacture (mainly limestone and clay) and concrete production (cement, water and aggregate, e.g. sand and stone), and to its robust, controllable and high performance.¹ According to the U.S. Geological Survey², the yearly production of PC has experienced an exponential increase in the past century, with a total manufacture of 4.6 billion metric tonnes in 2015. Assuming a typical mass percentage of ~15% cement in concrete composites, the yearly consumption of concrete is ~30 billion metric tonnes, which is the second most consumed commodity other than water (compared with ~1.5 billion metric tonnes crude steel in 2015³).

Large amount of concrete is needed in developing countries to construct the new infrastructure, and in developed countries to repair the damaged infrastructure.¹ However, there are still major technical problems relevant to the cement manufacturing, fresh concrete workability and long term performance.⁴⁻⁶

To address the environmental and civil engineering challenges, there are still unsolved scientific questions regarding the cement chemistry that are in urgent need of further investigation.^{7,8} For example, nowadays superplasticizer is often used to control the workability of fresh concrete mixture, which is efficient but also costly.¹ It works as surfactant that separate the previously agglomerated cement particles. C_3A (following the cement chemistry notation where $C=CaO$, $S=SiO_2$, $A=Al_2O_3$, $H=H_2O$, $\bar{S}=SO_3$) is the most reactive phase in PC clinkers, and its hydration greatly determines the workability of fresh concrete mix. Before superplasticizer become largely available, gypsum is often used to retard the rapid hydration of C_3A , yet the retardation mechanism is still unclear, despite 70 years of study.⁸⁻¹¹ This research barrier generally exists in the study of all clinker phases,¹⁰ and it is greatly due to the limit of experimental methods that allow probing the cement hydration process at a few nanometers scale in an *in-situ* manner, and at the same time preserve the sample from drying, high energy beam damage, CO_2 contamination, *etc.* Schemes that are able to fill such research gap may innovate engineering solutions to precisely control the early age hydration rate of cement, especially of C_3A , in order to control the workability in a more efficient and less costly way.

Apart from the early contribution from the C_3A hydration products, the major strength-contributing phase is calcium-silicate-hydrates (C-S-H) throughout the service life of PC concrete.¹² Despite its dominant importance to the performance of concrete, the physical properties of pore-free C-S-H lack adequate investigation through direct experimental

approaches. The difficulty mainly comes from the hierarchically porous structure of C-S-H down to single nanometer.¹³ Extensive chemical studies confirmed that C-S-H resembles the structure of natural tobermorite minerals at atomistic scale.¹⁴⁻¹⁷ Based on this model, atomistic simulations suggest its mechanical property is driven by crystallographic defects such as SiO₄ tetrahedra omission, yet this hypothesis lacks experimental validation on pore-free C-S-H solid.¹⁸ Such missing gap needs to be fill before realistic modelling of C-S-H takes a convincing next-step.

An efficient way to reduce the carbon footprint of concrete industry is to substitute PC with highly aluminosiliceous industrial by-products (also called supplementary cementitious materials (SCMs), e.g., fly ash and blast-furnace slag), which produce calcium aluminosiliceous hydrate (C-A-S-H) as the primary binding phase.^{6,19,20} Although numerous atomic simulations of C-A-S-H have been reported in the literature, similar difficulty exists in experimentally probing the intrinsic property of pore-free C-A-S-H, because of its poor crystallinity nature and hierarchically porous structure. The lack of experimental evidence greatly restricts the understanding and prediction of the performance of C-A-S-H, and development of the next generation C-A-S-H-based binding material.

The designed service life of modern infrastructures are often over 50 years. Many unexpected failure happens at material-level due to physical-chemical processes that deteriorate the microstructure of concrete matrix.¹ Investigating the microstructure evolution of cement paste over a long term is critical to understanding and predicting the durability-related processes, yet most existing studies focus on the first few months of cement hydration. As the major binding phase, more evidence of the late age (over 10 years) hydration product of C₃S is particularly needed to enrich the knowledge of concrete durability.

The above-mentioned topics are representative problems spanning from early age to very late age of concrete service life. Despite their importance, the conventional experimental methods have failed to provide insightful information, especially at nano and atomistic scale. Therefore, to address the environmental and civil engineering challenges in the new century, innovations in experimental methods are needed so that more experimental evidence of the hydration chemistry, and the structures and properties of the hydration product composites are provided. This dissertation attempts to apply the state of the art experimental packages supported by synchrotron radiation facilities, to the study of the above-mentioned topics. The synchrotron-radiation-based methods have significant advantage over conventional lab methods, in terms of the sample preparation protocols and the abundance of the collected information. For example, to image the hydrated cement particles at early age, SEM often requires severe pre-drying and coating with conductive materials, which may cause undefined damage to the samples. In contrast, the X-ray imaging tool in this dissertation uses drop-cast samples from the water-cement suspension. Besides, the synchrotron radiation facilities provide a suit of probes that measure the spatial-resolved crystallographic, chemical and multi-scale morphological information of

objects, which is critical to understand the microscale heterogeneity of cement hydration system. Details of the applied synchrotron-radiation-based methods are explained in the following sections.

1.2 Synchrotron-radiation-based experiment methods applied to cementitious materials

In the 1940s, it was discovered that the radial acceleration of charged particles generates electromagnetic waves.²¹ The unique characteristics of the synchrotron radiation (mostly in the form of X-ray), including extremely high brightness, tunable beam energy, coherence of incident beam, making it a powerful scientific research tool. A typical third generation synchrotron facility is composed of an accelerator, a storage ring and multiple beamlines that are designed to conduct specific experiments.²²⁻²⁴ The X-ray beam is introduced to the beamlines through magnetic field created by bending magnets, undulators and/or wigglers. After extensive development in the past half century, more than 50 synchrotron facilities (third generation) are now in operation world-wide, serving a broad categories of research fields such as life science, material science, chemical science, geoscience, physics, applied sciences, *et al.*²²

The Advanced Light Source (ALS) in Lawrence Berkeley National Laboratory (LBNL) was originally built in 1946 as a cyclotron for nuclear research. In 1993 it was transformed into a third generation synchrotron. It is operated at 1.9 GeV and 500 mA, producing photon flux up to $\sim 10^{10}$ times brighter than a typical lab X-ray source.²³ It has over 40 beamlines that use X-rays ranging from ~ 50 eV to 50 keV, providing research platforms for a broad range of scientific topics, including materials science, biology, chemistry, physics, and environmental sciences. In the past ten years, experiments in several beamlines of ALS have been conducted to probe the fundamental chemistry and material science-related problems of cement-based material.^{25,26} This dissertation mainly used two types of synchrotron-radiation-based techniques. The first technique is a nanometer-resolved microspectroscopy, i.e. a scanning transmission X-ray microscope (STXM) coupled with a ptychographic imaging tool; the second technique is high pressure X-ray diffraction (HP-XRD). A general introduction of these methods are given in the following sections.

STXM combines spatially resolved measurements with X-rays of tunable energy at synchrotron radiation facilities.²⁷ Figure 1.1 shows a typical STXM setup: the sample is scanned with an incident X-ray beam, focused using a zone plate and filtered with an order sorting aperture, and the transmitted beam is collected as raw data. The bonding and coordination environment of elements in certain phases that are intermixed at the nano- and microscales can be spatially determined by STXM using coupled near edge X-ray absorption fine structure (NEXAFS) measurements.²⁸ The NEXAFS spectra of a certain element contains abundant features that are often sensitive to its crystallographic and chemical status, for example the number of coordination neighbor atoms and their configurational symmetry. This technique has gained significant interest in geology²⁹,

environmental and material research applications³⁰, photovoltaics³¹ and cosmological chemistry³².

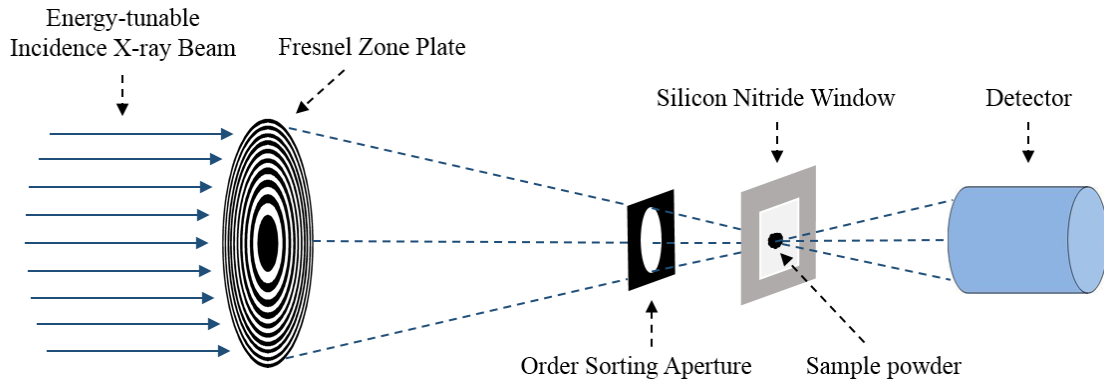


Figure 1.1 Schematic diagram of STXM

There are three major advantages of using STXM to study cementitious system. 1). Cementitious systems have submicron chemical and structural heterogeneities, which may drastically evolve along with cement hydration, STXM provides a powerful analytical tool for measuring both spectroscopic and spatial information down to the micro- or nano-meter scales for cementitious materials. 2). Cementitious system contains both crystalline phases and amorphous phase. STXM probes the local atomistic configuration regardless of the materials' crystallinity, whereas lab XRD only measures crystalline phases. 3). The incident beam energy used in STXM is usually below 2-3 keV, which causes much less beam damage, compared with scanning electron microscope (SEM) and transmission electron microscope (TEM) measurements.

The STXM studies are conducted at ALS Beamline 5.3.2.1 and 5.3.2.2., which utilize X-rays of tunable energy from 250 to 780 eV (5.3.2.2), and from 600 to 2000 eV (5.3.2.1), respectively.²⁷ The bonding and coordination environments of a wide range of elements, (including the major elements in concrete, e.g. O, Ca, Si, Al, Mg, C) can be spatially determined by STXM. Coupled with newly commissioned ptychographic imaging modulus, beamline 5.3.2.1 is now able to provide spectroscopic analysis combined with high resolution ptychographic imaging down to ~5 nm.³³

Soft X-ray Ptychographic imaging is a recently developed technique that operates with a typical STXM setup.³³ It uses recorded coherent diffraction patterns to reconstruct the transmission image of the object. As implied by the name (ptycho, from the Greek, meaning "to fold"), the raw diffraction pattern is collected in partially overlapped step size, which is then processed with an iterative algorithm that leads to a unique solution of the complex refractive index of each pixel.

A coherent X-ray beam can be expressed as a complex number Z , where the intensity of the beam is its square $|Z|^2$. When X-ray beam passes matter, its intensity and phase are both altered. A detector only records the intensity of the diffracted beam, yet its phase

information is lost. Ptychographic imaging methods are proposed to solve this “phase problem”. As illustrated in Figure 1.2(a), when the incident beam passes two overlapped scanning areas of the object, the amplitudes of individual diffraction beam ($|Z1|$ and $|Z2|$), and the overlapped region ($|Z1+Z2|$) are recorded. In the complex coordination system (Figure 1.2(b)), $Z1$, $Z2$ and $Z1+Z2$ must form a closed triangle. With their amplitude been measured, the angle φ between $Z1$ and $Z2$, i.e. the relative phase of $Z2$ to $Z1$ is solved. Note that the sign of the angle φ could not be determined. When the number of linearly positioned overlapped diffraction beam increases to N (Figure 1.2(c)), there is generally 2^N undistinguished combinations. This ambiguity can be reduced by increasing the ratio of measurements to unknowns, as shown in Figure 1.2(d).

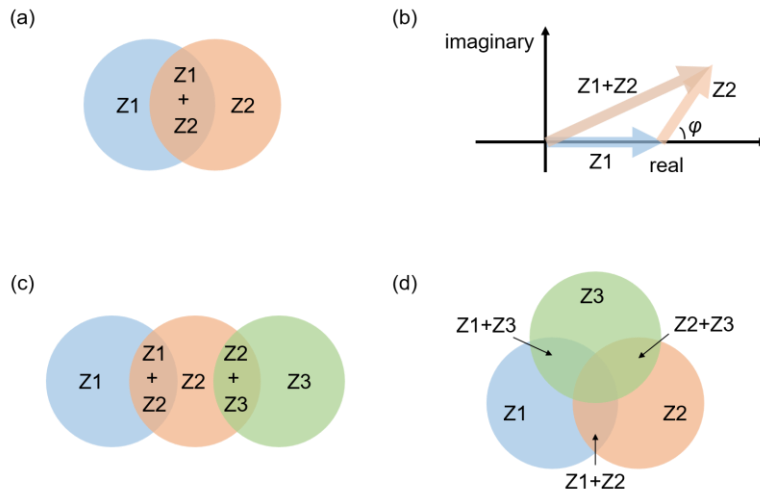


Figure 1.2 Schemes of the phase relationship in STXM ptychography. (a) Two diffracted disks lying in the Fraunhofer diffraction plane. (b) Phase relationship of the underlying amplitudes of these two disks. (c) Three linearly positioned interfering disks. (d) Ambiguity in this phase problem is reduced because the ratio of measurements to unknowns increases. The figures are adopted from literature³⁴.

The original idea of Ptychography exists for almost half century³⁵⁻³⁷. Yet it is only recently that X-ray ptychography has gained rapid development in synchrotron facilities, due to the development of high performance scanning system and super computers. This method removes the resolution limit set by the characteristics of the X-ray optics. It yields high quality images at signal-nanometer resolution, which largely enhances the imaging ability of STXM. It has great potential to be applied in nano-scale research, and is considered one of the most important new directions of X-ray microscopy³⁸.

HP-XRD was developed principally to study the geochemistry and geophysics of earth minerals subjected to extremely high pressure and temperature.³⁹ It has also drawn great attention in studying the pressure and temperature-induced behavior of lab-synthesized (nano)crystalline materials.^{40,41} For HP-XRD experiment, a ‘diamond anvil cell’ (DAC) is always used to create elevated pressure values. A typical setup of HP-XRD DAC is shown

in Figure 1.3(c), where the investigated sample is placed in a sub-millimeter sized cylindrical chamber, which is closed from both sides with diamond anvil. The sample chamber containing the sample can be filled with a pressure medium that generates hydrostatic pressure up to several hundred GPa when external loading is applied to the DAC. Ruby (Cr^{3+} doped Al_2O_3) powder is often used as pressure calibrant by correlating its fluorescence signal and hydrostatic pressure.⁴² Figure 1.3 (a) is a typical Merrill-Bassett type DAC, and (b) is an image of a gasket being closed with diamond anvils.

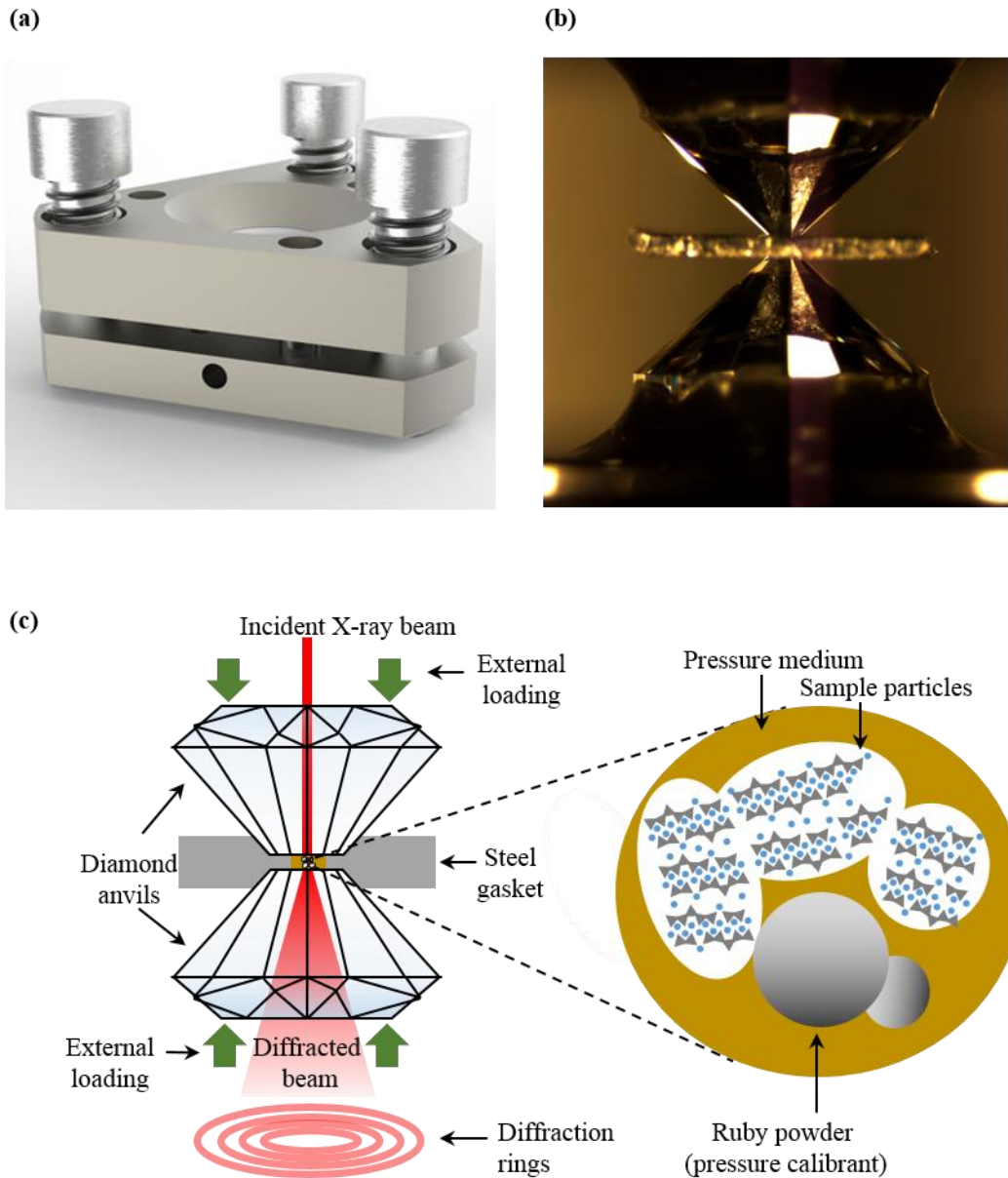


Figure 1.3 (a) A typical Merrill-Bassett type diamond anvil cell (DAC), (b) gasket being closed with diamond anvil pairs, and (c) a sketch of a DAC loaded with samples.

The Beamline 12.2.2 in ALS is home to a HP-XRD platform.^{40,41} Its incident beam energy is tunable within range of 5-35 keV using a pair of flat crystals monochromator with Si(111) crystals ($E/\Delta E \sim 7000$) and W/B₄C multilayers ($E/\Delta E \sim 100$), which allows collecting the diffraction data of powder or single crystal samples within a designated q -range. Three types of detector are available, namely a MAR345 image plate (for high resolution), a Perkin Elmer CMOS (for fast image collection) and an Amp-Tek fluorescence detector (to collect fluorescence signal), which allows the investigating samples of a wide range of crystallinity characteristics. In this dissertation, an incident beam energy of 25 keV and the MAR345 detector are used to provide proper q -range and better resolution for the diffraction of C-(A-)S-H.

Other synchrotron sources

Synchrotron resources other than ALS were also utilized, including the Hard X-ray Nanoprobe beamline (BL26-ID-C) at the Advanced Photon Source (APS) of USA, and the Small/Wide Angle X-ray Scattering beamline (BL1.3W) at the Synchrotron Light Research Institute (SLRI) of Thailand. The Hard X-ray Nanoprobe Beamline provides a combined package of full-field imaging using transmission, fluorescence and nanodiffraction signals, in a spatial resolution of ~ 30 nm. The energy scanning range is 3-30 keV X-rays, which covers the absorption edge of a broad range of elements.⁴³ The Small/Wide Angle X-ray Scattering (SAXS/WAXS) beamline in SLRI covers energy range within 6-9 keV, equipped with a CCD detector for SAXS and an image plate for WAXS. The beamline is optimized for capable of conducting in-situ experiments, which greatly benefits the investigation of cement hydration in this thesis.⁴⁴

1.3 Contents of this thesis

The main scientific body of this thesis is composed of experiments and analysis of topics that are critical to the performance of cementitious material at different ages of its service life. For instance, the study on C₃A hydration is closely related to the early age workability; the study on C-(A-)S-H aims to understand the property of concrete matrix in the mature age, as a function of the chemical composition; the study on a 50-year-old C₃S paste aims to track the multi-scale structural change of the cementitious matrix over the long term. In all these studies, a suit of synchrotron-radiation-based methods are applied, and they share similar philosophy of designing novel experimental experiments to the study of modern construction material, which should add new insights into, as well as inspire future work on the fundamental knowledge of cement and concrete science.

In chapter 1, the general background the study is described. The principles of the synchrotron-radiation-based methods used in this dissertation are also introduced, along with a discussion of their advantage over the conventional lab methods.

Chapter 2 summarizes a literature survey of existing results and the missing information of the specific topics that are addressed in this dissertation.

In chapter 3, methodology details are described, including sample preparation, data acquisition and analytical methods.

Chapter 4 presents the investigation of the early-age hydration mechanism of cubic C₃A in the presence of gypsum. SAXS and STXM are integrated to provide the crystal-chemical information on the dissolution-precipitation frontier of partially hydrated C₃A in the induction period. Ptychographic images and nano-CT are used to quantify the nanoscale 2D and 3D morphology of the hydration product.

Chapter 5 describes the experimental research of HP-XRD integrated with atomistic simulations, aimed to correlate the anisotropic elasticity of nano-crystalline C-S-H to the systematically varying atomistic configuration caused by changing Ca/Si. The deformation of the lattice parameters are tracked as functions of applied and simulated hydrostatic pressure. The atomistic scale mechanism of C-S-H deformation is analyzed by simulation. Improvements to constructing more realistic C-S-H models are discussed.

Chapter 6 summarizes the HP-XRD results that are used to quantify the influence of dreierketten chain cross-linking on the anisotropic mechanical behavior of C-(A-)S-H. Similar as in chapter 4, the deformations along each lattice directions of C-(A-)S-H are investigated as functions of hydrostatic pressure, which yields the anisotropic incompressibility and the overall bulk modulus. The role of Al-induced crosslinking in modifying the overall modulus is discussed.

Chapter 7 reports the investigation of a 50-year-old hydrated alite (96% C₃S) paste, at the nano- and micro-scale, aiming at understanding the microstructure of C₃S hydrates at the extremely late age of concrete service life. SEM and TEM are used to obtain the nanoscale morphology; STXM, coupled with XRD and NMR, is used to study the crystal-chemical information of C-S-H.

Chapter 8 highlights the major conclusions and impact of the research. Possible directions of future studies are summarized.

Chapter 9 presents an appendix of raw material characterization and data analysis schemes (summarized in the appendix for conciseness of the main chapter contents).

1.4 References

1. Mehta, P.K. & Monteiro, P.J. *Concrete Microstructure, Properties, and Materials* (McGraw-Hill Companies, New York City, 4th edition, 2014).
2. “Cement Statistics and Information.” *US Geological Survey*. US Department of the Interior. URL: <http://minerals.usgs.gov/minerals/pubs/commodity/cement/>.
3. “Steel Statistic Yearbook.” *World Steel Association*. URL: <https://www.worldsteel.org/statistics/statistics-archive/yearbook-archive.html>.

4. Bentur, A. Cementitious materials-nine millennia and a new century: past, present, and future. *J. Mater. Civ. Eng.* **14**, 2-22 (2002).
5. Flatt, R.J., Roussel, N. & Cheeseman, C.R., 2012. Concrete: An eco material that needs to be improved. *J. Eur. Ceram. Soc.* **32**, 2787-2798 (2012).
6. Mehta, P.K. Reducing the environmental impact of concrete. *Con. Inter.* **23**, 61-66 (2010).
7. Ludwig, H.M. & Zhang, W. Research review of cement clinker chemistry. *Cem. Con. Res.* **78**, 24-37 (2015).
8. Scrivener, K.L., Juilland, P. & Monteiro, P.J. Advances in understanding hydration of Portland cement. *Cem. Con. Res.* **78**, 38-56 (2015).
9. Collepardi, M., Baldini, G., Pauri, M. & Corradi, M. Tricalcium aluminate hydration in the presence of lime, gypsum or sodium sulfate. *Cem. Concr. Res.* **8**, 571-580 (1978).
10. Bullard, J. W., *et al.* Mechanisms of cement hydration. *Cem. Concr. Res.* **41**, 1208-1223 (2011).
11. Black, L., *et al.* Hydration of tricalcium aluminate (C₃A) in the presence and absence of gypsum — studied by Raman spectroscopy and X-ray diffraction. *J. Mater. Chem.* **16**, 1263-1272 (2006).
12. Taylor, H. F. W. *Cement chemistry, second ed.*. Thomas Telford, London (1997).
13. Allen, A. J., Thomas, J. J. & Jennings, H. M. Composition and density of nanoscale calcium–silicate–hydrate in cement. *Nat. Mater.* **6**, 311-316 (2007).
14. Myers, R. J., L'Hôpital, E., Provis, J. L. & Lothenbach, B. Effect of temperature and aluminium on calcium (alumino) silicate hydrate chemistry under equilibrium conditions. *Cem. Concr. Res.* **68**, 83-93 (2015).
15. Walker, C. S., Savage, D., Tyrer, M. & Ragnarsdottir, K. V. Non-ideal solid solution aqueous solution modeling of synthetic calcium silicate hydrate. *Cem. Concr. Res.* **37**, 502-511 (2007).
16. Lothenbach, B. & Nonat, A. Calcium silicate hydrates: Solid and liquid phase composition. *Cem. Concr. Res.* **78**, 57-70 (2015).
17. Nonat, A. The structure and stoichiometry of CSH. *Cem. Concr. Res.* **34**, 1521-1528 (2004).
18. Qomi, M. A., *et al.* Combinatorial molecular optimization of cement hydrates. *Nat. Commun.* **5**, (2014).
19. Palomo, A., Grutzeck, M.W. & Blanco, M.T. Alkali-activated fly ashes: a cement for the future. *Cem. Concr. Res.* **29**, 1323-1329 (1999).
20. Juenger, M.C.G., Winnefeld, F., Provis, J.L. & Ideker, J.H. Advances in alternative cementitious binders. *Cem. Concr. Res.* **41**, 1232-1243 (2011).

21. Elder, F.R., Gurewitsch, A.M., Langmuir, R.V. & Pollock, H.C. Radiation from electrons in a synchrotron. *Phy. Rev.* **71**, 829 (1947).
22. Bilderback, D.H., Elleaume, P. & Weckert, E. Review of third and next generation synchrotron light sources. *J. Phy. B*, **38**, S773 (2005).
23. “Quick facts”. *Advanced light source*. Office of science, US Department of Energy. URL: <https://www-als.lbl.gov/index.php/about-the-als/quick-facts.html>.
24. Austin, E. Advanced Photon Source. *Syn. Rad. News*, **29**, 29-30 (2016).
25. Monteiro, P.J.M., Kirchheim, A.P., Chae, S., Fischer, P., MacDowell, A.A., Schaible, E. & Wenk, H.R. Characterizing the nano and micro structure of concrete to improve its durability. *Cem. Con. Com.* **31**, 577-584 (2009).
26. Chae, S.R., Moon, J., Yoon, S., Bae, S., Levitz, P., Winarski, R. & Monteiro, P.J. Advanced nanoscale characterization of cement based materials using X-ray synchrotron radiation: a review. *Int. J. Concr. Struct. Mat.* **7**, 95-110 (2013).
27. Kilcoyne, A.L.D., Tyliczszak, T., Steele, W.F., Fakra, S., Hitchcock, P., Franck, K., Anderson, E., Harteneck, B., Rightor, E.G., Mitchell, G.E. & Hitchcock, A.P. Interferometer-controlled scanning transmission X-ray microscopes at the Advanced Light Source. *J. Syn. Rad.* **10**, 125-136 (2003).
28. Stöhr, J. *NEXAFS spectroscopy* (Vol. 25) (Springer Science & Business Media, 2013).
29. Wan, J., Tyliczszak, T. & Tokunaga, T.K. Organic carbon distribution, speciation, and elemental correlations within soil microaggregates: applications of STXM and NEXAFS spectroscopy. *Geochim. Cosmochim. Acta.* **71**, 5439-5449 (2007).
30. Chen, C., Dynes, J.J., Wang, J., Karunakaran, C. & Sparks, D.L. Soft X-ray spectromicroscopy study of mineral-organic matter associations in pasture soil clay fractions. *Env. Sci. & Tech.* **48**, 6678-6686 (2014).
31. McNeill, C.R. *et al.* Evolution of the nanomorphology of photovoltaic polyfluorene blends: sub-100 nm resolution with x-ray spectromicroscopy. *Nanotechnology*, **19**, 424015 (2008).
32. Sandford, S.A. *et al.* Organics captured from comet 81P/Wild 2 by the Stardust spacecraft. *Science*, **314**, 1720-1724 (2006).
33. Shapiro, D.A. *et al.* Chemical composition mapping with nanometre resolution by soft X-ray microscopy. *Nat. Photon.* **8**, 765-769 (2014).
34. Rodenburg, J.M. Ptychography and related diffractive imaging methods. *Adv. Imaging Elec. Phys.* **150**, 87-184 (2008).
35. Hoppe, W. Diffraction in inhomogeneous primary wave fields. 1.Principle of phase determination from electron diffraction interference. *Acta Crystallogr. A* **25**, 495–501. (1969).

36. Hoppe, W. Diffraction in inhomogeneous primary wave fields. 3. Amplitude and phase determination for nonperiodic objects. *Acta Crystallogr. A* **25**, 508–515 (1969).
37. Hoppe, W. Trace structure analysis, ptychography, phase tomography. *Ultramicroscopy* **10**, 187–198 (1982).
38. Falcone, R. *et al.* New directions in X-ray microscopy. *Contemp. Phys.* **52**, 293-318 (2011).
39. Rissanen, K. ed. *Advanced X-ray crystallography* (Vol. 315). (Springer Science & Business Media, 2012).
40. Prewitt, C.T. and Downs, R.T., ‘High-pressure crystal chemistry’, *Rev. Mineral.* **37** (1998) 284-318.
41. Kunz, M., *et al.*, ‘A beamline for high-pressure studies at the Advanced Light Source with a superconducting bending magnet as the source’, *J. Syn. Rad.* **12** (2005) 650-658.
42. Mao, H.K., Xu, J.A. & Bell, P.M. Calibration of the ruby pressure gauge to 800 kbar under quasi-hydrostatic conditions. *J. Geophys. Res. Solid Earth.* **91**, 4673-4676 (1986).
43. Winarski, R.P., *et al.* A hard X-ray nanoprobe beamline for nanoscale microscopy. *J Syn. Rad.* **19**, 1056-1060 (2012).
44. Phinjaroenphan, R., *et al.* SAXS/WAXS Capability and Absolute Intensity Measurement Study at the SAXS Beamline of the Siam Photon Laboratory. *J. Phy. Conference Series*, **425**, 132019 (2013).

2. Existing results and open questions – a short literature survey

Chapter 1 presented a brief description of the topics being investigated in this dissertation. This Chapter summarizes the relevant literature starting from the early hydration to the late concrete service life.

2.1 Early age – C₃A hydration in the presence of gypsum

Good workability of fresh PC concrete is fundamentally important to produce highly durable infrastructure, which is essential to reduce the environment impact of concrete.¹⁻⁴ Portland cement (PC) clinker is mainly composed of four mineral phases, i.e. tricalcium aluminate (C₃A), tricalcium silicate (C₃S), dicalcium silicate (C₂S), and tetracalcium aluminoferrite (C₄AF).¹ Gypsum (CaSO₄·2H₂O), and sometimes bassanite (CaSO₄·0.5H₂O) are intermixed with the clinker during the grinding process, in order to control the fluidity and the overall time window of workability of fresh PC concrete mixtures to avoid ‘flash setting’,^{1,4-6} by retarding the hydration of the most reactive PC clinker phase – tricalcium aluminate (C₃A). This retarding phenomena guarantees that fresh concrete is workable for a few hours before solidifying, even though nowadays chemical admixture also plays critical role in engineering the workability.

The retardation of C₃A hydration in the presence of gypsum can be delayed by minutes to hours depending on the C₃A/gypsum ratio in the cement composition.^{1,2,5} This interval of low reactivity, also called the ‘induction period’, enables fresh concrete mixture to be workable; however, the chemistry underlying this mechanism has not been elucidated despite being researched for over half a century.^{5,7-18} This uncertainty has mostly persisted because direct evidence of this mechanism has not been reported. Two main hypotheses exist, which describe C₃A hydration inhibition to occur via: (i) the formation of ettringite⁷ (6CaO·Al₂O₃·SO₃·32H₂O)- and/or Ca-Al layered double hydroxide (AFm, ‘aluminoferrite-mono’)-type barrier to ion transport, which may include monosulfate⁸ (4CaO·Al₂O₃·SO₃·18H₂O, also denoted as \bar{S} -AFm) or hydroxyl AFm⁹ (OH-AFm, mainly 4CaO·Al₂O₃·19H₂O (C₄AH₁₉)¹⁰, which dehydrates to 4CaO·Al₂O₃·13H₂O (C₄AH₁₃) when relative humidity drops to ~88%^{11,12}, and gradually converts to 3CaO·Al₂O₃·6H₂O (C₃AH₆)⁹); or (ii) the adsorption of Ca and/or S complexes on dissolving C₃A particles.^{13,14} The latter hypothesis has recently gained increasing support although the diffusion-barrier hypothesis has not yet been disproven, due mainly to ettringite precipitates hindering observations of the C₃A dissolution frontier during hydration.^{15,16} Therefore, a nanometer-resolved chemical-crystallographic probe is needed to more fully investigate the dissolution frontier. Conventional imaging methods, including scanning electron microscopy (SEM),¹⁷ transmission electron microscopy (TEM)¹⁸ are restricted by destructive sample preparation and electron beam damage. Three-dimensional (3D) studies have never been reported for this system at sub-micron scale yet may deliver critical information that cannot be probed by 2D imaging.¹⁹

Recent advancements in synchrotron-based experimental technology have substantially improved the ability to obtain direct chemical and morphological information in hydrated C₃A systems: state-of-the-art soft X-ray ptychography imaging^{20,21} and coupled scanning transmission X-ray microscopy (STXM) with X-ray adsorption near-edge fine structure (XANES)²² now enable transmission imaging at ~5 nm pixel resolution and chemical mapping at ~70 nm pixel resolution, respectively. A nano-CT beamline could yield 3D images at resolution of 10-20 nm.²³ From the collected 2D and 3D images, small angle scattering (SAS) can be calculated to quantify the morphological information of areas-of-interests^{24,25}. These methods are promising to yield novel evidence of retardation mechanism of C₃A hydration in the presence of sulfate.

2.2 Mature age – the chemistry-structure-property correlation of C-S-H

A century of exhaustive research highlights that optimizing properties of PC concrete's principal binding phase, calcium silicate hydrate (C-S-H), is a potential venue to achieve better concrete. C-S-H is poorly crystalline and hierarchically porous at multiscale.²⁶⁻²⁸ It exists as a solid solution with variable structure and chemical composition.^{29,30} Such characteristics make it exceedingly difficult to probe composition-structure-property correlation in pore-free C-S-H systems.²⁹⁻³² Theoretical prediction of macro-scale mechanical property of PC concrete requires the input of the property of pore-free solid and the multi-scale pore structure. Therefore the missing information of C-S-H mechanical behavior at fundamental scale (several nanometer) is critical to advance to the multi-scale modeling of concrete.

The nanocrystalline C-S-H is structurally analogous to tobermorite, a natural mineral family structurally composed of layered SiO₄ 'dreierketten'-based chains on either side of CaO₇ double sheets, which are themselves separated by aqueous-containing 'interlayer' space³³ (Figure 2.1(a)). The thicknesses of the interlayer space is directly related to the basal spacing, which are commonly 9.3 Å, 11.3 Å, 14.0 Å in tobermorite¹⁹⁻³⁸. The principal mechanisms of increasing the calcium-to-silicon molar ratio (Ca/Si) in tobermorite (generally <0.84) to the more realistic case of C-S-H are through the omission of SiO₄ tetrahedra in bridging sites of the dreierketten Si chain, and enrichment of Ca in the interlayer space.³⁹ The basal spacing of C-S-H (I) generally decreases with increasing Ca/Si due to the ionic force of cations in the interlayer.⁴⁰⁻⁴¹

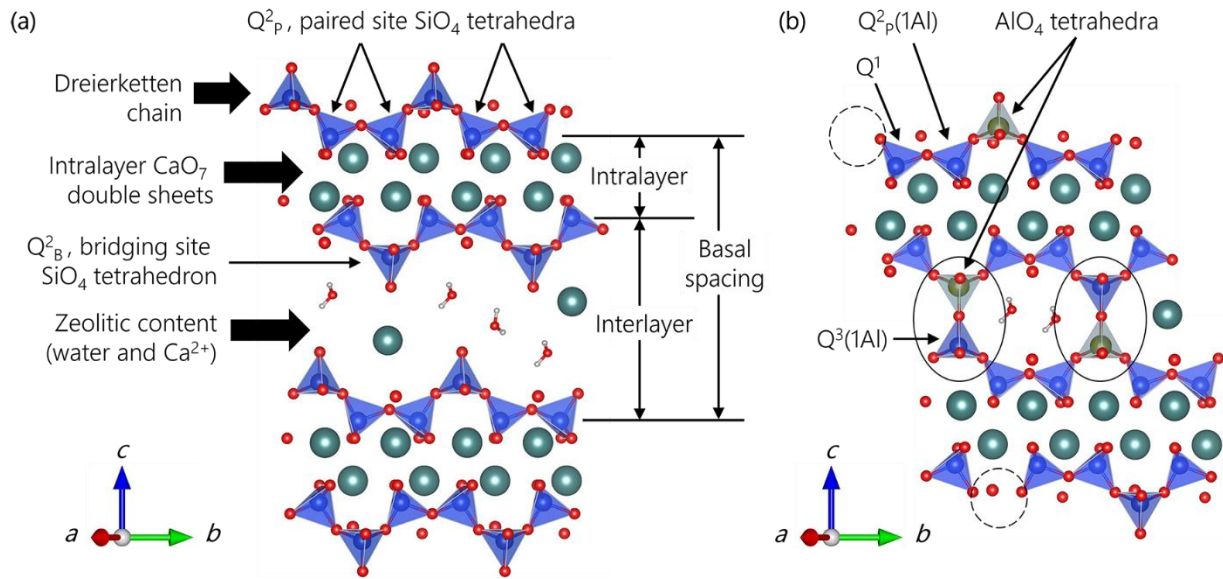


Figure 2.1. Schematics of (a) crystalline C-S-H (modified from 14 Å tobermorite³⁸) and (b) C-A-S-H atomistic structures with Al-induced cross-linking (solid circles). Spheres of blue, red, green, white and yellow colors represent Si, O, Ca, H and Al, respectively. The dashed circles are tetrahedral Si vacancies in bridging sites (b). The conventional $Q^n(mAl)$ -notation is used, which describes aluminosilicate chain polymerization, e.g., Si tetrahedra are connected to n adjacent tetrahedra (SiO_4 or AlO_4), of which m are AlO_4 ; subscripts P and B represent paired and bridging sites, respectively.

Predicting the multi-scale mechanical properties of C-S-H by up-scaling homogenization algorithm eventually requires the mechanical properties at the lowest level.^{43,44} With applying micro-poromechanics analysis to the experimental results from nanoindentation, it is possible to obtain an indirect measurement of fundamental elastic and strength properties of C-S-H as influenced by the Ca/Si ratio.⁴³⁻⁴⁸ Although successful at yielding a statistical link between the phase chemistry and mechanical properties, this method remains strictly limited to the characteristic length of the interaction volume in order of a micrometer. The direct experimental link between the chemical composition, molecular structure, and mechanical properties of C-S-H still remains vastly unexplored.

Atomistic simulations provide a wealth of computational techniques to explore composition-structure-property correlation in C-S-H systems. With the advent of realistic C-S-H modeling, researchers are proposing molecular models of C-S-H that are in partial agreement with the scattered experimental data in the literature.^{48,49} To comply with ²⁹Si NMR measurements at varying Ca/Si, the solid backbone of C-S-H is created by the removal of silica groups from silicate chains in tobermorite minerals. The defective structure subsequently adsorbs nano-confined water by putting it in contact with a reservoir using Grand Canonical Monte Carlo technique.⁴⁸ Finally, the simulation cell is relaxed using reactive molecular dynamics⁵⁰ or first principle calculations, while the C-S-H density

is allowed to vary according to thermodynamic conditions. These modeling efforts indicate that both the structural order and mechanical properties of C-S-H decrease with increasing Ca/Si.^{48,51,52} However, this hypothesis can be questionable as 14 Å tobermorite, although highly crystalline, exhibits significantly lower modulus than poorly crystalline but denser phase, as confirmed by both simulation and experiment.⁵²⁻⁵⁴ The fact that defect-driven models cannot explain such behavior leads to an alternative hypothesis that the mechanical property of C-S-H at the nanoscale is preferentially density-driven. Experimental evidence is urgently needed to validate this hypothesis.

2.3 Mature age – influence of Al-incorporation on the nanomechanical property C-A-S-H

The atomistic structure of calcium aluminosilicate hydrate (C-A-S-H) and its similarity with the naturally occurring tobermorite mineral family have attracted significant interest in the scientific community. As a high-performance binding material in concrete, it is produced from the reaction between calcic and aluminosiliceous components in water and often under-elevated temperature. This phenomena is found in the ancient Roman concrete⁵⁵, alkali activated cements^{56,57} and massive-volume castings of concrete—such as in the case of dams—comprised of hydrated Portland cement (PC) blended with supplementary cementitious materials (SCMs, fly ash, blast-furnace slag, volcanic ash, etc.)⁵⁸. Compared to Al-free calcium silicate hydrate (C-S-H), which is the most abundant and key binding phase in PC concrete), the process to produce C-A-S-H in contemporary cementitious materials usually involves incorporating more SCMs; this results in a lower CO₂ footprint, which is critical in improving the sustainability of the construction industry.⁵⁹

C-A-S-H synthesized hydrothermally at room temperature lacks long-range crystallinity but has an atomistic structure analogous to tobermorite as shown in Figure 2.1(a), with the thickness of the intralayer roughly constant while that of the interlayer varying greatly with the synthesizing conditions. Besides the bridging site vacancies as in C-S-H, C-A-S-H is contains defects such as Al for Si substitution in bridging sites⁶⁰⁻⁶³. Cross-linking of adjacent dreierketten chains can also occur, as shown in Figure 2.1(b). The long-range order of C-A-S-H is reported to increase with Al-incorporation and curing at elevated temperature²⁷. Al-induced cross-linking is observed at 80 °C²⁷ but also at lower temperatures when synthesized using aqueous alkali hydroxide solutions^{27,64,65}; however, Al-incorporation typically decreases C-A-S-H crystallinity at room temperature^{40,65}.

Despite numerous studies on the chemistry and crystallography of C-A-S-H, the correlation between its structure and mechanical properties at atomistic scale has rarely been experimentally studied: the influence of Al-induced cross-linking on the mechanical properties of C-(A-)S-H has never been reported. Similar as C-S-H, direct experimental data on pore-free C-(A-)S-H solids are difficult to obtain because it has hierarchical porosity down to the atomistic scale. A recent HP-XRD study reported the bulk modulus of macro-crystalline Al-tobermorite to be 55 ± 5 GPa⁶⁶. It was also previously reported that

Al-incorporation does not change the mechanical properties of nano-crystalline C-A-S-H in alkali-activated slag (AAS) cement (38 ± 3 GPa) relative to C-S-H(I) (38 ± 7 GPa)⁵⁴; however, the obvious differences in the sample preparation conditions employed for each material and the lack of chemical crystallographic characterization shed doubt on the reliability of this conclusion. Therefore, the influence of Al incorporation on the atomistic scale mechanical properties of C-A-S-H remains unclear. This information is critical for understanding, predicting and designing the mechanical performance of concrete structures comprised of C-(A-)S-H-based composites, i.e., the great majority of contemporary construction materials.

Atomistic simulations of C-A-S-H have been reported,⁶⁷⁻⁶⁹ however there exist clear missing gaps that restrict its improvement: (a) a lack of direct experimental tests to validate the simulated mechanical properties at the atomistic scale; (b) to date, focus has been directed on the structural change but limited work performed on its influence to the mechanical properties remains^{60,68,69}; and (c) little experiment-supported understanding of the critical structural features (among the overall Ca to Si molar ratio (Ca/Si), vacancies and Al-uptake in the dreierketten chain, basal spacing, interlayer contents, etc.) that have the most significant influence on the mechanical property. These missing information need to be provided to pave the way for better modelling of C-A-S-H.

2.4 Late age - microstructural study of a 50-year-old hydrated C₃S paste

Among all clinker phases of OPC, alite, or its pure chemical phase tricalcium silicate ($3\text{CaO}\cdot\text{SiO}_2$, or, in cement chemistry notation, C₃S), is of the highest content and second highest reactivity (after C₃A). The hydration of C₃S greatly contributes to the early strength, and dominates the strength after 2-3 days casting of OPC concrete. It is therefore frequently used to model the hydration system of OPC.^{8,70} However, even when modeling a simple system such as pure C₃S, the dissolution, diffusion and precipitation processes involved in the hydration process still remains unclear.

For example, the heat generated by C₃S hydration shows an induction behavior between the initial heat release (shortly after mixing with water)^{71,72} and accelerated reaction period, which cannot be thoroughly explained by any single hypothesis. Stein⁷³ was the first researcher to attribute this induction behavior to the rapid formation of a meta-stable calcium silicate hydrate layer, which is thin but still able to prohibit the dissolving of unreacted C₃S. Thomas has suggested that the slow rate of nucleation on C₃S surface could solely account for the phenomena.⁷⁰ This hypothesis gives a more robust interpretation of the heat evolution compared to the Avrami model, which is based on random nucleation⁷⁴.

The C-S-H gel, produced from the hydration of C₃S, is the major binder of PC concrete. Unlike the previous discussed C-S-H(I), C-S-H gel produced by C₃S is less crystalline and its atomistic configuration can hardly be detected by X-ray diffraction-based methods. It's still unclear whether C-S-H gel resembles tobermorite at the atomistic scale, or its structure is a hybrid of tobermorite molecular pieces with a more Ca-rich phase, e.g. Ca(OH)₂ and

jennite ($\text{Ca}_9\text{Si}_6\text{O}_{18}(\text{OH})_6 \cdot 8\text{H}_2\text{O}$).³³ The main consideration of the latter hypothesis is that C-S-H gel formed in the hydration of pure C_3S has an average Ca/Si \approx 1.7, which is much larger than that of tobermorite (0.67-0.8) and most lab synthesized C-S-H(I) (0.6-1.5).

At nanoscale, Jennings⁴² suggested that the basic construction unit of C-S-H is non-spherical globule whose dimension is around 5 nm. Constantinides and Ulm⁷⁵ applied this model successfully to their nano-indentation experiments. The TEM studies of hydrated C_3S and pozzolanic material by Richardson³³ and Taylor⁷⁶ demonstrated the material exhibiting a fibrillar structure of C-S-H outer product in a hydrated C_3S paste, while the inner product is featureless and resembles the globular morphology as pictured by Jennings⁴² (here outer product (OP) and inner product (IP) stand for the hydrates outside and within the original C_3S -water interface). Each OP C-S-H fiber (100-150 nm wide) is composed of a finer substructure also in a fibrillar shape. This substructure is about 3 nm in its smallest dimension, with the length varying from a few nanometers to many tens of nanometers.

The existing investigations concentrate on the first few months after C_3S hydration, yet there is a lack in the characterization of the microstructure and chemistry of late age C_3S paste. It is unclear whether the C-S-H gel crystallized to more ordered phase during the extremely long service life of PC infrastructure. There is also only scattered evidence whether the silicate chain linkage of C-S-H gel significantly increases during long term curing. More evidence is required to further understand the long-term microstructure evolution of PC concrete.

2.5 References

- 1 Mehta, P. K. & Monteiro, P. J. *Concrete Microstructure, Properties, and Materials* (McGraw-Hill Companies, New York City, 4th edition, 2014).
- 2 Barnes, P. & Bensted, J. *Structure and Performance of Cements* (CRC Press, Boca Raton, 2002).
- 3 Peters, G. P., *et al.* Rapid growth in CO₂ emissions after the 2008-2009 global financial crisis. *Nature Clim. Change* **2**, 2-4 (2012).
- 4 Mehta, P. K. Reducing the Environmental Impact of Concrete. *Concr. Int.* **23**, 61-66 (2001).
- 5 Taylor, H. F. *Cement Chemistry*. (Thomas Telford, London, 2nd edition, 1997).
- 6 Nelson, E. B. *Well Cementing*. (Elsevier Science Publisher B. V., Amsterdam, 1990).
- 7 Collepardi, M., Baldini, G., Pauri, M. & Corradi, M. Tricalcium aluminate hydration in the presence of lime, gypsum or sodium sulfate. *Cem. Concr. Res.* **8**, 571-580 (1978).
- 8 Bullard, J. W., *et al.* Mechanisms of cement hydration. *Cem. Concr. Res.* **41**, 1208-1223 (2011).

- 9 Black, L., *et al.* Hydration of tricalcium aluminate (C₃A) in the presence and absence of gypsum — studied by Raman spectroscopy and X-ray diffraction. *J. Mater. Chem.* **16**, 1263-1272 (2006).
- 10 Christensen, A. N., Jensen, T. R., Scarlett, N. V., Madsen, I. C. & Hanson, J. C. Hydrolysis of Pure and Sodium Substituted Calcium Aluminates and Cement Clinker Components Investigated by in Situ Synchrotron X-ray Powder Diffraction. *J. Am. Ceram. Soc.* **87**, 1488-1493 (2004).
- 11 Aruja, E. The unit cell and space group of 4CaO Al₂O₃ ·19H₂O polymorphs. *Acta Cryst.* **14**, 1213-1216 (1961).
- 12 Roberts, M. H. New calcium hydrates. *J. Appl. Chem.* **7**, 543-546 (1957).
- 13 Tadros, M.E., Jackson, W.Y. & Skalny, J. Study of the dissolution and electrokinetic behavior of tricalcium aluminate. *Colloid Interface Sci.* 211-223 (1976).
- 14 Skalny, J. & Tadros, M.E. Retardation of tricalcium aluminate hydration by sulfates. *J. Am. Ceram. Soc.* **60**, 174-175 (1977).
- 15 Minard, H., Garrault, S., Regnaud, L. & Nonat, A. Mechanisms and parameters controlling the tricalcium aluminate reactivity in the presence of gypsum. *Cem. Concr. Res.* **37**, 1418-1426 (2007).
- 16 Quennoz, A. & Scrivener, K. L. Hydration of C₃A–gypsum systems. *Cem. Concr. Res.* **42**, 1032-1041 (2012).
- 17 Holly, R., Peemoeller, H., Zhang, M., Reardon, E. & Hansson, C. M. Magnetic resonance in situ study of tricalcium aluminate hydration in the presence of gypsum. *J. Am. Ceram. Soc.* **89**, 1022-1027 (2006).
- 18 Hampson, C. J. & Bailey, J. E. The microstructure of the hydration products of tricalcium aluminate in the presence of gypsum. *J. Mater. Sci.* **18**, 402-410 (1983).
- 19 Jackson, M. D. *et al.* Material and elastic properties of Al-tobermorite in ancient Roman seawater concrete. *J. Am. Ceram. Soc.* **96**, 2598-2606 (2013).
- 20 Shapiro, D. A. *et al.* Chemical composition mapping with nanometre resolution by soft X-ray microscopy. *Nature Photon.* **8**, 765-769 (2014).
- 21 Yu, Y. S. *et al.* Dependence on Crystal Size of the Nanoscale Chemical Phase Distribution and Fracture in Li_xFePO₄. *Nano Lett.* **15**, 4282-4288 (2015).
- 22 Kilcoyne, A. L. D., *et al.* Interferometer-controlled scanning transmission X-ray microscopes at the Advanced Light Source. *J. Synchrotron Radiat.* **10**, 125-136 (2003).
- 23 Winarski, R. P., *et al.* A hard X-ray nanoprobe beamline for nanoscale microscopy. *J. Synchrotron Radiat.* **19**, 1056-1060 (2012).
- 24 Brisard, S., *et al.* Morphological quantification of hierarchical geomaterials by X-ray nano-CT bridges the gap from nano to micro length scales. *Am. Mineral.* **97**, 480-483 (2012).

- 25 Levitz, P. & Tchoubar, D. Disordered porous solids: from chord distributions to small angle scattering. *J. Phys. I*, **2**, 771-790 (1992).
- 26 Allen, A. J., Thomas, J. J. & Jennings, H. M. Composition and density of nanoscale calcium–silicate–hydrate in cement. *Nat. Mater.* **6**, 311-316 (2007).
- 27 Myers, R. J., L'Hôpital, E., Provis, J. L. & Lothenbach, B. Effect of temperature and aluminium on calcium (alumino) silicate hydrate chemistry under equilibrium conditions. *Cem. Concr. Res.* **68**, 83-93 (2015).
- 28 Walker, C. S., Savage, D., Tyrer, M. & Ragnarsdottir, K. V. Non-ideal solid solution aqueous solution modeling of synthetic calcium silicate hydrate. *Cem. Concr. Res.* **37**, 502-511 (2007).
- 29 Lothenbach, B. & Nonat, A. Calcium silicate hydrates: Solid and liquid phase composition. *Cem. Concr. Res.* **78**, 57-70 (2015).
- 30 Nonat, A. The structure and stoichiometry of CSH. *Cem. Concr. Res.* **34**, 1521-1528 (2004).
- 31 Black, L., Garbev, K., Beuchle, G., Stemmermann, P. & Schild, D. X-ray photoelectron spectroscopic investigation of nanocrystalline calcium silicate hydrates synthesised by reactive milling. *Cem. Concr. Res.* **36**, 1023-1031 (2006).
- 32 Soyer-Uzun, S., Chae, S. R., Benmore, C. J., Wenk, H. R. & Monteiro, P. J. Compositional evolution of calcium silicate hydrate (C–S–H) structures by total x-ray scattering. *J. Am. Ceram. Soc.* **95**, 793-798 (2012).
- 33 Richardson, I. G. Tobermorite/jennite-and tobermorite/calcium hydroxide-based models for the structure of CSH: applicability to hardened pastes of tricalcium silicate, β -dicalcium silicate, Portland cement, and blends of Portland cement with blast-furnace slag, metakaolin, or silica fume. *Cem. Concr. Res.* **34**, 1733-1777 (2004).
- 34 Merlino, S., Bonaccorsi, E. & Armbruster, T. The real structures of clinotobermorite and tobermorite 9 Å OD character, polytypes, and structural relationships. *Eur. J. Mineral.* **12**, 411-429 (2000).
- 35 Hamid, S. A. The crystal structure of the 11 Å natural tobermorite $\text{Ca}_{2.25}[\text{Si}_3\text{O}_{7.5}(\text{OH})_{1.5}] \cdot \text{H}_2\text{O}$. *Z. Kristallogr. Cryst. Mater.* **154**, 189-198 (1981).
- 36 Merlino, S., Bonaccorsi, E. & Armbruster, T. Tobermorites: their real structure and order-disorder (OD) character. *Am. Mineral.* **84**, 1613-1621 (1999).
- 37 Merlino, S., Bonaccorsi, E. & Armbruster, T. The real structure of tobermorite 11 Å normal and anomalous forms, OD character and polytypic modifications. *Eur. J. Mineral.* **13**, 577-590 (2001).
- 38 Bonaccorsi, E., Merlino, S. & Kampf, A. R. The crystal structure of tobermorite 14 Å (Plombierite), a C-S-H phase. *J. Am. Ceram. Soc.* **88**, 505–512 (2005).

- 39 Cong, X. & Kirkpatrick, R. J. ^{29}Si MAS NMR study of the structure of calcium silicate hydrate. *Adv. Cem. Based Mater.* **3**, 144-156 (1996).
- 40 Renaudin, G., Russias, J., Leroux, F., Frizon, F. & Cau-dit-Coumes, C. Structural characterization of C–S–H and C–A–S–H samples—part I: long-range order investigated by Rietveld analyses. *J. Solid State Chem.* **182**, 3312-3319 (2009).
- 41 Richardson, I. G. Model structures for C-(A)-S-H (I). *Acta Crystallogr. Sect. B-Struct. Sci.* **70** (2014).
- 42 Jennings, H. M. Refinements to colloid model of CSH in cement: CM-II. *Cem. Concr. Res.* **38**, 275-289 (2008).
- 43 Constantinides, G. & Ulm, F. J. The effect of two types of CSH on the elasticity of cement-based materials: Results from nanoindentation and micromechanical modeling. *Cem. Concr Res.* **34**, 67-80 (2004).
- 44 J. Krakowiak, K., Wilson, W., James, S., Musso, S. & Ulm, F.-J. Inference of the phase-to-mechanical property link via coupled X-ray spectrometry and indentation analysis: Application to cement-based materials. *Cem. Concr. Res.* **67**, 271–285 (2015).
- 45 Pelisser, F., Gleize, P. J. P. & Mikowski, A. Effect of the Ca/Si Molar Ratio on the Micro/nanomechanical Properties of Synthetic CSH Measured by Nanoindentation. *J. Phys. Chem. C.* **116**, 17219-17227 (2012).
- 46 Jennings, H. M., Thomas, J. J., Gevrenov, J.S., Constantinides, G. & Ulm, F. J. A multi-technique investigation of the nanoporosity of cement paste. *Cem. Concr. Res.* **37**, 329-336 (2007).
- 47 Constantinides, G. & Ulm, F. J. The nanogranular nature of C–S–H. *J. Mech. Phys. Solids.* **55**, 64-90 (2007).
- 48 Qomi, M. A., *et al.* Combinatorial molecular optimization of cement hydrates. *Nat. Commun.* **5**, (2014).
- 49 Pellenq, R. J. M., Lequeux, N. & Van Damme, H. Engineering the bonding scheme in C–S–H: The iono-covalent framework. *Cem. Concr. Res.* **38**, 159-174 (2008).
- 50 Manzano, H. *et al.* Confined water dissociation in microporous defective silicates: mechanism, dipole distribution, and impact on substrate properties. *J. Am. Chem. Soc.* **134**, 2208–2215 (2012).
- 51 Manzano, H., Dolado, J. S. & Ayuela, A. Elastic properties of the main species present in Portland cement pastes. *Acta Mater.* **57**, 1666-1674 (2009).
- 52 Shahsavari, R., Buehler, M. J., Pellenq, R. J. M. & Ulm, F. J. First-principles study of elastic constants and interlayer interactions of complex hydrated oxides: Case study of tobermorite and jennite. *J. Am. Ceram. Soc.* **92**, 2323-2330 (2009).

- 53 Oh, J. E., Clark, S. M., Wenk, H. R. & Monteiro, P. J. Experimental determination of bulk modulus of 14Å tobermorite using high pressure synchrotron X-ray diffraction. *Cem. Concr. Res.* **42**, 397-403 (2012).
- 54 Oh, J. E., Clark, S. M. & Monteiro, P. J. Does the Al substitution in C–S–H (I) change its mechanical property? *Cem. Concr. Res.* **41**, 102-106 (2011).
- 55 Jackson, M.D. *et al.* Unlocking the secrets of Al-tobermorite in Roman seawater concrete. *Am. Mineral.* **98**, 1669-1687 (2013).
- 56 Palomo, A., Grutzeck, M.W. & Blanco, M.T. Alkali-activated fly ashes: a cement for the future. *Cem. Concr. Res.* **29**, 1323-1329 (1999).
- 57 Juenger, M.C.G., Winnefeld, F., Provis, J.L. & Ideker, J.H. Advances in alternative cementitious binders. *Cem. Concr. Res.* **41**, 1232-1243 (2011).
- 58 Myers, R.J., Bernal, S.A., Gehman, J.D., Deventer, J.S. & Provis, J.L. The Role of Al in cross-linking of alkali-activated slag cements. *J. Am. Ceram. Soc.* **98**, 996-1004 (2015).
- 59 Shi, C., Roy, D. & Krivenko, P. *Alkali-activated cements and concretes* (CRC press, 2006).
- 60 Pegado, L., Labbez, C. & Churakov, S.V. Mechanism of aluminium incorporation into C–S–H from ab initio calculations. *J. Mat. Chem. A*, **2**, 3477-3483 (2014).
- 61 Manzano, H., Dolado, J.S. & Ayuela, A. Aluminum incorporation to dreierketten silicate chains. *J. Phys. Chem. B*, **113**, 2832-2839 (2009).
- 62 Renaudin, G., Russias, J., Leroux, F., Cau-dit-Coumes, C. & Frizon, F. Structural characterization of C-S-H and C-A-S-H samples—part II: Local environment investigated by spectroscopic analyses. *J. Solid State Chem.* **182**, 3320-3329 (2009).
- 63 Richardson, I.G., Brough, A.R., Brydson, R., Groves, G.W. & Dobson, C.M. Location of aluminum in substituted calcium silicate hydrate (C-S-H) gels as determined by ²⁹Si and ²⁷Al NMR and EELS. *J. Am. Ceram. Soc.* **76**, 2285-2288 (1993).
- 64 Myers, R.J., Provis, J.L. & Lothenbach, B. Composition–solubility–structure relationships in calcium (alkali) aluminosilicate hydrate (C-(N, K-) ASH). *Dalton Trans.* **44**, 13530-13544 (2015).
- 65 L’Hôpital, E., Lothenbach, B., Le Saout, G., Kulik, D. & Scrivener, K. Incorporation of aluminium in calcium-silicate-hydrates. *Cem. Concr. Res.* **75**, 91-103 (2015).
- 66 Jackson, M.D. *et al.* Material and elastic properties of Al-tobermorite in ancient Roman seawater concrete. *J. Am. Ceram. Soc.* **96**, 2598-2606 (2013).
- 67 Manzano, H., Dolado, J.S., Guerrero, A. & Ayuela, A. Mechanical properties of crystalline calcium-silicate-hydrates: comparison with cementitious C-S-H gels. *Phys. Status Solidi A*, **204**, 1775-1780 (2007).

- 68 Qomi, M.J.A., Ulm, F.J. & Pellenq, R.J.M. Evidence on the Dual Nature of Aluminum in the Calcium-Silicate-Hydrates Based on Atomistic Simulations. *J. Am. Ceram. Soc.* **95**, 1128-1137 (2012).
- 69 Manzano, H., Dolado, J.S., Griebel, M. & Hamaekers, J. A molecular dynamics study of the aluminosilicate chains structure in Al-rich calcium silicate hydrated (C-S-H) gels. *Phys. Status Solidi A*, **205**, 1324-1329 (2008).
- 70 Thomas, J.J. A new approach to modeling the nucleation and growth kinetics of tricalcium silicate hydration. *J. Am. Ceram. Soc.* **90**, 3282-3288 (2007).
- 71 Silva, D.A., Monteiro, P.J. Hydration evolution of C₃S-EVA composites analyzed by soft X-ray microscopy. *Cem. Con. Res.* **35**, 351-357 (2005).
- 72 Thomas, J.J., Allen, A.J. & Jennings H.M. Hydration kinetics and microstructure development of normal and CaCl₂-accelerated tricalcium silicate pastes. *J. Phy. Chem. C*, **113**, 19836-19844 (2009).
- 73 Stein, H.N. & Stevels, J.M. Influence of silica on the hydration of 3CaO·SiO₂. *J. App. Chem.* **14**, 338-346 (1964).
- 74 Avrami, M. Kinetics of phase change. I General theory. *J. Chem. Phy.* **7**, 1103-1112 (1939).
- 75 Constantinides, G. & Ulm, F.-J. The nanogranular nature of C-S-H. *J. Mech. Phy. Solids*, **55**, 64-90 (2007)
- 76 Taylor, R. *Characterization of C-S-H in early and late age systems containing admixtures* (PhD dissertation. University of Leeds, 2010).
- 77 Rodger, S.A., Groves, G.W., Clayden, N.J. & Dobson, C.M. Hydration of Tricalcium Silicate Followed by ²⁹Si NMR with Cross-Polarization. *J. Am. Ceram. Soc.* **71**, 91-96 (1988).

3. Materials and Methods

3.1 Materials

Preparing C₃A hydration system containing gypsum. Pure C₃A and hydrogarnet (C₃AH₆) powders were purchased from Mineral Research Processing (<http://www.mineralresearchprocessing.fr/>). Gypsum was purchased from Fisher Scientific (#S76764). The purities of these materials were verified by powder X-ray diffraction (XRD). Partially-hydrated C₃A samples were prepared by mixing gypsum, C₃A and nanopure water in sealed plastic vials at room temperature (25 ± 2 °C) and agitated frequently by hand and/or constantly by mechanical rotation until further sample preparation and analysis. The initial mass ratio of C₃A to gypsum is 1:0.4. A w/s = 10 was selected to fit the requirement of most experiments. A w/s = 1 was also used for the X-ray ptychography experiments to verify the influence of dilution. Ettringite and \bar{S} -AFm were independently prepared by precipitation from stoichiometric mixtures of C₃A, gypsum and water. All reference minerals were characterized by XRD, and the purities were further verified by Rietveld refinement with software *HighScorePlus* and ICSD database (C₃A #1841, ettringite #16045, \bar{S} -AFm #100138, C₃AH₆ #62704 and gypsum #2058), as shown in Figure 3.1.

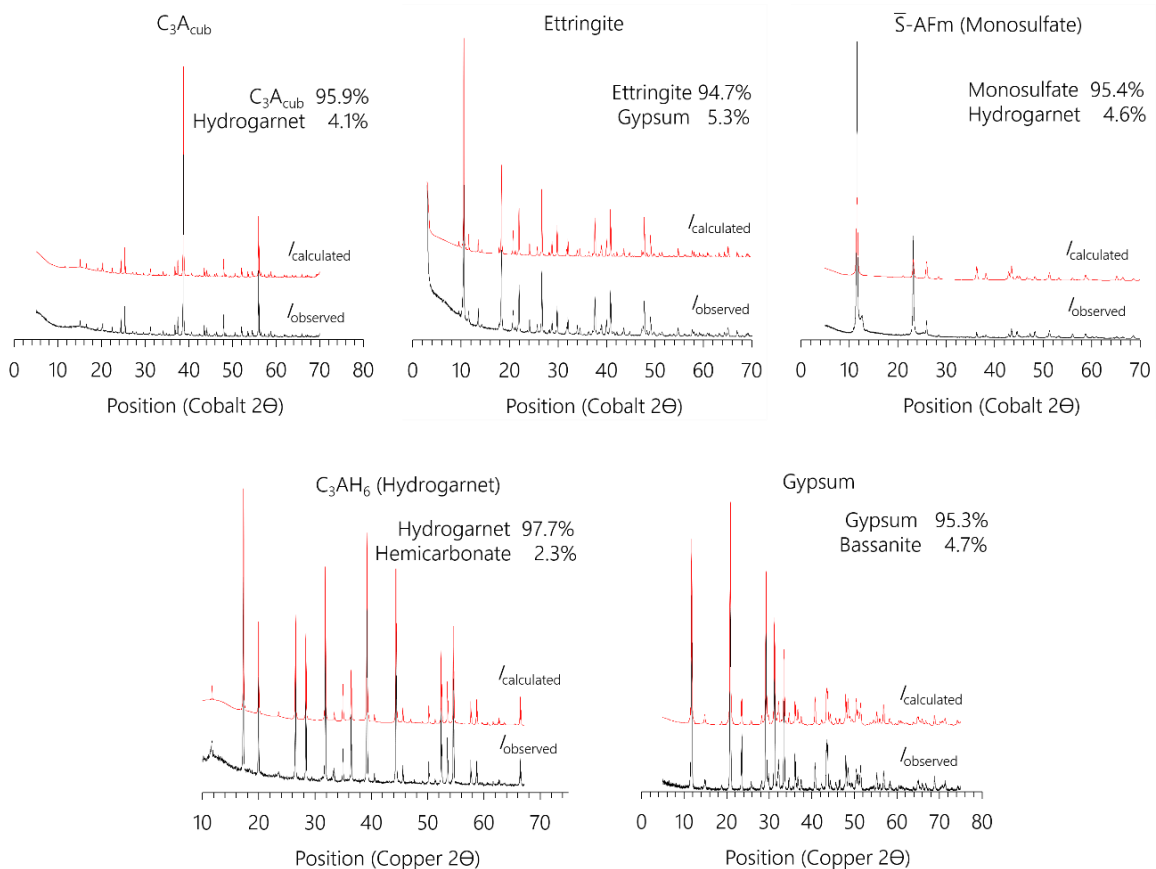


Figure 3.1 Powder XRD and Rietveld refinement of reference minerals.

For SEM experiments, C₃A powder was spread on carbon tape pieces attached to steel SEM sample holders, which were then immersed into saturated gypsum water solution for up to 240 s. The hydrated samples were then immediately rinsed with large quantities of 99.5% ethanol and dried in N₂ atmosphere. Samples were carbon coated before being placed in SEM chamber.

For STXM and ptychographic study, partially hydrated C₃A samples prepared as described above were drop-cast onto 100 nm-thick Si₃N₄ windows (Norcada™), with excess solution removed using Kimwipes (Kimtech Science™). Samples were immediately transferred to the vacuumed STXM chamber. This drop-cast method is applied to all preparations of STXM and ptychographic samples, which will not be repeated later on.

Synthesizing nano-crystalline C-S-H and C-A-S-H. C-S-H samples with bulk Ca/Si=0.80, 0.98 and 1.29 (labeled 0.8CSH, 1.0CSH and 1.3CSH, respectively) were synthesized by mixing stoichiometric amounts of CaO (obtained by burning CaCO₃ (Merck Millipore) at 1000 °C for 12 h), SiO₂ (Aerosil 200, Evonik) and nano-pure water (Merck Millipore) in high density polyethylene bottles at a water to solid ratio = 45. The bottles were shaken at 100 rpm for 182 days. Solids were then collected by vacuum filtration in an N_{2(g)}-filled glove box using 0.45µm nylon filters, washed with a 50% v/v ethanol / nano-pure water (Merck Millipore) solution and then with ≥94 vol.% ethanol, freeze-dried for seven days, and then stored in N_{2(g)}-filled desiccators in the presence of a saturated CaCl₂ solution (≈30% RH) and solid NaOH as a CO₂ trap. In an order of increasing Ca/Si ratio, samples were labeled 0.8CSH, 1.0CSH and 1.3CSH; the mean dreierketten chain lengths (MCL) are 19, 5 and 2 (as characterized by NMR), corresponding to 15%, 50% and 100% bridging site omission.

Similar to the preparation of C-S-H, synthesis of C-(A-)S-H was performed using an initial bulk Ca/Si molar ratio of 1.0 and initial bulk Al/Si molar ratios of 0, 0.05 and 0.1 (labeled Al0, Al05, and Al10, respectively) by mixing stoichiometric amounts of SiO₂, CaO and CaO · Al₂O₃ at a water/solid ratio of 45 in a N₂-filled glove box. The mixtures were stored in Teflon bottles at 80 °C and shaken twice a week for 56 days. The solid C-(A-)S-H were vacuum filtered using 0.45µm nylon filters, freeze-dried for 7 days, and then stored in N₂-filled desiccators in the presence of saturated CaCl₂ solutions (≈ 30% R.H.) and NaOH (CO₂ trap). The MCL of the Al0 and Al10 samples were measured to be 8.8 and 19.8, respectively.

Synthesizing the 50-year-old C₃S hydrates. Synthesized alite (96% C₃S) and distilled water were mixed at w/c=0.5, and cast into a 2-inch-long, 0.5-inch-diameter cylindrical mold fifty years ago. For the first three years after mixing, the sample was stored in saturated Ca(OH)₂ water solution at room temperature. After that the sample was kept in a sealed plastic container, cured at room temperature for 47 years. To investigate the evolution of C-S-H, a 1.5-year-old sample was also prepared before the STXM experiment, by mixing pure C₃S with distilled water at w/c=5.0. Such a high water to cement ratio was

used, so that the suspension could be studied by STXM in an *in-situ* way. Hydrated C₃S particles were kept in their original morphology. The paste was ground to powders, which were used to prepare STXM, SEM, NMR and lab XRD samples.

3.2 Experimental methods

Scanning Electron Microscope (SEM). A ZEISS EVO® MA10 SEM, coupled with an Energy Dispersive X-ray Spectrometer (EDX), is used in second electron mode at 5 kV and 7 pA (to optimize the resolution), and in back scattered electron mode at 15 kV and 500 pA (to obtain enough signal-to-noise ratio).

Lab XRD was used to characterize the purity of raw materials used to synthesize the C₃A+gypsum hydration system; the 50-year-old C₃S paste was also studied using lab XRD. The experiments were performed with PANalytical X'Pert Pro diffractometer, operating at 40 keV and 40 mA with a Cobalt anode. The 2-theta scanning range was between 5 ° to 100 °, with a step width of 0.0167 ° and collection time of 0.475 second per step. Software *HighScore (Plus)* was used to identify the peak positions.

²⁹Si Magic Angle Spinning Nuclear Magnetic Resonance (MAS-NMR) was conducted on the 50-year-old C₃S paste. A section of the sample taken from the core was finely ground and packed evenly into a 4-mm zirconia rotor and sealed at the open end with a Vespel cap. The rotor was spun at 14 kHz on a Bruker Ultrashield 400.13 WB Plus with a 9.2 T magnet operating at 79.495 MHz for ²⁹Si and a dwell time of 10 μs, 2048 acquisitions were obtained in all cases. In order to obtain quantitative data a recycle delay of 30 seconds was used, which allowed for full relaxation of the signal. The magic angle was set to 54.734 °, using KBr as a reference. The quantitative information on the fractions of silicon ions present in silicate tetrahedra with different connectivities was obtained by deconvolution of the single-pulse spectrum. In this work, the spectrum were fitted by the iterative fitting of the hydrate peaks to Voigt lineshapes using IgorPro 6.35A5 (Wavemetrics, Inc., USA).

²⁹Si NMR was also conducted for the synthesized C-(A-)S-H samples by the collaborative of relevant projects. The experimental details and results have been well summarized in published work^{1,2}, and will not be repeated here.

Transmission Electron Microscope (TEM) was conducted on the 50-year-old C₃S paste. Fine powders were scraped from the core of the cylinder, and suspended with ethanol. The suspension was then deposited on a carbon film and air-dried for 5 min. Ten-nm-diameter gold particles coated the carbon film to assure proper alignment of the reconstruction. A Titan CT TEM, equipped with *Xplore3D* tomography software was used. To ensure no Ca(OH)₂ (CH) particles exist, which will cause strong scattering, the diffraction pattern was investigated before the tomography measurement was conducted. The rotation range was set as 0 to -65 ° and 0 to +65 °, which collected 361 projection images that were then aligned using IMOD software³.

STXM. The STXM experiments were conducted at beamline 5.3.2.2 (C *K*-edge and Ca *L*_{2,3}-edge) and 5.3.2.1 (Al and Si *K*-edge, and ptychographic imaging) of the ALS. For C *K*-edge study, the incident beam energy was scanned from 240 eV to 310 eV with step size 0.1 eV; for Ca *L*_{2,3}-edge the beam is scanned from 340 eV to 360 eV with step size 0.1 eV; for Al *K*-edge, from 1552 to 1605 eV with step size 0.1 eV from 1565 to 1594 eV and step size 0.3 eV over the other energy ranges. A dwell time of 3s was used for linear scan mode, and 5-10s for point-by-point scan model.

STXM data can be collected in several ways. a) Image can be generated from the absorption data of each pixel. In this case, the beam energy is fixed and the scanning is only conducted in spatial dimension. The data is converted to optical density (OD) image through the Beer-Lambert law: $OD = -\ln[I/I_0]$, where I is the intensity of the transmitted beam and I_0 is the incidence beam intensity. A bright area on the OD image indicates a large absorption. Note that the amount of absorption is affected to by three factors: density, thickness and the absorption coefficient. Specially, the absorption coefficient can be largely increased to a significant degree when the incident beam energy reaches the absorption edge of certain elements, as explained earlier; b) Line scan data can be obtained by scanning both the incident beam energy (within the range of about 60 eV and centered at the absorption edge) and spatial dimension along a straight line on the sample. Line-scan data yield the NEXAFS spectra of each pixel on that line; and c) A stack scan, which is the most complete scan, measures the NEXAFS on each pixel over the whole image. The image stack was aligned and analyzed with the aXis2000 software.⁴

X-ray ptychography was conducted using the same STXM setup in beamline 5.3.2.1 of ALS. For these measurements, a 60 nm outer-zone-width zone plate focused a coherent soft X-ray beam (750-800 eV) onto the sample, which was scanned in 40 nm increments to ensure overlap of the probed areas. The effects of incoherent background signals were eliminated by implementing a background retrieval algorithm that iteratively determines a constant offset to the diffraction data. The sample was aligned with respect to the zone plate through an interferometric feedback system. A pixel size of 5 nm was used in image reconstruction. The reported resolution of beamline 5.3.2.1 is 5 nm.⁵ With an ImageJ plugin code, the small angle scattering calculations were performed using the ptychography images as input (algorithm available in appendix).

In-situ WAXS and SAXS. In-situ WAXS and SAXS experiments were conducted at the WAXS/SAXS beamline of the Synchrotron Light Research Institute (SLRI), Thailand, which runs at 1.2 GeV and 75-125 mA. For measurements, an incident beam of 9 keV was transmitted through two pieces of kapton™ film between which the sample was placed, measuring from 2 to 120 min of hydration. The q -range covered was 0.04 to 42 nm⁻¹ for WAXS and 0.07 to 0.7 nm⁻¹ for SAXS, both with an angular step size 0.25 °.

TXM tomography. The TXM projections were collected at the Hard X-ray Nanoprobe Beamline, operated by the Center for Nanoscale Materials at Sector 26 of the Advanced Photon Source.⁶ A cluster of partially-hydrated C₃A samples was mounted on a tungsten

needle tip and placed on multi-directional scanning stage. The incident beam was tuned to 9 keV and condensed by an elliptically shaped single-reflection glass capillary with a central stop. Transmission images were recorded while the sample was rotated from -90° to 90° . Ten images were collected at every 1° step, with an exposure of 10 s at each step to obtain better averaging statistics. The mathematical algorithm of reconstruction is available in the appendix.

High pressure XRD. The HP-XRD experiment was conducted at beamline 12.2.2 of the Advanced Light Source (ALS) in Lawrence Berkeley National Laboratory (LBNL). Stainless steel gaskets and diamond anvils of culet diameter $\sim 300 \mu\text{m}$ were used in an axial Merrell-Bassett cell. The gaskets were pre-indented using diamond anvils before laser drilling holes through the centers of the indented regions to create cylindrical chambers of diameter $150 \mu\text{m}$ and height $\sim 100 \mu\text{m}$ (one for each gasket). Small amount of ruby powder ($\alpha\text{-Al}_2\text{O}_3$ doped with 0.05 wt.% Cr^{3+}) was used as pressure calibration and mixed with sample in the chamber. The chamber was then filled with methanol-ethanol (volumetric ration 4:1), followed by immediate closing with diamond culets. The methanol-ethanol solution intrudes pores of $\sim 1 \text{ nm}$ in diameter⁷ and therefore generates hydrostatic pressure on porosity-free nano-crystalline C-S-H. Up to $\sim 10 \text{ GPa}$ hydrostatic pressure was generated by applying load on the diamond anvils in the direction parallel to incident beam path, with a step size of 1-2 GPa. Pressure was calibrated using the ruby fluorescence signal.⁸ XRD patterns were recorded on MAR345 detector, with the center positions and sample-to-detector distance calibrated by standard material LaB_6 , the. The raw diffraction data were integrated using the Dioptas software⁹. The incident beam energy was set to $\sim 25 \text{ keV}$ and the wavelength was calibrated to be 0.49755 \AA . Rietveld refinement was performed using the MAUD software.¹⁰

The change in molar volume of each solid phase in the sample, induced by the applied hydrostatic pressure, is linked to the bulk modulus by the 2nd order Birch-Murnaghan equation of state (BM-EoS)¹¹:

$$P = \frac{3}{2}K_0 \left[\left(\frac{V}{V_0} \right)^{-\frac{7}{3}} - \left(\frac{V}{V_0} \right)^{-\frac{5}{3}} \right] \quad (3-1)$$

where V_0 is the unit cell volume at ambient pressure; V is the unit cell volume under applied hydrostatic pressure P ; K_0 is the ambient bulk modulus. This equation is valid when the first pressure derivative of K_0 is 4, which is often assumed in order to more confidently fit K_0 .¹² By defining volumetric strain $\varepsilon_V = 1 - V/V_0$, Eq. (3-1) is rewritten as:

$$P = \frac{3}{2}K_0 \left[(1 - \varepsilon_V)^{-\frac{7}{3}} - (1 - \varepsilon_V)^{-\frac{5}{3}} \right] \quad (3-2)$$

Atomistic simulations. Atomistic models of 0.8CSH and 1.0CSH were proposed based on a $2 \times 2 \times 1$ supercell of 14 \AA tobermorite structure¹³; model of 1.3CSH was based on a $2 \times 2 \times 2$ supercell of 9 \AA tobermorite structure¹⁴. The bridging site SiO_4 tetrahedron was omitted to match NMR data. The Ca/Si ratio was then adjusted by modifying the amount of Ca in the

interlayer space. The amount of water molecules were determined so that the initial interlayer spacings at ambient pressure match the values refined from XRD (appendix). The GULP energy minimization algorithm package was used, so that each model was relaxed under constant hydrostatic pressure values from 0 to 8 GPa. The potential functions used in this study, and preliminary molecular calculations to validate the starting model are summarized in the appendix.

3.3 References

- 1 Myers, R. J., L'Hôpital, E., Provis, J. L. & Lothenbach, B. Effect of temperature and aluminium on calcium (alumino) silicate hydrate chemistry under equilibrium conditions. *Cem. Concr. Res.* **68**, 83-93 (2015).
- 2 L'Hôpital, E., Lothenbach, B., Le Saout, G., Kulik, D. & Scrivener, K. Incorporation of aluminium in calcium-silicate-hydrates. *Cem. Concr. Res.* **75**, 91-103 (2015).
- 3 Kremer, J.R., Mastrorade, D.N. & McIntosh, J.R., Computer visualization of three-dimensional image data using IMOD. *J. Struct. Bio.* **116**, 71-76 (1996).
- 4 Hitchcock, A. P. *et al.* aXis 2000 — Analysis of X-ray images and spectra. <http://unicorn.mcmaster.ca/aXis2000.html> (2012).
- 5 Shapiro, D. A. *et al.* Chemical composition mapping with nanometre resolution by soft X-ray microscopy. *Nature Photon.* **8**, 765-769 (2014).
- 6 Winarski, R. P., *et al.* A hard X-ray nanoprobe beamline for nanoscale microscopy. *J. Synchrotron Radiat.* **19**, 1056-1060 (2012).
- 7 Juenger, M. C. G. & Jennings, H. M. The use of nitrogen adsorption to assess the microstructure of cement paste. *Cem. Concr. Res.* **31**, 883-892 (2011).
- 8 Piermarini, G. J., Block, S., Barnett, J. D. & Forman, R. A. Calibration of the pressure dependence of the R1 ruby fluorescence line to 195 kbar. *J. Appl. Phys.* **46**, 2774-2780 (1975).
- 9 Prescher, C. & Prakapenka, V. B. DIOPTAS: a program for reduction of two-dimensional X-ray diffraction data and data exploration. *High Pressure Res.* **35**, 223-230 (2015).
- 10 Lutterotti, L., Matthies, S. & Wenk, H. R. MAUD: a friendly Java program for material analysis using diffraction. *IUCr: Newsletter of the CPD.* **21**, 14-15 (1999).
- 11 Birch, F. Elasticity and constitution of the Earth's interior. *J. Geophys. Res.* **57** (1952).
- 12 Oh, J. E., Clark, S. M., Wenk, H. R. & Monteiro, P. J. Experimental determination of bulk modulus of 14Å tobermorite using high pressure synchrotron X-ray diffraction. *Cem. Concr. Res.* **42**, 397-403 (2012).

- 13 Bonaccorsi, E., Merlino, S. & Kampf, A. R. The crystal structure of tobermorite 14 Å (Plombierite), a C-S-H phase. *J. Am. Ceram. Soc.* **88**, 505–512 (2005).
- 14 Merlino, S., Bonaccorsi, E. & Armbruster, T. The real structures of clinotobermorite and tobermorite 9 Å OD character, polytypes, and structural relationships. *Eur. J. Mineral.* **12**, 411-429 (2000).

4. Early-age hydration mechanism of cubic C₃A in the presence of gypsum

This chapter focuses on the early age performance of freshly-mixed concrete, which critically depends on the hydration of tricalcium aluminate (C₃A). Gypsum addition to cement retards the rapid hydration of C₃A, although its underlying chemical mechanism(s) remains unclear. There exists an intense debate whether the retardation (and hence lack of C₃A dissolution) is due to an ion diffusion barrier at the C₃A-water interface, or due to that the active dissolution site on C₃A is passivated by sulfate adsorption. This chapter aims to provide nanoscale morphological, chemical and crystallographic information of the diffusion-precipitation frontier of C₃A particles, in order to test the existing hypothesis. Partially hydrated C₃A particles with different water to solid mass ratio (w/s) ratios, and at various ages in the induction period, are investigated as described in Chapter 3. The crystalline compositions were tracked by SAXS study of an in-situ hydration system. Morphological information was quantified by ptychographic imaging (2D) and nano-CT (3D). A phase mapping is conducted using STXM and Al K-edge NEXAFS. A summary of the scientifically findings and their potential impact are discussed right after the technical contents.

4.1 In-situ chemistry and crystallography of the initial hydration of C₃A in the presence of gypsum

Figure 4.1a-c shows that the surface morphology of C₃A changes greatly during initial hydration in the presence of gypsum. The first dominant hydration product has foil/flake-like morphology to coat C₃A in the first minute (≤ 80 s), which is then masked by needle-like ettringite precipitates by 240 s. The flake-like precipitates have 200-300 nm thickness at their edges and previous researchers have reported to be poorly-crystalline AFm phases^{1,2}. As shown in Figure 4.1d, the synchrotron-radiation based WAXS measures the X-ray diffraction of the C₃A+gypsum system in an in-situ way, from 2 to 120 min. Only the diffraction of remnant C₃A and gypsum, and a small quantity of ettringite are detected throughout the measured time duration³⁻⁸. The intensities of the major peaks of C₃A and gypsum vary slightly with respect to the absolute values, whereas the intensity of ettringite diffraction increases monotonically with increasing hydration time. The characteristic peaks of OH-AFm phase (e.g. C₄AH₁₉) at 10.7 Å, (red arrow in Figure 4.1d)⁶, \bar{S} -AFm at 8.97 Å (blue arrow)⁷ are not observed for the first 120 min hydration, indicating that the initially-formed AFm-type flakes are too poorly crystalline to generate detectable diffraction or are gradually decomposed with increasing hydration time. The conversion of OH-AFm to C₃AH₆ (4.44, 3.35 and 3.14 Å (green arrows)⁸) are also not observed.

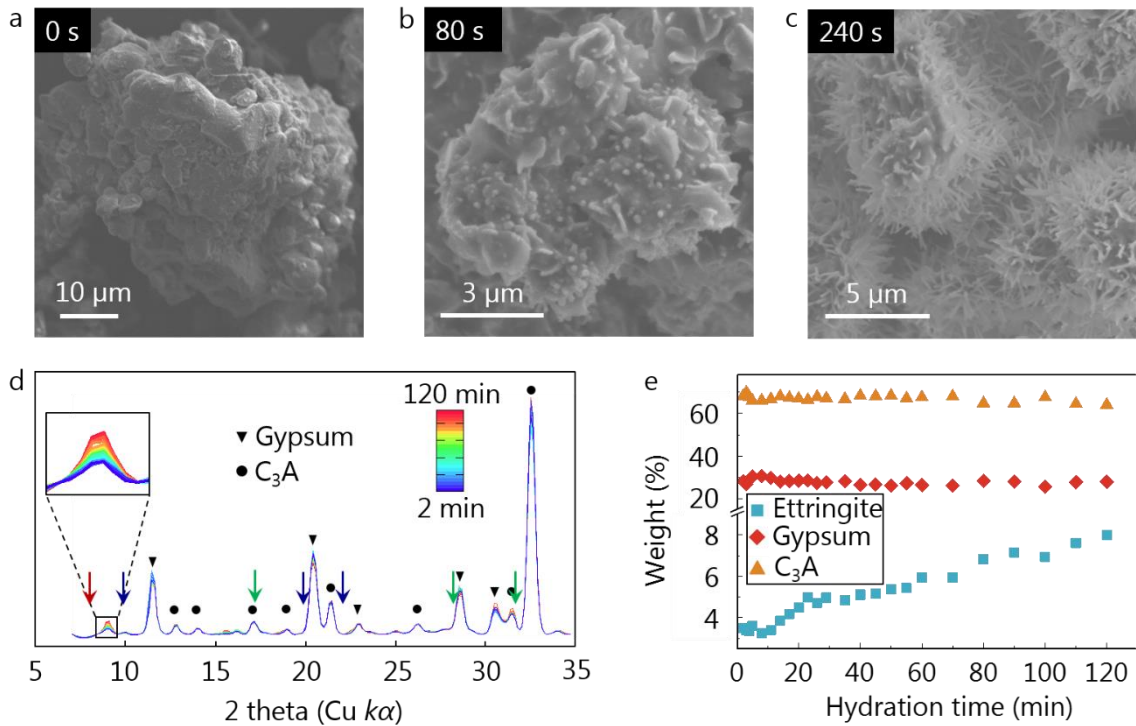


Figure 4.1 SEM and in-situ WAXS results of C_3A hydration in the presence of gypsum. SEM images of C_3A particles **a**, before hydration, and hydrated for **b**, 80 s and **c**, 240 s. **d**, WAXS results of the sample hydrated from 2 to 120 min, plotted in color series as indicated. C_3A and gypsum diffraction peaks are labeled with triangles and circles, respectively. The inset is a magnification of the major diffraction peak of ettringite. The red, blue and green arrows denote the characteristic diffraction peaks of C_4AH_{19} , \bar{S} -AFm and C_3AH_6 , respectively. **e**, Evolution of the weight percentages of ettringite, gypsum and C_3A during hydration.

Weight percentages of individual phases are calculated through Rietveld refinement (Figure 4.1d, details available in appendix). Within the hydration time studied, the amounts of C_3A and gypsum remain almost constant. Ettringite forms at a rate of ~ 2 wt.% per hour with respect to the total crystalline solid mass, reaching 8 wt.% at 120 min. There is an initial rapid initial formation of 3.5 wt.% ettringite before the first 2 min of hydration. As vast amount of initial flake-like precipitates precede these ettringite needles, it seems unlikely that these flake-like precipitates act as a diffusion barrier to retard the precipitation of ettringite within the first 2 min of hydration. However, it is still unclear whether a gel layer persists as a diffusion barrier at the dissolution frontier of C_3A throughout the induction period, as it may be XRD-transparent, and is masked in the SEM images by ettringite needles.

4.2 Spectromicroscopy of C₃A hydrated in the presence of gypsum during the induction period

STXM is a promising tool to study the chemistry at the dissolution frontier of C₃A with nanometer spatial resolution. Unlike XRD, STXM would pick up the signal if there is an amorphous layer on the surface of C₃A particles. Using STXM at the Al *K*-edge (1575 eV), eight regions parallel to the dissolution/precipitation frontier (Figure 4.2a), labeled B1-B8, were chosen to analyze the chemistry of the C₃A dissolution frontier. In Al *K*-edge XANES spectra, peaks A, C and E correspond to the transitions of 1*s* to 3*s*-like, 3*p*-like and 3*d*-like states, respectively, and peak D corresponds to multi-scattering within adjacent neighbor shells.⁹ The transition of 1*s* to the 3*s* state is forbidden by the selection rule but is observable if the tetrahedron coordination is distorted and permits a mixture of Al *s* and *p* states. In good agreement with other Al-bearing minerals,⁹⁻¹² the position of peak C is a few eV lower for tetrahedral Al (Al[4]) in C₃A³ than for octahedral Al (Al[6]) in possible solid hydration products i.e. ettringite⁴, \bar{S} -AFm⁷, C₄AH₁₃¹³ (dehydration of C₄AH₁₉ is most likely to happen in vacuum condition¹⁵) and C₃AH₆⁸ (Figure 4.2b). The unique features of the reference spectra allow us to determine the identity of the solid hydration product(s).

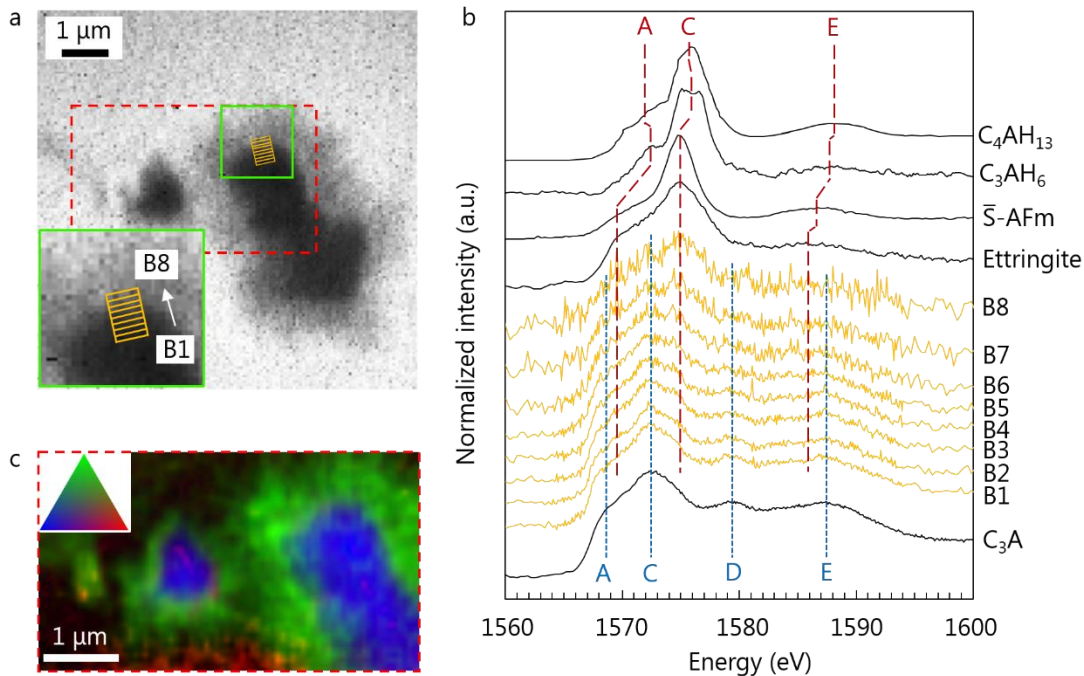


Figure 4.2 STXM and Al *K*-edge XANES results of C₃A hydrated for 150 minutes in the presence of gypsum. **a**, An X-ray absorption contrast image at 1575 eV, with XANES data collected for each pixel (the pixel size is $\sim 70 \times 70$ nm). Eight segments ($\sim 100 \times 700$ nm), marked by yellow rectangles labeled B1 (bottom) to B8 (top), are selected to sample a continuous region including unhydrated C₃A and the solid hydration product (inset is magnification of the green-boxed region in the main image). **b**, Al *K*-edge of XANES

spectra for each area B1-B8 (yellow curves), C_3A and several possible Al-containing solid hydration products.¹⁴ Resonance peaks for Al[4] and Al[6] are marked by short-dashed blue and long-dashed red lines, respectively. The spectrum of C_4AH_{13} is adapted from published work¹¹. **c**, Phase composition mapping of the region outlined by the dashed red rectangle in **a**, where green, blue and red shaded areas correspond to ettringite, C_3A and decomposition residue, respectively. Inset is a RGB color-triangle for reader convenience.

In the Al *K*-edge XANES spectra of B1-B8, the intensities of the Al[4] peaks (blue short-dashed lines) A (1568.6 eV), C (1572.5 eV), D (1579.3 eV) and E (1587.4 eV) decrease and the Al[6] peaks (red long-dashed lines) C (1574.9 eV) and E (1585.9 eV) grow as functions of increasing distance away from the remnant C_3A particle (Figure 4.2b). The spectra collected in regions B1 and B2 have almost identical features as the Al *K*-edge XANES spectrum of C_3A and show strong intensities at the energies of its major tetrahedral Al (Al[4]) peaks A, C, D and E, indicating that these regions contain predominantly remnant C_3A . The positions of the growing Al[6] peaks C and E match with the corresponding peaks and positions for ettringite (1574.9 and 1585.9 eV respectively) rather than C_3AH_6 (1576.0 and 1588.0 eV respectively) and C_4AH_{13} (1575.8 and 1588.2 eV respectively). The position of peak E in B1-B8 also does not match the location of this peak in the spectrum for \bar{S} -AFm, at 1587.0 eV. Compared to the intensities and shapes of peaks C and A in the spectrum for ettringite, peak C (1574.7 eV) is significantly sharper and peak A (1569.4 eV) is much weaker in spectrum of \bar{S} -AFm. Therefore, regions B3–B6 contain significant amounts of C_3A (Al[4]) and ettringite (Al[6]) and regions B7–B8 contain predominantly ettringite (Al[6]). After 150 minutes of hydration, ettringite is the only precipitate at the surface of the C_3A particle analyzed here.

The Al *K*-edge XANES of the full imaged region is well-fitted using the spectra of C_3A (green) and ettringite (blue), with only a small residual signal (red) in the background region that is thus assigned to measurement noise. This result further demonstrates that ettringite is the only solid hydration product here (Figure 4.2c). There is no trace of AFm phases, although flake-like AFm dominate the surface morphology at initial hydration (Figure 4.1b). There is also no trace of a more stable phase C_3AH_6 generated from the conversion of OH-AFm phases. This ettringite layer is ~ 1 μm thick on the bigger C_3A particle (Figure 4.2a, right-hand-side), and slightly thinner on the smaller one (Figure 4.2a, left-hand-side). A needle-like morphology characteristic of ettringite is not clearly observed at this resolution, as the precipitated ettringite crystallites have characteristic dimensions at or below the pixel resolution (i.e. ~ 70 nm).

4.3 Meso-scale morphological evolution of solid hydration products using X-ray ptychographic imaging and in-situ SAXS

X-ray ptychographic imaging is used here to observe the morphology of the C_3A dissolution frontier (Figure 4.3). The image resolution better than ~ 17 nm is determined by Fourier ring correlation (appendix). Needle-like ettringite precipitates studied here are

observed with uniform thickness from 30 to 620 min in the water to solid mass ratio (w/s) = 10 system (Figure 4.3a-c). The population of ettringite needles increases with increasing hydration time, but individual needles generally all grow to a maximum length of $\sim 1 \mu\text{m}$, with also no significant thickening. Ettringite prefers to nucleate on C_3A particles instead of precipitating through-solution, and generally grow perpendicular to the C_3A surface (dashed blue squares). The needle network is densified through interlacing of ettringite needles in confined regions (dashed yellow squares). After 620 min hydration, the transition from the layer of ettringite needles to the remnant C_3A is continuous and no physical barrier of distinct grey scale is observed in the interfacial zone (insets in Figure 4.3c), i.e. ettringite precipitates directly on rough, partially-dissolved C_3A surfaces.

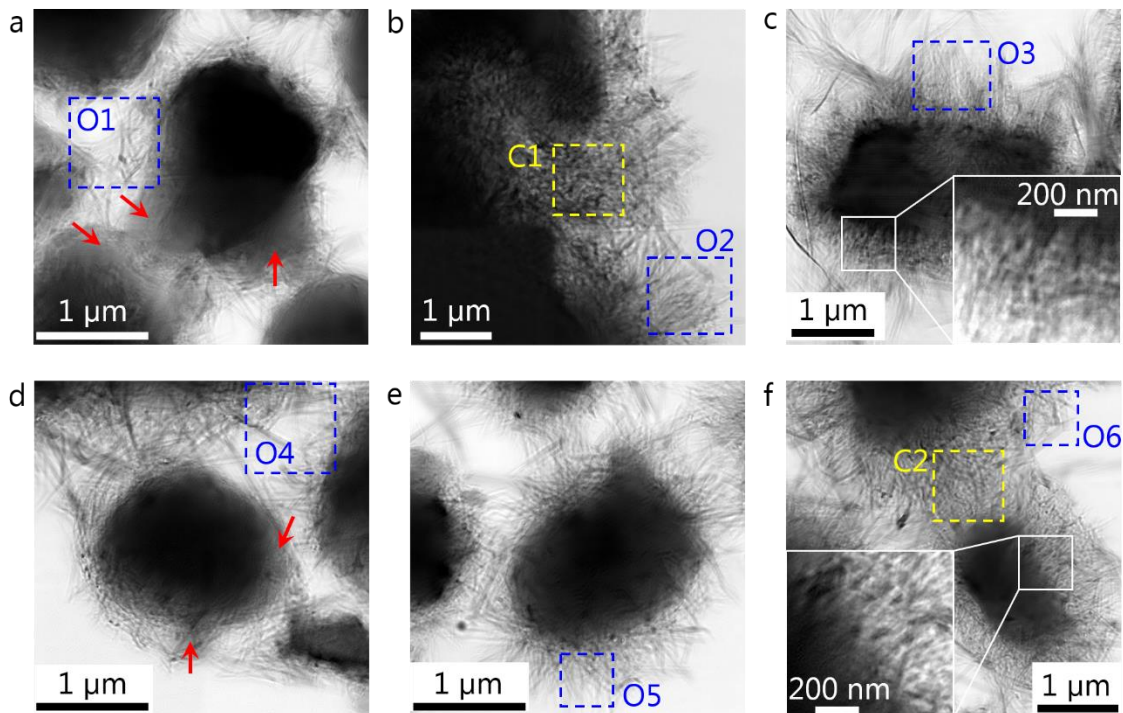


Figure 4.3 X-ray ptychographic images of C_3A hydrated in the presence of gypsum and $w/s = 10$ (a-c), and $w/s = 1$ (d-f), at hydration times of: **a**, 30 min; **b**, 135 min; **c**, 620 min; **d**, 30 min; **e**, 90 min; and **f**, 910 min. The reconstructed pixel size is $5 \times 5 \text{ nm}^2$. Blue and yellow squares indicate needle-like ettringite precipitation on open C_3A surfaces and confined spaces between particles, respectively. Red arrows indicate gel-like hydration product at early hydration (< 30 min). The white box insets in c and f are magnified regions of the interface between remnant C_3A and hydration product.

The morphologies of the C_3A dissolution frontier in the $w/s = 10$ (Figure 4.3a-4c) and $w/s = 1$ (Figure 4.3d-f) systems are similar: ettringite needles reach a length of $\sim 1 \mu\text{m}$ after 910 min hydration and thicken negligibly in the $w/s = 1$ system. A solid ‘diffusion barrier’ is not identified at 910 minutes of hydration (Figure 4.3f inset). C_3A hydration kinetics is

reported to be independent of the w/s between 1 and 10.^{16,17} In both w/s systems, there exist areas on the particle surfaces that have distinct grey scale values as the remnant C₃A and with dimension of a few hundred nanometers. These ‘gel-like’ materials are assigned to the flake-like AFm phases due to the highly morphological similarity as shown in SEM images (Figure 4.1b). They are observed intermixed with ettringite needles on C₃A surface at 30 minutes of hydration (red arrows in Figure 4.3a and 3d), but are not observed at later age of induction period under transmission microscope. Therefore the initially formed AFm flakes destabilizes to form ettringite during the induction period and so cannot act as physical diffusion barrier to retard C₃A dissolution throughout this period. This interpretation is consistent with the STXM and Al *K*-edge XANES results.

To quantify the morphology of the ettringite that precipitates under different spatial confinement, theoretical calculations of SAS (algorithm available in appendix) are applied to the selected dashed blue (O1-O6, open spaces) and yellow (C1-C2, confined regions) square regions in Figure 4.3, and are compared with in-situ SAXS measurement of the w/s = 1 system (Figure 4.4). The calculated SAS results generally resemble the in-situ SAXS results, and both can be interpreted using the form factor of a typical Guinier-Porod pattern of agglomerated isometric rods or cylinders.¹⁸ In a log-log plot of the intensity vs. scattering vector (q), the q_1 and q_{cutoff} values define the lower and higher end, respectively, of a linear Porod region with slope between -4 and -3, which corresponds to the surfaces fractal. For $q < q_1$, a nonlinear Guinier region with slope ranging from -1 to -3 is defined, corresponding to the volume fractal. Due to the limitation of the SAXS experimental setup and the overall size of the selected ptychographic image regions ($\sim 1 \mu\text{m}^2$ here), the low- q end of the Guinier region here is not small enough to reliably probe the scale equal or larger than the needle length ($\sim 1 \mu\text{m}$).

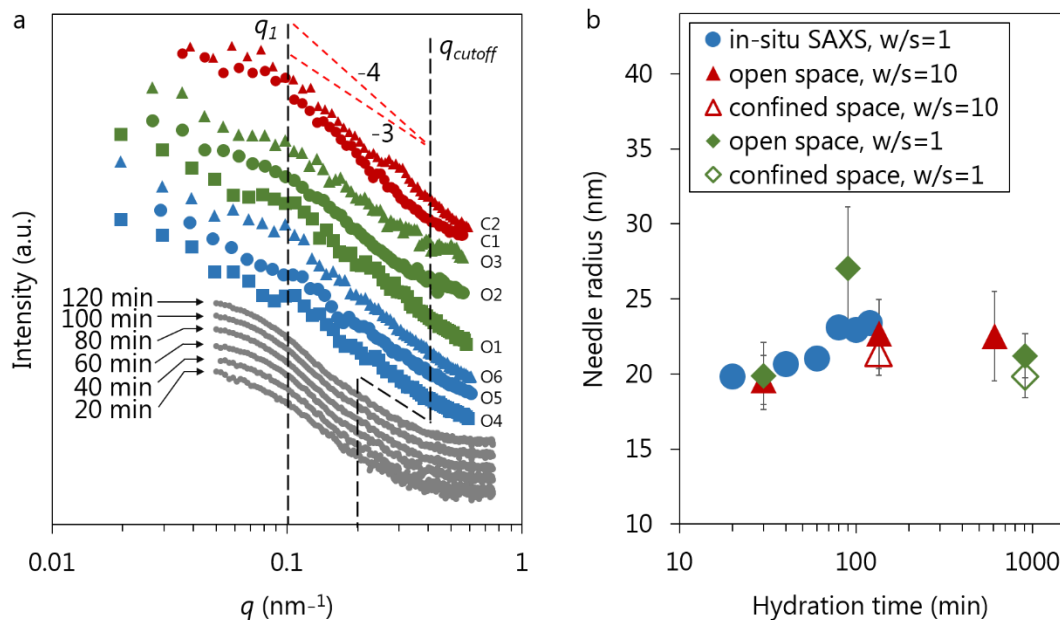


Figure 4.4 Morphology of C₃A particles hydrated in the presence of gypsum as quantified using SAS. **a**, In-situ SAXS results from 20 to 120 min, using the SAXS at 2 min hydration as the background signal of mainly liquid water, C₃A and gypsum. SAS were also calculated from the regions marked by dashed squares in the ptychographic images. The q_1 (intersection between lower- q Guinier region and higher- q Porod region) and q_{cutoff} (high- q end of Porod region) are schematically marked with black long-dashed lines. Red short-dashed lines with slope -4 and -3 are displayed as eye guides. **b**, Evolution of the radii of ettringite precipitates, with the uncertainty denoted by error bars and marker size. The uncertainty is derived from the fitting of q_1 and d .

The needle-like ettringite precipitates are of isometric radius (r), which is related to q_1 following eq.(4-1)¹⁸:

$$q_1 = (2d-2)^{0.5}/r \quad (4-1)$$

where d is the fractal dimension of the Porod region (interpretation of SAXS data presented in appendix), i.e. the absolute value of the slope when intensity is plotted in the logarithmic (base 10) domain as a function of q (Figure 4.4a). The fitted needle radius r from the in-situ SAXS measurement increases slightly as a function of hydration time, i.e. from ~20 nm at 20 min hydration to ~23 nm at 120 min hydration, with a standard error of ~0.7 nm (Figure 4.4b). A comparable result was obtained from the SAS data calculated from the ptychographic images at both $w/s = 1$ and 10, where the radii of ettringite crystallites are 20-25 nm, with uncertainty of 2-5 nm. Needles in confined space (C1-C2) are similarly thick to those growing in open space (O1-O6). Therefore in the time that concrete is required to be workable (i.e. < ~10 hours), the typical radius of ettringite precipitates is <30 nm, and is independent of the w/s and hydration time. The growth of ettringite crystals is mainly through new precipitates on C₃A surface, rather than the thickening or lengthening of individual ettringite needles.

4.4 3D morphology of C₃A hydrated in the presence of gypsum during the induction period

Only 2D morphologies of hydrated C₃A at nano- and meso-scale have been reported in the literature so far, which provides limited morphological information on the C₃A dissolution frontier. To further probe the 3D nanoscale morphology of partially reacted C₃A in induction period, a full-field TXM tomographic study was conducted (a movie of the volume rendering is presented in the appendix). C₃A particles are non-uniformly reacted at 143 minutes of hydration (Figure 4.5), with the solid hydration products at C₃A surfaces varying in thickness from almost not visible to ~1 μm. This information is not observed in the 2D X-ray ptychographic images (Figure 4.3). Heterogeneous C₃A dissolution is observed to generate features on the sub-micrometer scale, including highly reacted and rough surface regions (yellow arrows in Figure 4.5c-6d) and much smoother surfaces with no or low reaction extents (red arrows in Figure 4.5c-6d). Non-uniform hydration is also observed in the inner cavities of C₃A particles (Figure 4.5c-6d), some of which are more

connected to the external particle surface than others. The amount of reactive C_3A surface is directly related to the speed of ettringite formation¹⁶. Here, the TXM results show that the amount of reactive C_3A surface depends on: a) the nonuniform nature of C_3A hydration, with a significant proportion of its surface area reacting in very slow rate; and b) that the surfaces of inner cavities are reactive and that any originally closed cavities participate in hydration as soon as the dissolution frontier exposes them to the solution.

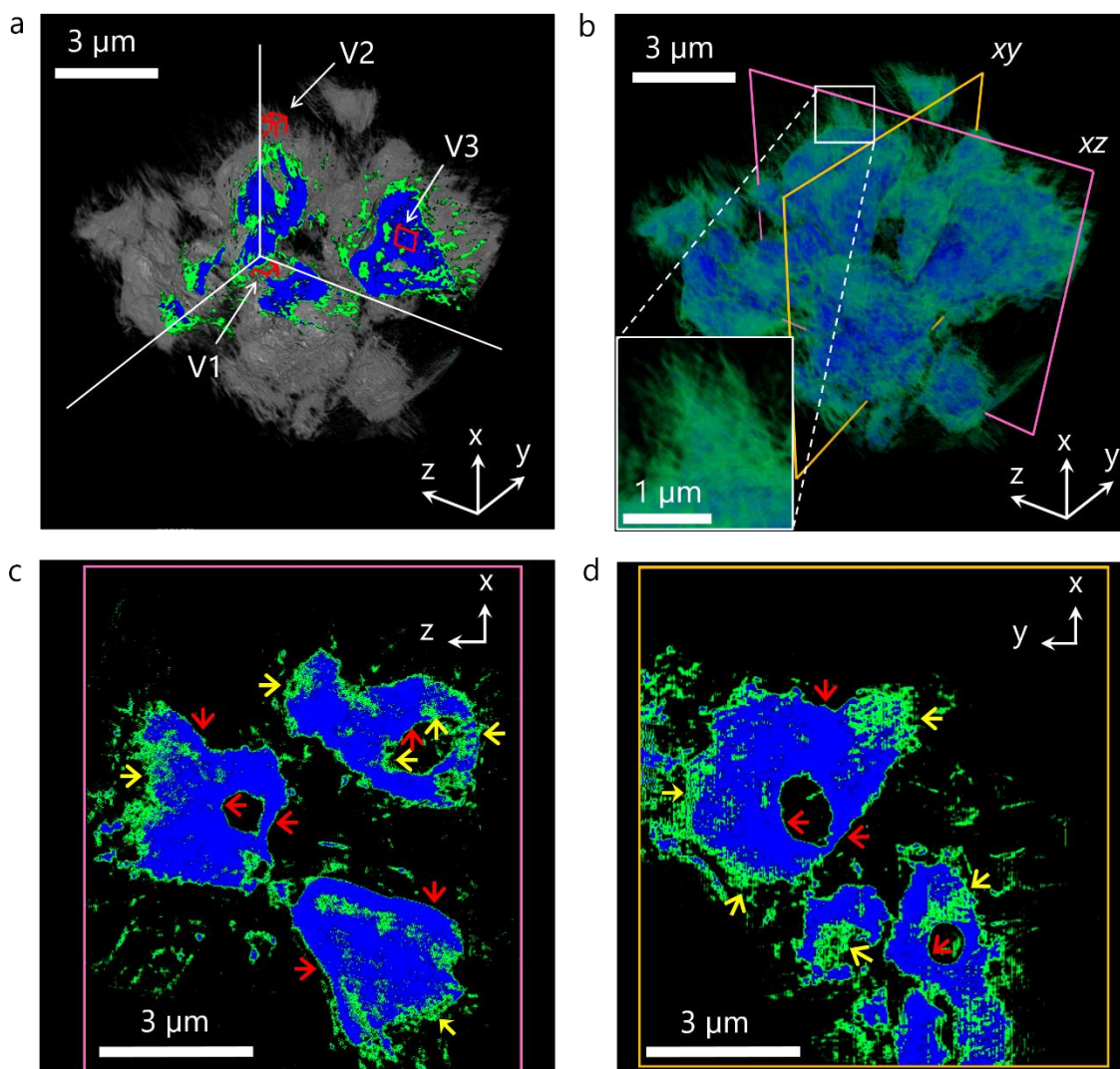


Figure 4.5 3D reconstruction of C_3A particles hydrated for 143 minutes in the presence of gypsum. **a**, A cubic sub-volume (white lines represent its edges) is removed from the full 3D dataset to expose interior features, which are colored blue (remnant C_3A) and green (solid hydration products). The reconstructed voxel volume is $10 \times 10 \times 10 \text{ nm}^3$. Sub-volumes V1, V2 and V3 (red cubes of 500 nm edge length) correspond to hydration products grown in confined space, open space, and remnant C_3A , respectively. **b**, Colored volume rendering of remnant C_3A (blue) and hydration product (green). A magnified

region is shown in the white box inset. Two slices, marked by pink and orange squares, are displayed in **c** (xz plane) and **d** (xy plane), respectively. Segmentation of hydration products and remnant C_3A is performed by applying a threshold optical density value according to the histogram of the full 3D data (details available in appendix).

Porosities of selected sub-volumes in Figure 4.5a, V1 (solid hydration products grown in confined space), V2 (solid hydration products grown in open space) and V3 (remnant C_3A), are determined according to the attenuation Law.¹⁹ In the appendix, it is shown that the porosity, φ , can be estimated using eq.(4-2):

$$\varphi = 1 - OD_{recon_mean} / OD_{recon_max} \quad (4-2)$$

where OD_{recon_mean} is the average reconstructed optical density of the studied sub-volumes, and OD_{recon_max} is the reconstructed optical density of a zero-porosity voxel of the studied phase (ettringite or C_3A), which is assumed to be the 90% threshold of the cumulative distribution of the optical density histograms in V2 and V3 (details available appendix). By applying this equation to the three sub-volume, the respective porosities of V1, V2 and V3 are determined to be ~29%, ~58% and ~19%. Therefore, after 143 min of hydration, the network of ettringite needles on open C_3A surfaces (V2) is highly porous; the network of ettringite needles in confined spaces (V1) is denser but also significantly porous. The region representing remnant C_3A (V3) contains non-zero porosity due to the presence of initial cavities and cracks. The mechanical property of the cementitious matrix is greatly determined by its porosity^{1,14}, and here the first sub-50 nm study of local porosities is present, which provides important experimental data that can be used to validate 3D computational models of cement hydration.

4.5 Discussion and conclusions

Our results provide strong evidence that OH-AFm or \bar{S} -AFm do not greatly retard the initial ettringite formation as there is a rapid ettringite formation after a few minutes of hydration when the C_3A surface is already efficiently covered by these phases. These AFm-type phases also do not form a C_3A dissolution-inhibiting ‘diffusion-barrier’ in the induction period, because ettringite is identified by coupled STXM and Al K -edge XANES as the only precipitate on C_3A particles after 150 minutes of hydration, which is during the induction period and a typical time point when PC concrete is workable. Therefore, the initially formed AFm phases destabilized completely to ettringite during the induction period. With imaging resolution ~17 nm, no continuous dissolution-inhibiting ‘diffusion-barrier’ is observed at the C_3A dissolution frontier for most of the induction period. Our X-ray ptychography and TXM results also show that the network of ettringite needles that forms on C_3A particles is highly porous, with porosities of 29% and 58% calculated for these networks when growing in confined and open spaces after 143 min of hydration, respectively. These porous ettringite networks would not act as diffusion barrier that retards C_3A hydration. Therefore, the results point towards an alternative mechanism of C_3A dissolution retardation, e.g. potentially by adsorption of Ca and/or S complexes^{20,21}. This

mechanism is consistent with our observation that the precipitation rate of ettringite quickly decreases right after the rapid initial ettringite formation that happens in the first ~2 min of hydration, as it may correspond to an initial formation of Ca and/or S surface complexes that are structurally similar to ettringite. Further investigation on C₃A surface at the first 1-2 min hydration in the presence of gypsum is promising to provide more evidence.

The morphology of the C₃A dissolution frontier in the presence of gypsum in aqueous solution is similar in systems with w/s = 1 and 10. In both cases, ettringite precipitates predominantly by more needles forming on C₃A surface, instead of increasing in thickness and length of individual needles: the ettringite needles with radii of ~20 nm are observed after 20 min of hydration and grow to ~25 nm thick by 15 hours hydration; and the length of individual ettringite needles are always ~1 μm. The independence of the needle length on the w/s suggests that the maximum needle length is determined by other factors, e.g. the local saturation extent. C₃A dissolution is observed to occur heterogeneously, with more ettringite forming on roughly-dissolved regions, consistent with the dissolution rate of C₃A controlled to some extent by its crystalline surface chemistry and morphology.²²

For the first time, this work provides a sub-50 nm 2D and 3D morphological and spectroscopic study of hydrated C₃A in the presence of gypsum during the induction period. It advances the understanding of the retardation mechanism of gypsum on C₃A hydration through the central finding that a ‘diffusion-barrier’ does not exist on C₃A particles throughout the induction period in C₃A-gypsum-H₂O systems. This work may inspire future research on tuning the surface reactivities and cavity contents of C₃A particles as innovative solutions to controlling the workability of cementitious composites. It also serves as a first step to studying cement hydration with sub-50 nm resolution synchrotron radiation technologies. In future studies, it is expected that these techniques will provide key experimental evidence to validate multi-scale computational simulations of PC hydration²³ and macro-properties at fresh state²⁴.

4.6 References

- 1 Black, L., *et al.* Hydration of tricalcium aluminate (C₃A) in the presence and absence of gypsum — studied by Raman spectroscopy and X-ray diffraction. *J. Mater. Chem.* **16**, 1263-1272 (2006).
- 2 Meredith, P., Donald, A. M., Meller, N. & Hall, C. Tricalcium aluminate hydration: Microstructural observations by in-situ electron microscopy. *J. Mater. Sci.* **39**, 997-1005 (2004).
- 3 Mondal, P. & Jeffery, J. W. The crystal structure of tricalcium aluminate, Ca₃Al₂O₆. *Acta Cryst. B* **31**, 689-697 (1975).
- 4 Moore, A. E., & Taylor, H. F. W. Crystal structure of ettringite. *Acta Cryst. B* **26**, 386-393 (1970).

- 5 Comodi, P., Nazzareni, S., Zanazzi, P.F. & Speziale, S. High-pressure behavior of gypsum: a single-crystal X-ray study. *Am. Mineral.* **93**, 1530-1537 (2008).
- 6 Jensen, T. R., Christensen, A. N. & Hanson, J. C. Hydrothermal transformation of the calcium aluminum oxide hydrates $\text{CaAl}_2\text{O}_4 \cdot 10\text{H}_2\text{O}$ and $\text{Ca}_2\text{Al}_2\text{O}_5 \cdot 8\text{H}_2\text{O}$ to $\text{Ca}_3\text{Al}_2(\text{OH})_{12}$ investigated by in situ synchrotron X-ray powder diffraction. *Cem. Concr. Res.* **35**, 2300-2309 (2005).
- 7 Allmann, R. Refinement of the hybrid layer structure $[\text{Ca}_2\text{Al}(\text{OH})_6]^- \cdot [1/2\text{SO}_4 \cdot 3\text{H}_2\text{O}]^+$. *Neues. Jb. Miner. Monat.* **3**, 136-144 (1977).
- 8 Lager, G. A., Armbruster, T. & Faber, J. Neutron and X-ray diffraction study of hydrogarnet $\text{Ca}_3\text{Al}_2(\text{O}_4\text{H}_4)_3$. *Am. Mineral.* **72**, 756-765 (1987).
- 9 Li, D., Bancroft, G. M., Fleet, M., Feng, X & Pan, Y. Al K-edge XANES spectra of aluminosilicate minerals. *Am. Mineral.* **80**, 432-440 (1995).
- 10 Neuville, D. R., Henderson, G. S., Cormier, L. & Massiot, D. The structure of crystals, glasses, and melts along the CaO-Al₂O₃ join: results from Raman, Al L- and K-edge X-ray absorption, and ²⁷Al NMR spectroscopy. *Am. Mineral.* **95**, 1580-1589 (2010).
- 11 Vespa, M., Wieland, E., Döhn, R., Grolimund, D. & Scheidegger, A.M. Determination of the elemental distribution and chemical speciation in highly heterogeneous cementitious materials using synchrotron-based micro-spectroscopic techniques. *Cem. Concr. Res.* **37**, 1473-1482 (2007).
- 12 Richard, N., Lequeux, N. & Boch, P. EXAFS study of refractory cement phases: $\text{CaAl}_2\text{O}_4 \cdot 10\text{H}_2\text{O}$, $\text{Ca}_2\text{Al}_2\text{O}_5 \cdot 8\text{H}_2\text{O}$, and $\text{Ca}_3\text{Al}_2(\text{OH})_{12}$. *J. Phys. III* **5**, 1849-1864 (1995).
- 13 Aruja, E. The unit cell and space group of $4\text{CaO} \cdot \text{Al}_2\text{O}_3 \cdot 19\text{H}_2\text{O}$ polymorphs. *Acta Cryst.* **14**, 1213-1216 (1961).
- 14 Barnes, P. & Bensted, J. *Structure and Performance of Cements* (CRC Press, Boca Raton, 2002).
- 15 Roberts, M. H. New calcium hydrates. *J. Appl. Chem.* **7**, 543-546 (1957).
- 16 Minard, H., Garrault, S., Regnaud, L. & Nonat, A. Mechanisms and parameters controlling the tricalcium aluminate reactivity in the presence of gypsum. *Cem. Concr. Res.* **37**, 1418-1426 (2007).
- 17 Tenoutasse, N. The hydration mechanism of C₃A and C₃S in the presence of calcium chloride and calcium sulfate. *Proceedings of the 5th International Symposium on the Chemistry of Cement* (1968).
- 18 Hammouda, B. A new Guinier-Porod model. *J. Appl. Cryst.* **43**, 716-719 (2010).
- 19 Hubbell, J. H. & Seltzer, S.M. Tables of X-ray mass attenuation coefficients 1 keV to 20 MeV for elements Z1 to 92 and 48 additional substances of dosimetric interest. *Gaithersburg, MD: National Institute of Standards and Technology* (1995).

- 20 Bullard, J. W., *et al.* Mechanisms of cement hydration. *Cem. Concr. Res.* **41**, 1208-1223 (2011).
- 21 Stumm, W. Reactivity at the mineral-water interface: dissolution and inhibition. *Colloids Surf. A* **120**, 43-166 (1997).
- 22 Lasaga, A. C. & Luttge, A. Variation of crystal dissolution rate based on a dissolution stepwave model. *Science* **291**, 2400-2404 (2001).
- 23 Bentz, D. P. Three-dimensional computer simulation of portland cement hydration and microstructure development. *J. Am. Ceram. Soc.* **80**, 3-21 (1997).
- 24 Ulm, F. J. & Coussy, O. Modeling of thermochemomechanical couplings of concrete at early ages. *J. Eng. Mech-ASCE.* **121**, 785-794 (1995).

5. Chemistry-structure-property correlation of C-S-H at atomistic scale

In the mature age, mechanical property and volumetric stability are the most important character of PC concrete, both of which depend greatly on the main binding phase, C-S-H. Atomistic simulations suggest its mechanical property is driven by crystallographic defects such as SiO_4 tetrahedra omission, yet there is no experimental validation directly on a porosity-free C-S-H solid. In this chapter, synchrotron-radiation-based high pressure X-ray diffraction is integrated with atomistic simulations, aiming at correlating the mechanical properties of nano-crystalline C-S-H to the systematically varying atomistic configuration caused by changing Ca-to-Si molar ratio (Ca/Si). From the diffraction data, the deformation of C-S-H nanocrystals along each crystal axis was analyzed, which further yields the bulk modulus of C-S-H. The atomistic simulation not only reproduced the deformation of C-S-H under hydrostatic pressure, but also revealed the atomistic scale mechanism of the deformation. It is demonstrated that validating the interlayer spacing of C-S-H is critical to build more realistic C-S-H models.

5.1 Ambient pressure XRD

The nano-crystalline C-S-H studied are randomly oriented, therefore continuous diffraction rings are observed on the raw diffraction image, as shown by the p1-p5 rings in Figure 5.1a (numbering of the diffraction rings are consistent with Figure 5.1c). Ruby (Cr-doped Al_2O_3 , pressure calibrant) is identified by its relatively intensive and discrete diffraction spots, which are apparent in most of the data collected (Figure 5.1c, blue arrows). The diffraction ring at $d \sim 2.0 \text{ \AA}$ is assigned to the oxides of the stainless steel gaskets (Figure 5.1c, green arrows). The raw 2D diffraction patterns are integrated along the radial direction to yield intensity vs. 2θ diffractograms (Figure 5.1c). All integrated diffraction patterns resemble XRD of C-S-H after masking the diffraction peaks of ruby and gasket¹. The observed peaks assigned to C-S-H in the diffractograms correspond to $hk0$ reflections of tobermorite¹. This assignment is made considering the similar structure but much lower crystallinity in C-S-H, particularly along the c -direction²⁻⁵. The diffractions at the lowest probed pressure for each sample are considered the ambient condition references, which are 0.14 GPa for 0.8CSH and atmospheric pressure for 1.0CSH and 1.3CSH.

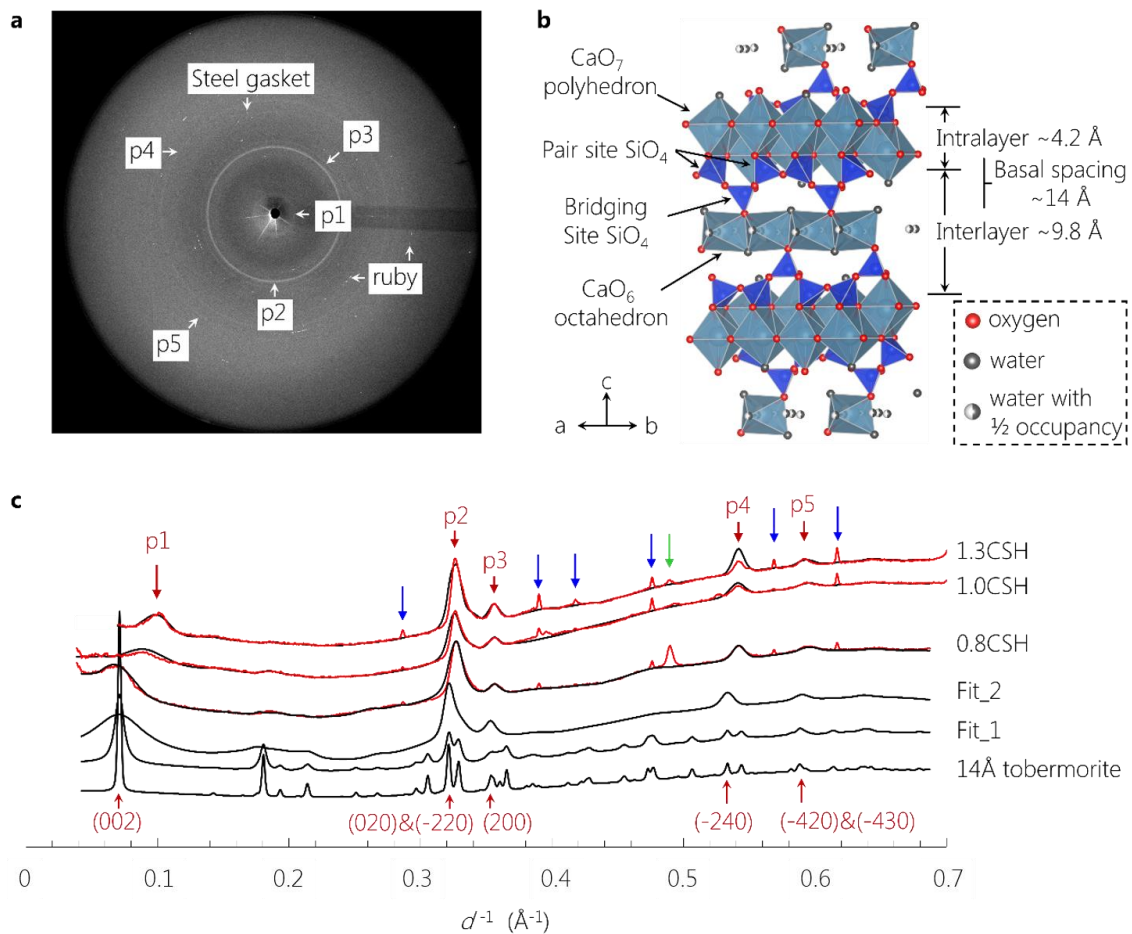


Figure 5.1 Rietveld refinement scheme. **a**, Raw diffraction pattern of 0.8CSH at ambient condition with the main diffraction features of C-S-H (p1-p5), steel gasket and ruby indicated. **b**, Crystal structure of 14 Å tobermorite (space group b11b) viewed along the (110) direction. The 14 Å-wide basal spacing comprises intralayer (~4.2 Å) and interlayer (~9.8 Å) spacing, separated by the pair sites Si. **c**, Red diffractograms are 0.8C-S-H, 1.0CSH and 1.3CSH at ambient condition. Peaks for C-S-H are labeled in red arrows. Peaks for ruby and steel gasket are marked with blue and green arrows, respectively. Refined diffractions are plotted in black at the same baseline as the measured results, starting from 14 Å tobermorite structure, followed by considering nano-crystalline effect (Fit_1), anisotropic strain-broadening (Fit_2), and final adjustment of lattice parameters a , b , c , and γ . The Miller indices of observable diffraction of C-S-H are labeled underneath the 14 Å tobermorite diffraction.

The tobermorite mineral family is composed of infinitely long ‘dreierketten’-type silicate chains bonded onto either side of CaO_7 double sheets (Figure 5.1b). These calcium silicate layers are separated by an aqueous electrolyte containing ‘interlayer’ space. The combined thicknesses of a calcium silicate layer and its associated interlayer region is defined as the basal spacing, which is typically observed as 9.3, 11.3, and 14.0 Å in tobermorite

minerals.⁶⁻¹⁰ At Ca/Si < 1.5, the structure of C-S-H is nanocrystalline and analogous to that of tobermorite, and most of C-S-H diffraction peaks can be assigned to the $hk0$ diffraction peaks of tobermorite.^{11,4} When compared with 14 Å tobermorite (*B11b*), peak p1, p3 and p4 matches the diffraction peaks of (002), (200) and ($\bar{2}40$). Due to the nanocrystallinity, peak p2 contains contributions from (020) and ($\bar{2}20$); peak p5 is composed of ($\bar{4}20$) and ($\bar{4}30$).

Here, the diffractogram is fitted, starting from 14 Å tobermorite structure in space group *B11b* (Figure 5.1b), in three steps: a) setting the crystallite size to ~15 nm isotropic particles⁴, which broadens the diffraction peaks and/or merges adjacent peaks together (Figure 5.1c, Fit_1). b) Reducing the crystallite size in the c -axis from 15 nm to ~2.5 nm and introducing anisotropic strain-broadening effect to c -direction, which significantly broadens peak p1 and generally smears out the other c axis-related peaks (Fit_2)¹². This residue strain, especially along c -axis, is universally observed and explained by the disordered stacking of the layer structure^{2,5}. c) Refining the lattice parameters a , b , c and γ . Refinement of the lattice parameter c relies on peak p1 (002), while the positions of the other labeled peaks p2-p5 depend greatly on the lattice parameters a and b . Details are available in supplementary information (appendix).

Here, the plate-like shape⁴ of C-S-H is verified by refining crystallite size to ~15-20 nm along a - and b -axis and ~2.5-5 nm along c -axis. Samples with different Ca/Si share similar parameters a and b at ambient pressure but distinct c , which decreases as Ca/Si increases, implying a decreasing basal spacing, which comprises intralayer and interlayer (Figure 5.1b). The intralayer spacing is less likely to change since all the samples reveal similar tobermorite-type layer backbone. Thus the decreasing of interlayer width accounts for majority of the basal spacing decreasing with increasing Ca/Si.

5.2 High pressure XRD

As shown in Figure 5.2a-2c, all diffraction peaks of nano-crystalline C-S-H shift to smaller d -spacing under increasing hydrostatic pressure, and return to their original positions upon unloading to ambient pressure, indicating reversible compression along three directions. The continuous trends in peak shift, and the absence of peak splitting or generation imply no reconstructive change of the crystal structure, while a pressure-induced strain broadening is observed.^{11,13} The broadening becomes so significant that p1 is not well resolved above 7.10 and 8.06 GPa for 0.8CSH and 1.0CSH respectively. This limits the refining of parameter c at higher pressures, although the parameters a and b can be confidently refined at all of the pressure values reached. Following the protocol in Figure 5.1c, refinement of the C-S-H lattice parameters at each pressure yields the results shown in Figure 5.2d-2e. Variation in the lattice parameter γ of $\pm 0.1^\circ$ has been reported for 14 Å tobermorite up to ~5 GPa,¹¹ inducing a volumetric strain of $\leq \pm 0.001$ that is negligible in determining the bulk modulus; therefore, the lattice parameter γ was refined at ambient pressure to be 122.6° , 122.8° and 122.5° for 0.8CSH, 1.0CSH and 1.3CSH, respectively, and set constant for refinement at all pressures.

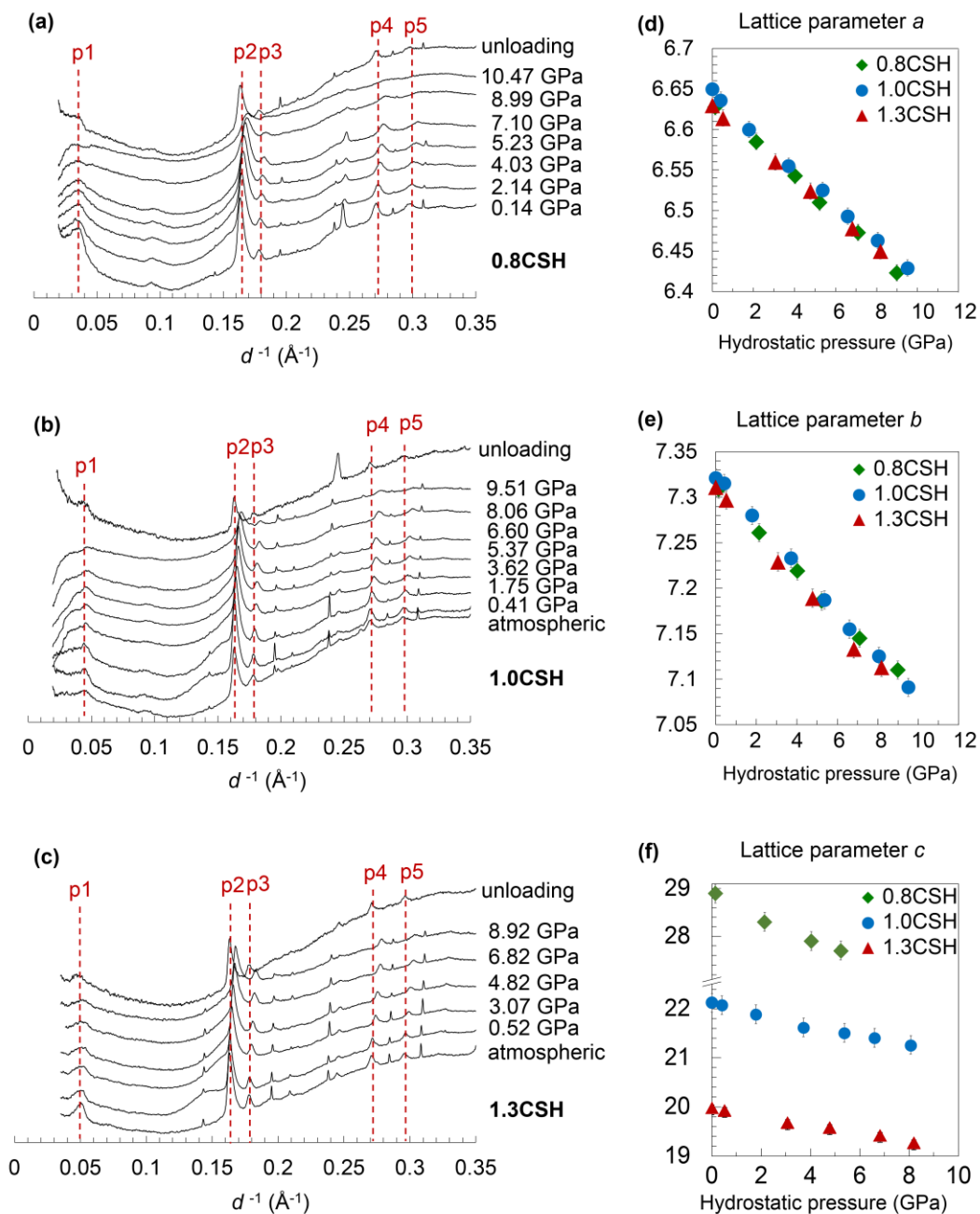
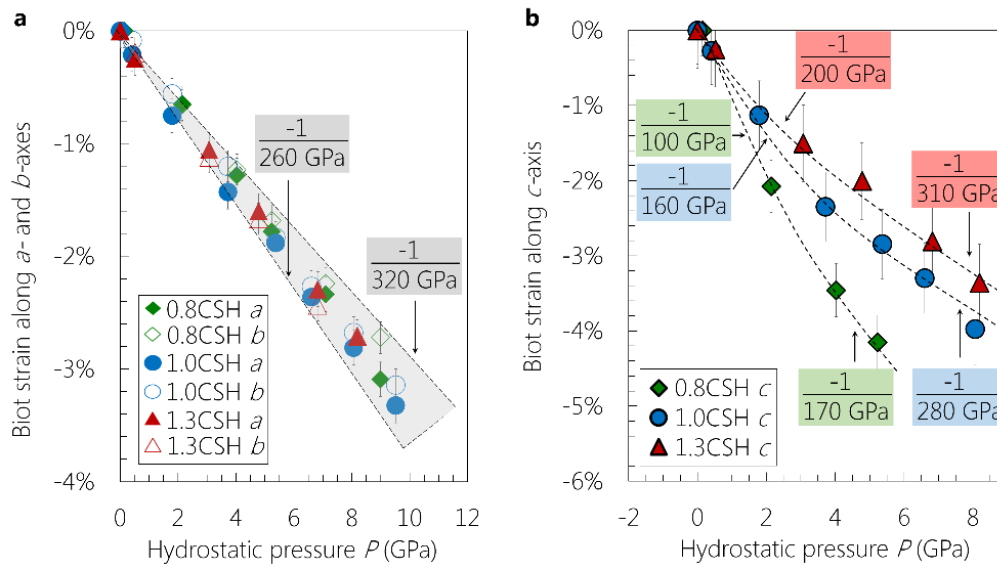


Figure 5.2 X-ray diffraction and lattice parameters as a functions of the applied hydrostatic pressure: Diffractograms of **a**, 0.8CSH, **b**, 1.0CSH, and **c**, 1.3CSH; pressure-induced change of lattice parameters **d**, *a*, **e**, *b* and **f**, *c*. The error bar is determined as 0.01, 0.01 and 0.1 \AA for *a*-, *b*- and *c*-axis, respectively (SI). The error of pressure is around 0.2 GPa.

All lattice parameters of C-S-H decrease monotonically with increasing hydrostatic pressure (Figure 5.2d-f), where a and b are highly consistent among all samples, nearly independent of their Ca/Si. Slightly reduced b are determined for 1.3CSH over the full range of applied pressure relative to the other Ca/Si compositions (Figure 5.2b), attributed to the omission of bridging site SiO_4 tetrahedron.³ A shortening of ~ 0.2 Å is observed for a and b at ~ 9 GPa, whereas more negative slopes are determined for c -axis, i.e. a shortening of 1.2 Å at 5 GPa for 0.8C-S-H, 0.9 Å and 0.7 Å at 9 GPa for 1.0C-S-H and 1.3C-S-H, respectively.

To estimate the mechanical property, lattice deformations are displayed as Biot strain ($(l-l_0)/l_0$, with l and l_0 are the measured and ambient condition lattice parameters, respectively) as functions of hydrostatic pressure (Figure 5.3a-b). Despite the significantly different amount of bridging site omissions, the hydrostatic incompressibilities of the a - and b -axes of 0.8CSH, 1.0CSH and 1.3CSH fall in the same range ($-1/260$ GPa to $-1/320$ GPa), and seems independent of Ca/Si (grey area in Figure 5.3a). The c -axis is softer than both a - and b -axes at ambient pressure, and is softer at lower Ca/Si. A non-linear deformation is observed for c -axis, as its elasticity increases by 50-70% at the maximum pressure probed for each samples, with respect to the ambient condition (Figure 5.3b). With hydrostatic pressure above ~ 4 GPa, c -axes of 1.0CSH and 1.3CSH have incompressibilities of ($-1/280$ GPa and $-1/310$ GPa, respectively) comparable to a - and b -axes, whereas the c -axis of 0.8CSH remains significantly softer than its orthonormal directions even at ~ 5 GPa.



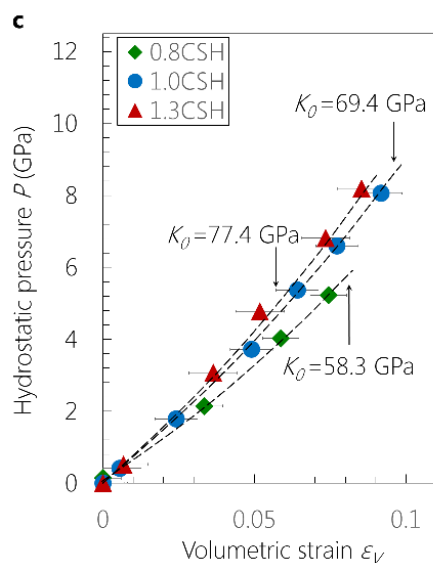


Figure 5.3 Measured mechanical response of C-S-H to hydrostatic pressure: Biot strain along **a**, *a*- and *b*-axes, and **b**, *c*-axis are plotted as functions of pressure. The slopes (dashed lines and curves) indicate incompressibilities, i.e. the negative inverse of elasticities. **c**, The 2nd order fitting of BM-EoS yields the ambient bulk modulus K_0 , with average R-square ~ 0.999 and standard error ~ 1 GPa. All error bars are from the refinement error in Figure 5.2.

The bulk modulus can be evaluated by fitting the Birch Murnaghan equation of state (BM-EoS). The determined initial bulk modulus (K_0) of 0.8C-S-H, 1.0C-S-H and 1.3C-S-H are 58.3, 69.7 and 77.2 GPa, respectively, with fitting error ~ 1 GPa (Figure 5.3c). The bulk moduli measured here are much higher than the directly measured values obtained by nano-indentation, i.e. 10-15 GPa for C-S-H(I) and *LD* C-S-H, and 20-25 GPa for *HD* C-S-H¹⁴⁻²⁰, and are also higher than the derived value after considering the packing density by the Mori-Tanaka model (~ 25 GPa) and the self-consistent model (~ 40 GPa)¹⁸, by applying a generally accepted Poisson's ratio (ν) of ~ 0.25 ²⁰.

5.3 Atomistic simulations

Atomistic simulations allow tracking atomic positions with increasing pressure, providing detailed configurational information to complement HP-XRD experiment. Here, we start the simulation from a typical layer-stacking structure modified from tobermorite²⁰, which is modified to match the existing crystal-chemical information as shown in Table 5.1. The amount of Si omission and interlayer Ca are straightforward determined to match the NMR data and measured Ca/Si. The amount of interlayer water is then adjusted such that the relaxed structure reproduces the measured basal spacing at ambient pressure, which has not raised enough attention in previous simulation studies.^{19,22-24} Note that the simulation model of 1.3CSH was generated from 9Å tobermorite, which has a space group of *C-1*. To enable direct comparison with the 14Å tobermorite (*B11b*) which is used in the refinement

of experimental data and simulation models for 0.8CSH and 1.3CSH, a virtual unit cell is defined in the 1.3CSH structure, whose *b*-axis runs parallel to the silicate chain, *a*-axis is 122.5° with-respect-to the *b*-axis, and *c*-axis is perpendicular to the *ab*-plan. The lattice parameter *b* of the virtual unit cell in 1.3CSH equals the modeled result, while *a* is determined so that the *ab*-plan projection of the virtual unit cell has the same size as the modeled result, and the parameter *c* is determined so that the virtual unit cell has the same volume as the modeled results.

Table 5.1 Comparing the chemical information and lattice parameters between the experimental values and the simulations models, at ambient pressure.

	0.8CSH		1.0CSH		1.3CSH	
	experiment	model	experiment	model	experiment	model*
<i>a</i> (Å)	6.63±0.01	6.73	6.65±0.01	6.72	6.63±0.01	6.62
<i>b</i> (Å)	7.31±0.01	7.49	7.32±0.01	7.41	7.31±0.01	7.34
<i>c</i> (Å)	28.9±0.1	28.4	22.1±0.1	22.6	19.9±0.1	19.4
<i>α</i>	90°	90.2°	90°	91.6°	90°	90°
<i>β</i>	90°	87.3°	90°	86.5°	90°	90°
<i>γ</i>	122.6°±0.5	124.3°	122.8°±0.1°	125.1°	122.5°±0.1°	122.5°
Ca/Si	0.8	0.80	1.0	1.00	1.3	1.25

* The lattice parameters of 1.3CSH model are calculated based on the virtual unit cell, as described in the text, in order to be directly compared with other data sets.

The present models readily predict the softness and non-linearity along the *c*-axis, relative to the in-planar (*a*- and *b*-axes) deformation (Figure 5.4a-b). Despite the Ca/Si, the calculated Biot strains of the *a*- and *b*-axes are slightly smaller (-1.9% to -2.4% at 8 GPa) than the measured values (~-2.6% at 8 GPa), whereas the *c*-axis strains are consistent between simulation and experiment. The simulation also reveals smaller *c*-axis deformation as Ca/Si increases, and strain hardening along *c*-axis with increasing pressure as well. The ambient pressure bulk moduli are calculated as 59.3, 72.3 and 83.4 GPa for 0.8CSH, 1.0CSH and 1.3CSH respectively, which matches the experimental results.

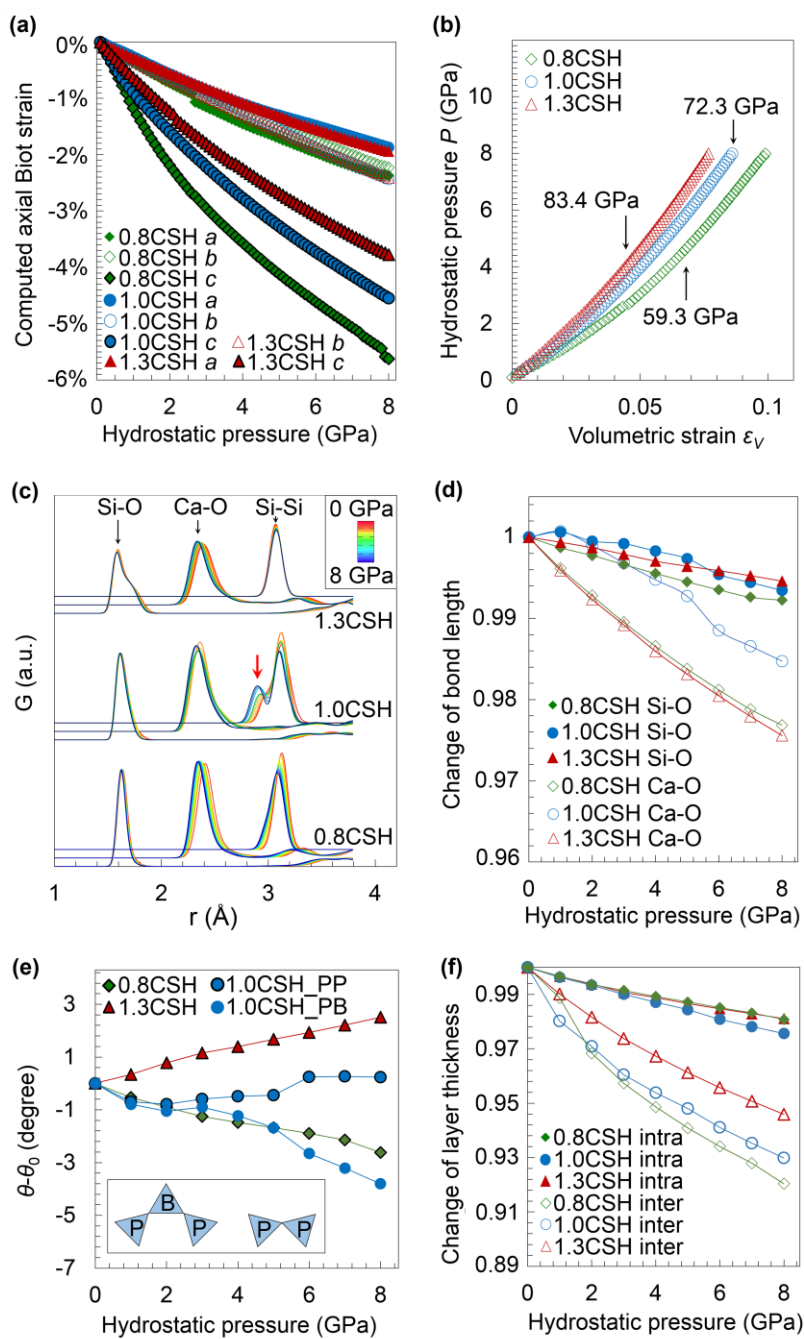


Figure 5.4 Atomistic simulation under hydrostatic pressure up to 8 GPa. **a**, Biot strain of *a*-, *b*- and *c*-axes. The 1.3CSH model is from 9 Å tobermorite and has different shape with the other two models. Its strain data were recast by defining *b*-axis as the Si chain direction, *a*-axis to be in-planar by 122.5° relative to *b*-axis, and *c*-axis to be perpendicular to the *ab* plane. **b**, Volumetric strain is plotted as a function pressure; results of second order BM-EoS fitting is displayed. **c**, Pair distribution functions (PDF)

of Si-O, Ca-O and Si-Si pairs. Baselines are adjusted for viewing convenience. Red arrow indicates the first Si-Si peak splitting. **d**, Average Ca-O, Si-O bond deformation. **e**, Si-O-Si dihedral angle change. The inset in **e** sketches non-defected Si chain (left) and dimeric structure after bridging Si omission (right). **f**, The interlayer and intralayer spacings are plotted as functions of applied hydrostatic pressure.

The rotation of corner-shared SiO_4 tetrahedron is a commonly observed deformation mechanism for Si-bearing minerals at relatively low pressure, rather than directly deform the stiff Si-O bond.²¹ This may explain why, in 1.0CSH and 1.3CSH with bridging site Si omission, the *b*-axis stiffness is not reduced due to the fragmented Si chain. To verify this phenomenon in C-S-H, the bond strain of Si-O and Ca-O (Figure 5.4d), and Si-O-Si dihedral angle change (Figure 5.4e) are quantified, using the calculated PDF (Figure 5.4c). Despite the Ca/Si, the slightly left-drifted Si-O PDF peaks near $\sim 1.62 \text{ \AA}$ correspond to a small bond shortening of 0.4-0.6% at 8 GPa. The Ca-O bond shortens much more (2.4% for 0.8CSH and 1.3CSH, 1.2% for 1.0CSH) as verified by the significant PDF peaks drifting. The Si linkage in 0.8CSH is continuous, and in 1.3CSH merely dimeric. In both cases, a single Si-Si first PDF peak is observed as pressure increases. At 8GPa the Si-O-Si angle decreases by $\sim 3.8^\circ$ in 0.8CSH but increase by $\sim 1.6^\circ$ in 1.3CSH, causing the closest Si-Si distance to decrease by 0.048 \AA and increase by 0.006 \AA , respectively. In 1.0CSH the two Si linkage configurations, resulted from partial bridging Si omission (Figure 5.4e inset), exhibit distinct angle evolution. The dimeric structure (1.0CSH_PP) remains almost untilted, whereas the angle between pair site Si and bridging site Si decreases by $\sim 3^\circ$ at 8GPa. it is therefore confirmed that the SiO_4 dimers do not contribute to the compression along *b*-axis, and the continuous dreierketten chain deforms by the tilting of adjacent tetrahedra, rather than the Si-O bond shortening.

Both experiment and simulation reveal the most distinct mechanical response of the three samples to be along *c*-axis. The change of the interlayer and intralayer spacing, as separated by the average *c*-coordinates of the pair Si atoms (Figure 5.4b), are plotted as functions of hydrostatic pressure (Figure 5.4f). The interlayer deforms much more than the intralayer in 0.8CSH and 1.0CSH, and dominates their overall deformation along the *c*-axis. With the Si tetrahedron chain completely broken into dimers, i.e. in 1.3CSH, the much thinner and more Ca-enriched interlayer clearly becomes stiffer, but is still much softer than its intralayer. Therefore, the overall modulus of CSH is dominated by the shortening and densification of the interlayer spacing, which is promoted by increasing Ca/Si. The crystallographic defects (e.g. bridging site Si omission) seem less important in determining the incompressibility along each lattice direction. The complete elasticity tensors of all three C-S-H models are listed in Table 5.2.

Table 5.2 The 6×6 elasticity tensors of three C-S-H models, GPa.

0.8 CSH					
108.2182	48.0028	26.3614	-0.4302	1.5082	-2.87

48.0028	108.0798	27.1299	-1.1461	2.9915	-6.8919
26.3614	27.1299	60.4687	-0.6461	2.357	-2.2492
-0.4302	-1.1461	-0.6461	20.9796	-3.5757	2.0703
1.5082	2.9915	2.357	-3.5757	19.8432	-0.7182
-2.87	-6.8919	-2.2492	2.0703	-0.7182	40.1193
1.0CSH					
126.832	51.9468	39.5936	-0.1747	6.1555	0.9934
51.9468	125.1373	41.8073	7.0011	3.5576	-5.146
39.5936	41.8073	100.6737	5.4425	1.7579	-0.0232
-0.1747	7.0011	5.4425	31.8621	0.8641	0.8952
6.1555	3.5576	1.7579	0.8641	20.2731	-1.3745
0.9934	-5.146	-0.0232	0.8952	-1.3745	45.9465
1.3CSH					
133.9717	52.5193	33.4183	-1.4589	1.5006	-1.547
52.5193	141.9933	36.6975	-0.862	-1.0003	3.2281
33.4183	36.6975	72.5062	-3.8661	4.6653	-0.2121
-1.4589	-0.862	-3.8661	16.0152	-1.1033	-1.297
1.5006	-1.0003	4.6653	-1.1033	19.258	-1.1571
-1.547	3.2281	-0.2121	-1.297	-1.1571	43.7139

5.4 Discussions and conclusions

The present work experimentally probes the nonlinear anisotropic mechanical behavior of C-S-H, and clearly describes how the configurational change, as induced by increasing Ca/Si, alters its response along different lattice directions. In the reported simulations of C-S-H from defected tobermorite model, increasing Ca/Si ratio of C-S-H causes bridging Si omission and poor crystallinity, and has been shown to decrease the overall mechanical behavior (Figure 5.5a).^{19,22,23} However, it is shown here that with increasing Ca/Si the overall stiffness doesn't necessarily decrease as the interlayer becomes thinner and denser with increasing amount of Ca ions intercalated in the interlayer opening. Our experiment and simulation both indicate that C-S-H stiffens with increasing Ca/Si, as the densified basal spacing is more dominant in resisting the *c*-axis deformation and hence increases the overall stiffness.

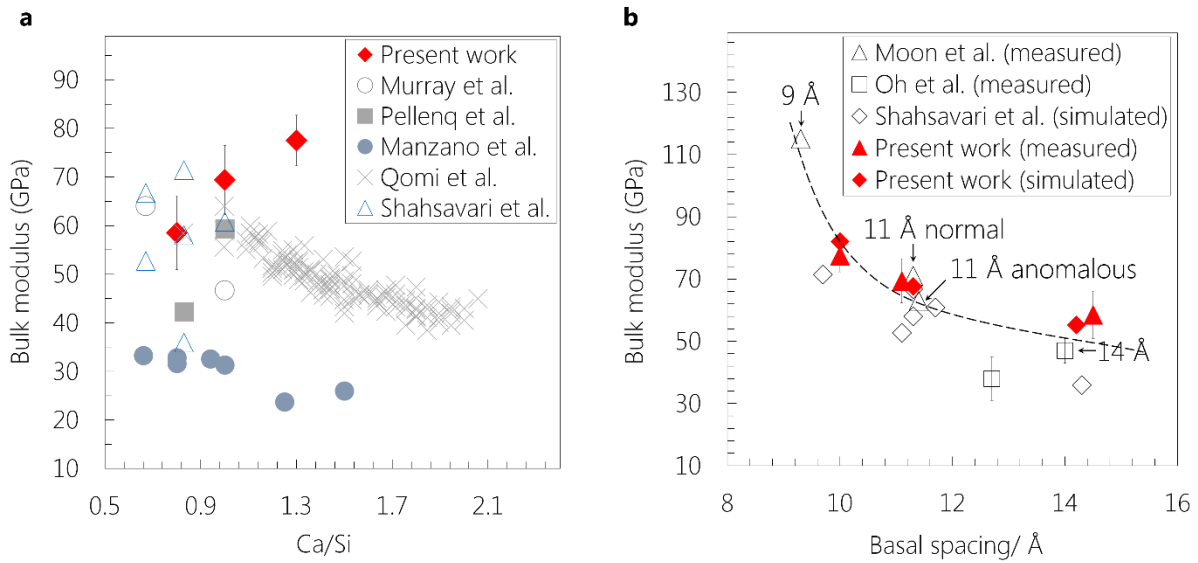


Figure 5.5 Bulk modulus of C-S-H as a function of **a**, $\text{Ca/Si}^{20-23,24}$ and **b**, basal spacing²⁴⁻²⁶. **a**, For some reported data, elastic moduli are recast to bulk modulus by assuming isotropy and $\nu \sim 0.25$ ¹⁹. **b**, The measured data points of crystalline tobermorite are labeled with arrows^{11,26}. Dashed curve is to eye-guide the trend.

The atomistic simulation with 11 Å tobermorite of Hamid model⁷ does yield an increasing modulus with increasing Ca in the interlayer space²⁴, however the moduli of different crystalline phases seem to be independent of Ca/Si. By plotting the measured bulk moduli as a function of basal spacing (Figure 5.5b), a decreasing trend is readily seen and is applicable to experimental and simulation results of crystalline tobermorite minerals^{24,11,26} and poorly crystalline C-S-H²⁵, although the calculated results are systematically smaller. As reported by high pressure XRD studies of minerals with structural SiO_4 tetrahedra, the compression takes place mainly through volumetric strain of cation-oxygens polyhedra (e.g., CaO_8 octahedron in grossular²⁷) compensated by the tilting of SiO_4 tetrahedra, and the overall modulus depends mostly on the compressibility of cation-oxygens polyhedra.^{27,28} This again confirms that the mechanical property of C-S-H is dominated by the densification of the interlayer spacing, instead of by dreierketten chain defects. This conclusion adds important enlightenment to the fundamental knowledge of the composition-structure-property correlation of C-S-H, and is expected to broadly impact from-bottom-up simulation approaches to the structural and property of C-S-H-based binding material.

In nowadays civil engineering practice, (Al-rich) SCMs are often used in replacement of PC, and are known to reduce the Ca/Si ratio of C-S-H. This may leads to the change of interlayer, as shown by the results in this chapter, which leads to the change of mechanical property at the nanometer level through modifying the interlayer spacing. For example, the nanoscale globules of C-S-H is expected to be less stiff in SCMs-incorporated concrete,

than PC concrete. At the meantime, Al-incorporation into the crystal structure may also alter the mechanical property of C-S-H, which will be discussed in the next chapter.

5.5 References

1. Taylor, H. F. W. *Cement chemistry, second ed.*. Thomas Telford, London (1997).
2. Renaudin, G., Russias, J., Leroux, F., Frizon, F. & Cau-dit-Coumes, C. Structural characterization of C-S-H and C-A-S-H samples—part I: long-range order investigated by Rietveld analyses. *J. Solid State Chem.* **182**, 3312-3319 (2009).
3. Richardson, I. G. Model structures for C-(A)-S-H (I). *Acta Crystallogr. Sect. B-Struct. Sci.* **70** (2014).
4. Battocchio, F., Monteiro, P. J. & Wenk, H. R. Rietveld refinement of the structures of 1.0 CSH and 1.5 CSH. *Cem. Concr. Res.* **42**, 1534-1548 (2012).
5. Grangeon, S., Claret, F., Linard, Y. & Chiaberge, C. X-ray diffraction: a powerful tool to probe and understand the structure of nanocrystalline calcium silicate hydrates. *Acta Crystallogr. Sect. B-Struct. Sci.* **69**, 465-473 (2013).
6. Merlino, S., Bonaccorsi, E. & Armbruster, T. The real structures of clinotobermorite and tobermorite 9 Å OD character, polytypes, and structural relationships. *Eur. J. Mineral.* **12**, 411-429 (2000).
7. Hamid, S. A. The crystal structure of the 11 Å natural tobermorite $\text{Ca}_{2.25}[\text{Si}_3\text{O}_{7.5}(\text{OH})_{1.5}] \cdot \text{H}_2\text{O}$. *Z. Kristallogr. Cryst. Mater.* **154**, 189-198 (1981).
8. Merlino, S., Bonaccorsi, E. & Armbruster, T. Tobermorites: their real structure and order-disorder (OD) character. *Am. Mineral.* **84**, 1613-1621 (1999).
9. Merlino, S., Bonaccorsi, E. & Armbruster, T. The real structure of tobermorite 11 Å normal and anomalous forms, OD character and polytypic modifications. *Eur. J. Mineral.* **13**, 577-590 (2001).
10. Bonaccorsi, E., Merlino, S. & Kampf, A. R. The crystal structure of tobermorite 14 Å (Plombierite), a C-S-H phase. *J. Am. Ceram. Soc.* **88**, 505-512 (2005).
11. Oh, J. E., Clark, S. M., Wenk, H. R. & Monteiro, P. J. Experimental determination of bulk modulus of 14 Å tobermorite using high pressure synchrotron X-ray diffraction. *Cem. Concr. Res.* **42**, 397-403 (2012).
12. Popa, N. C. & Balzar, D. Size-broadening anisotropy in whole powder pattern fitting. Application to zinc oxide and interpretation of the apparent crystallites in terms of physical models. *J Appl. Cryst.* **41**, 615-627 (2008).
13. Buerger, M. J. Polymorphism and phase transformations. *Fortschr. Mineral.* **39**, (1961).

14. Constantinides, G. & Ulm, F. J. The effect of two types of CSH on the elasticity of cement-based materials: Results from nanoindentation and micromechanical modeling. *Cem. Concr Res.* **34**, 67-80 (2004).
15. J. Krakowiak, K., Wilson, W., James, S., Musso, S. & Ulm, F.-J. Inference of the phase-to-mechanical property link via coupled X-ray spectrometry and indentation analysis: Application to cement-based materials. *Cem. Concr. Res.* **67**, 271–285 (2015).
16. Pelisser, F., Gleize, P. J. P. & Mikowski, A. Effect of the Ca/Si Molar Ratio on the Micro/nanomechanical Properties of Synthetic CSH Measured by Nanoindentation. *J. Phys. Chem. C.* **116**, 17219-17227 (2012).
17. Jennings, H. M., Thomas, J. J., Gevrenov, J.S., Constantinides, G. & Ulm, F. J. A multi-technique investigation of the nanoporosity of cement paste. *Cem. Concr. Res.* **37**, 329-336 (2007).
18. Constantinides, G. & Ulm, F. J. The nanogranular nature of C–S–H. *J. Mech. Phys. Solids.* **55**, 64-90 (2007).
19. Qomi, M. A., *et al.* Combinatorial molecular optimization of cement hydrates. *Nat. Commun.* **5**, (2014).
20. Pellenq, R. J. M., Lequeux, N. & Van Damme, H. Engineering the bonding scheme in C–S–H: The iono-covalent framework. *Cem. Concr. Res.* **38**, 159-174 (2008).
21. Gatta, G. Does porous mean soft? On the elastic behaviour and structural evolution of zeolites under pressure. *Z. Kristallogr.* **223**, 160-170 (2008).
22. Manzano, H., Dolado, J. S. & Ayuela, A. Elastic properties of the main species present in Portland cement pastes. *Acta Mater.* **57**, 1666-1674 (2009).
23. Murray, S., Subramani, V., Selvam, R. & Hall, K. Molecular dynamics to understand the mechanical behavior of cement paste. *Transport. Res. Rec.: J. Transport. Res Board.* **2142**, 75-82 (2010).
24. Shahsavari, R., Buehler, M. J., Pellenq, R. J. M. & Ulm, F. J. First-principles study of elastic constants and interlayer interactions of complex hydrated oxides: Case study of tobermorite and jennite. *J. Am. Ceram. Soc.* **92**, 2323-2330 (2009).
25. Oh, J. E., Clark, S. M. & Monteiro, P. J. Does the Al substitution in C–S–H (I) change its mechanical property? *Cem. Concr. Res.* **41**, 102-106 (2011).
26. Moon, J. *Experimental and Theoretical Studies on Mechanical Properties of Complex Oxides in Concrete*. PhD dissertation, University Of California, Berkeley, Department of Civil and Environmental Engineering, (2013).
27. Hazen, R. M. & Finger, L. W. Crystal structures and compressibilities of pyrope and grossular to 60 kbar. *Am. Mineral.* **63**, 297-303 (1978).
28. Prewitt, C. T. & Downs, R. T. High-pressure crystal chemistry. *Rev. Mineral.* **37**, 284-318 (1998).

6. Influence of Aluminum incorporation to the mechanical property to C-A-S-H

Incorporating Al-rich SCMs is an important way to enhance the durability and reduce the carbon footprint of PC concrete. The incorporation of Al and increased curing temperature promotes the crystallization and cross-linking of calcium (alumino)silicate hydrate (C-(A-)S-H), yet the influence of Al-induced structural changes on the mechanical properties at atomistic scale is not well understood. In the previous chapter, the ability of HP-XRD in studying the structure-property correlation of C-S-H is demonstrated. Herein, HP-XRD is used to quantify the mechanical property of C-(A-)S-H nanocrystals with increasing Al incorporation contents (Al/Si=0, 0.05, 0.1). The influence of Al-induced dreierketten chain cross-linking on the anisotropic mechanical behavior of C-(A-)S-H is then discussed.

6.1 XRD and ptychography at ambient pressure

C-(A)S-H samples studied here are of the same Ca to Si molar ratio (Ca/Si) = 1.0 but with different Al to Si molar ratios (Al/Si) = 0.0, 0.05, 0.1, and are labeled Al0, Al05 and Al10, respectively. The XRD diffractograms obtained at the lowest probed pressure, (0.41, 0.27, and 0.0 GPa for Al0, Al05, and Al10, respectively), are used as ambient condition references (Figure 6.1a). The diffraction peaks, although clearly sharper here, generally match those present in typical laboratory XRD patterns of C-S-H(I): peaks with $1/d > 0.3 \text{ \AA}^{-1}$ are assigned to $(hk0)$ reflections¹⁻³. Here, diffraction patterns are refined starting from 11 Å tobermorite (monoclinic, space group $b11m$)⁴ by sequentially modifying the three most significant structural characteristics: (1) the anisotropic nano-crystallite sizes; (2) the micro-strain along c -axis due to disordered stacking; and (3) adjusting the lattice parameters a , b , c , and angle γ . The anisotropic crystallite sizes are estimated from the line broadening model “anisotropic – no rules” as described in the literature⁵. These crystallographic features are readily defined in the *MAUD* software package⁶.

As shown in Figure 6.1a, a peak near $1/d \sim 0.07\text{-}0.09 \text{ \AA}^{-1}$ is observed for all samples and is assigned to (002) reflections. In Al0, a much sharper second basal peak is observed at $\sim 0.07 \text{ \AA}^{-1}$ — other than the major basal peak observed at $\sim 0.08 \text{ \AA}^{-1}$ — indicating two major nano-crystalline structures in this sample that share similar structures in ab -plane but have different basal spacings; they are named Al0_C2 and Al0_C1, respectively hereafter. Refinement of the Al0_C1/Al0_C2 mass ratio yields a value of 5. Weak diffraction of (101) is observed for all samples. The (022) & (-222) diffractions at $\sim 0.335 \text{ \AA}^{-1}$ are clearly observed in Al10 and Al05 but less resolvable in Al0. The relative intensities and sharpness of the peaks associated with the c -axis indicate that stacking along this axis is more ordered in Al10 and Al05 than in Al0_C1. This verifies that Al-incorporation increases the crystallinity of C-A-S-H in these 80 °C samples, which is consistent with the laboratory X-ray diffraction results of these materials⁶.

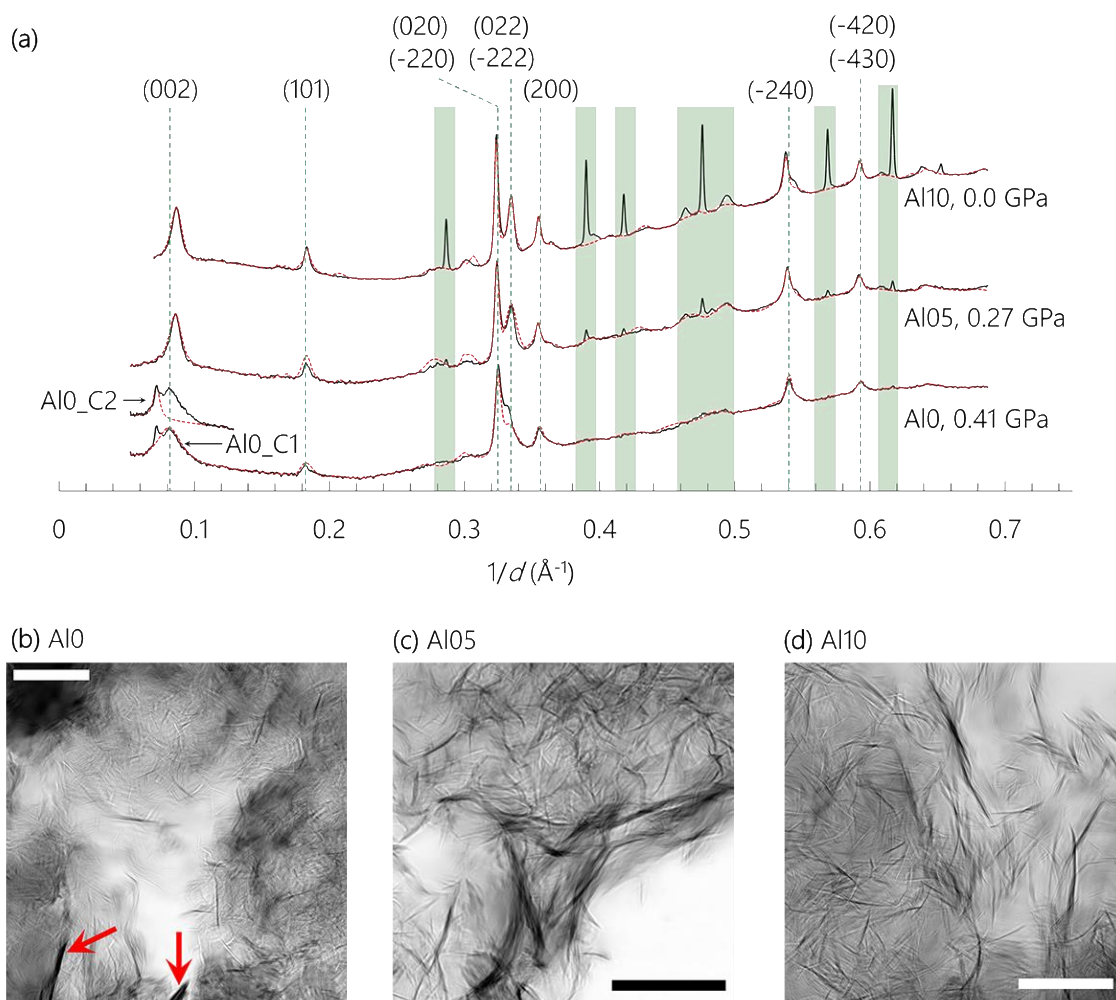


Figure 6.1 (a) Reference X-ray diffractograms (solid black curves) of Al0, Al05, and Al10 at 0.41, 0.27, and 0.0 GPa, respectively. Calculated diffractograms from Rietveld refinement are displayed as red curves. Typical diffraction peaks of C-(A-)S-H are assigned to their Miller indices (dashed vertical green lines). Diffraction from ruby and steel gaskets are masked by green strips. X-ray ptychographic imaging study was conducted on (b) Al0, (c) Al05, and (d) Al10. Scale bars are 1 μm . The Al0_C2 diffraction may come from the relatively large crystalline regions in (b), labeled by red arrows, whereas Al0_C1 is identifiable from the more abundant thin fibers.

The refinement results presented in Table 6.1 show that Al-incorporation increases the lattice parameters a and b since the typical AlO_4 tetrahedron ($\text{Al-O} \approx 1.75 \text{ \AA}$ in katoite ($\text{Ca}_3\text{Al}_2\text{O}_6 \cdot 10\text{H}_2\text{O}$), for instance⁸) is larger than the SiO_4 tetrahedron ($\text{Si-O} \approx 1.62 \text{ \AA}$ in 11 \AA tobermorite⁴). The basal spacing, however, is significantly reduced by Al-induced cross-linking in Al10 (11.5 \AA)⁶, which most likely also occurs in Al05 (11.6 \AA) due to the similarly significantly reduced basal spacing with respect to Al0_C1 (12.2 \AA) and Al0_C2 (13.8 \AA). The sharpness and relative intensities of the (002) peaks are highly sensitive to

the crystallite size along the *c*-axis (l_{cc}); therefore, refining l_{cc} yields uncertainties of 0.5-1 nm, while the other dimensions (l_{aa} and l_{bb}) with uncertainties of 5 nm. The Al0_C2 has a much larger crystallite size along the *c*-axis than Al0_C1 (15 and 3.5 nm, respectively). Compared with Al0_C1, Al-incorporation has at least doubled the size of nano-crystals along the *c*-axis in Al05 and Al10. The refinement of lattice parameter *a* is largely determined by the positions of the (200) peaks, whereas refining *b* mainly depends on the positions of the (020) & (-220) peaks in addition to *a*. Both lattice parameter values have uncertainties of ± 0.01 Å. Refinement of *c* is essentially independent of *a* and *b*, and is mainly determined by the (002) peak position (uncertainty of ± 0.1 Å). The refined results match the observed nano-scale morphologies (Figure 6.1b-2d) as the fibrillar precipitates are thicker and longer in Al05 and Al10 than in Al0. Relatively thick nano-crystals are identified in Al0, which are thus assigned to Al0_C2 (red arrows in Figure 6.1b).

Table 6.1 Refinement of the lattice parameters (*a*, *b*, and *c*) and crystallite sizes (l_{xx} , with *x* being *a*, *b*, or *c*) at ambient conditions. The uncertainties of the lattice parameters are determined as 0.01 Å for *a* and *b*, 0.1 Å for *c*, and 0.1 ° for angle γ .

	Al0	Al05	Al10
<i>a</i> (Å)	6.68 ± 0.01	6.69 ± 0.01	6.71 ± 0.01
<i>b</i> (Å)	7.33 ± 0.01	7.35 ± 0.01	7.36 ± 0.01
<i>c</i> (Å)	24.4 ± 0.1 (Al0_C1)	23.1 ± 0.1	22.9 ± 0.1
	27.6 ± 0.1 (Al0_C2)		
γ	$123.0^\circ \pm 0.1^\circ$	$123.0^\circ \pm 0.1^\circ$	$123.2^\circ \pm 0.1^\circ$
l_{aa} (nm)	18 ± 5	25 ± 5	25 ± 5
l_{bb} (nm)	25 ± 5	45 ± 5	45 ± 5
l_{cc} (nm)	3.5 ± 0.5 (Al0_C1)	7 ± 1	7.5 ± 1
	15 ± 1 (Al0_C2)		
l_{ab} (nm)	25 ± 5	45 ± 5	45 ± 5
l_{bc} (nm)	13 ± 5	20 ± 5	20 ± 5
l_{ac} (nm)	13 ± 5	20 ± 5	20 ± 5

6.2 High pressure XRD

When samples are exposed to increasing hydrostatic loading, all resolvable diffraction peaks of nano-crystalline C-(A-)S-H shift to higher $1/d$ values independent of the Al

content (Figure 5.2). The deformations are purely elastic as these peaks return to their original positions upon unloading.

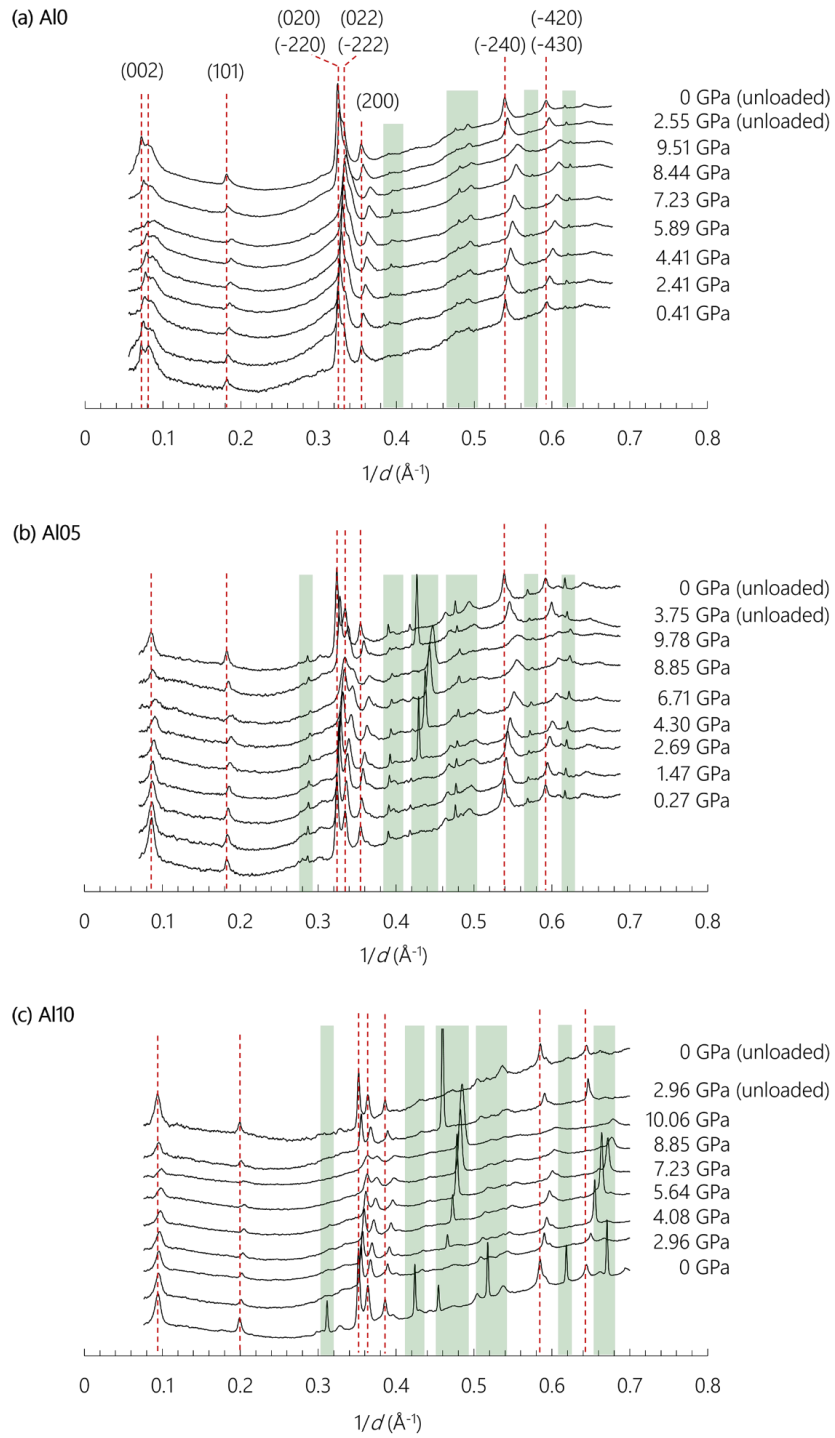


Figure 6.2 Normalized XRD diffractograms of Al0, Al05, and Al10 up to ~10 GPa. Vertical red dashed lines correspond to the reference C-(A-)S-H peaks positions at ambient pressure as eye guides. Two XRD patterns taken after unloading pressure are plotted for each sample. Diffraction from ruby and steel gaskets are masked by green strips. The determination of pressure has uncertainty of ~0.15 GPa.

Each individual peak broadens with increasing pressure, which is caused by reduced crystallinity and/or the development of micro-strain and are common phenomena observed in HP-XRD experiments⁹. The monotonically increasing peak shifting and the absence of peak splitting or the occurrence of new peaks imply no reconstructive crystal-structural change during the loading process. However, peak broadening does cause some adjacent peaks to merge, e.g., the (020) & (-220) peaks with the (022) & (-222) peaks in Al05 and Al10 at pressure > ~8 GPa.

The refinement protocol described above for the results shown in Figure 6.1 is used to fit the diffraction patterns shown in Figure 6.2, the results of which are plotted in the form of Biot strains ($\varepsilon = L/L_0 - 1$, where L and L_0 are the current and initial length of unit cell edge, respectively) in Figure 6.3a-4b. In a HP-XRD study of 14 Å tobermorite¹⁰, the angle γ was found to fluctuate within $\pm 0.1^\circ$ with hydrostatic pressure increased to ~5 GPa, which induces a volumetric strain ($\varepsilon_V = 1 - V/V_0$, where V and V_0 are the observed and initial unit cell volume) of ± 0.001 and is negligible in determining bulk modulus. Hence, γ was fixed to its respective values in each sample at ambient condition (Table 6.1), leaving only a , b and c to be refined.

The stiffness of the nano-crystalline C-(A-)S-H along the a - and b -axes are comparable and independent of their Al content (Figure 6.3a). These axes deform monotonically as functions of pressure up to ~10 GPa, with average compliance (defined as the absolute value of the slope of the ε - P plot) $\approx 3.3\%$ per 10 GPa. Similar compliances have been reported for synthetic C-S-H(I)¹⁰ and 14 Å tobermorite¹⁰, which implies that the ab -planar stiffness of C-(A-)S-H is not significantly influenced by the extent of bridging site vacancies, nor Al for Si substitution in their dreierketten chains.

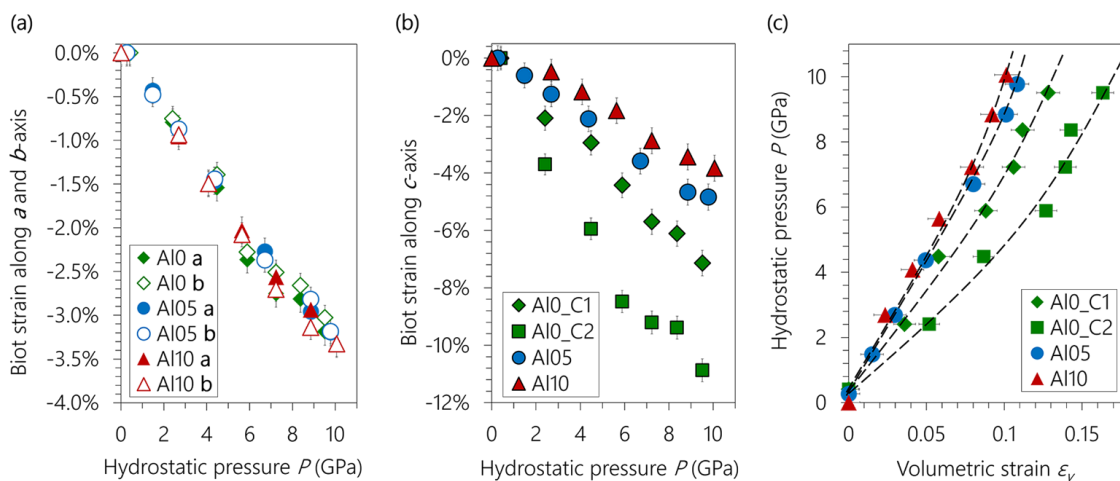


Figure 6.3 Biot strains as functions of applied hydrostatic pressure along (a) *a*- and *b*-axes, and (b) *c*-axis. (c) Pressure as a function of volumetric strain. The error bars of the axial Biot strains and the volumetric strain originate from the refinement uncertainties (see Table 6.1). The uncertainty of pressure is estimated to be ~ 0.15 GPa. Dashed curves in (c) illustrate the fitted results of BM-EoS.

Deformation along the *c*-axis in Al0 is roughly linear, with compliance $\approx 7\%$ per 10 GPa for Al0_C1, and $\approx 11\%$ per 10 GPa for Al0_C2 (Figure 6.3b). The material is clearly softer along the *c*-axis than within the *ab*-plane. The compliance of the *c*-axis in Al_C2 is consistent with reported data for that found in 14 Å tobermorite macro-crystal¹⁰. As its ambient lattice parameter *c* (27.6 Å) is also consistent with that of 14 Å tobermorite (27.99 Å¹⁰), Al_C2 is most probably nano-crystalline 14 Å tobermorite. This conclusion corroborates existing work which demonstrates that 14 Å tobermorite is often found intermixed with normal 11 Å tobermorite in the absence of Al (i.e., Al_C2 and Al_C1, respectively) but not in the presence of Al (i.e. the case of Al05 and Al10)¹². Compared with Al0, the *c*-axis is clearly stiffer in the Al-containing samples, which stiffens as the Al content increases. The compliance along the *c*-axis of Al10 ($\sim 4\%$ per 10 GPa) is almost comparable to those along the *a*- and *b*-axes.

The bulk modulus K_0 under ambient pressure is fitted from Figure 6.3c using Birch-Murnaghan equation of state (BM-EoS, see methods, Equations (1) and (2)). Note that K_0' is often suggested as having a constant value of 4 for zeolites^{10,13}, thus, leaving K_0 as the only fitted parameter in Equation (2). The results of these fits are shown in Table 6.2. The K_0 of Al0_C2 (36 ± 1 GPa) is comparable to the reported value for macro-crystalline 14 Å tobermorite (47 ± 4 GPa), further supporting the interpretation herein that this material may be nano-crystalline 14 Å tobermorite¹⁰. The Al0_C1 has a significantly smaller basal spacing than Al0_C2 (12.2 Å versus 13.8 Å shown in Figure 6.4), which makes its *c*-axis less deformable and causes its ambient pressure bulk modulus to increase by $\sim 40\%$, to 50 ± 2 GPa. The presence of similar intralayer structures and the absence of cross-linking in both materials leads to the hypothesis that the interlayer, which is filled with zeolitic

contents (i.e., mainly water and Ca^{2+}), is much softer than the intralayer and therefore originates most of the deformation along the c -axis.

Table 6.2 Fitted K_0 values from the refined lattice parameters with BM-EoS equation. Linear fitting with two-dimensional errors follows the York method¹⁴.

	K_0 (GPa)	K_0'
Al0_C1	50 ± 2	4 (assumed)
Al0_C2	36 ± 1	4 (assumed)
Al05	64 ± 3	4 (assumed)
Al10	71 ± 3	4 (assumed)

Al-incorporation further reduces the basal spacings of C-A-S-H to 11.6 Å (Al05) and 11.5 Å (Al10). Although this additional reduction is less than that occurs from Al0_C2 to Al0_C1, the ambient pressure bulk modulus significantly increases to 64 ± 3 (Al05) and 71 ± 3 GPa (Al10). Therefore, the nano-crystalline C-(A-)S-H analyzed here become stiffer with increasing Al incorporation. A contradictory result was obtained for C-A-S-H in alkali activated slag (AAS), where no Al-induced stiffening was observed compared to C-S-H(I) synthesized at room temperature¹⁰. The basal spacing of that C-A-S-H (AAS) at ambient pressure is 12.44 Å, which is too wide to allow cross-linking. Thus, cross-linking appears to be the key factor that significantly increases the stiffness of the C-A-S-H samples studied herein. As shown in Figure 6.4, the cross-linked tetrahedra between adjacent dreierketten chains may act as supporting ‘columns’ that withstand the closing of the porous interlayer.

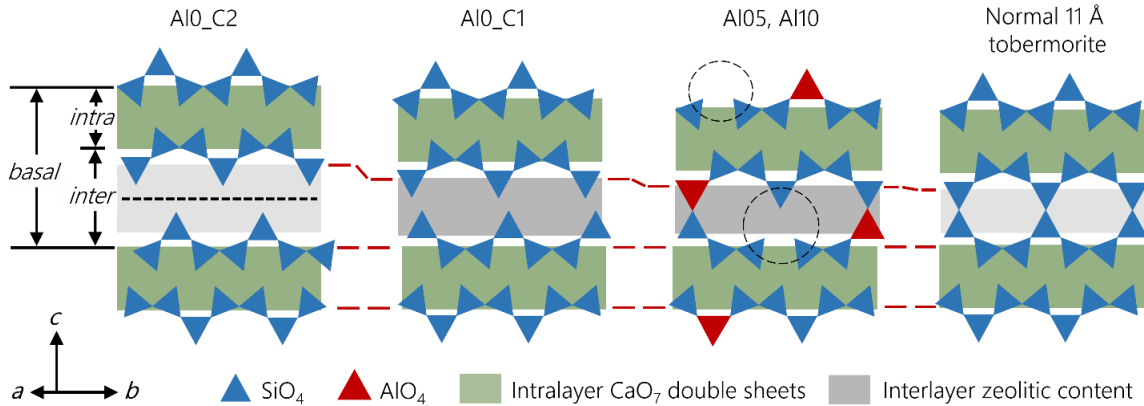


Figure 6.4 Schematic comparison of atomistic configurations of C-(A-)S-H in the samples analyzed here and in normal 11 Å tobermorite. The darkness of the grey band in the interlayer illustrates the concentration of the zeolitic content (e.g., interlayer water and Ca^{2+} , dark = more concentrated and light = less concentrated). A $b/2$ glide plan

(black short-dashed line) is assumed in AlO_C2 following 14 Å tobermorite¹⁰. The black dashed circles indicate non-cross-linked sites due to missing bridging tetrahedra. The red long-dashed lines are eye guides to view the changing basal and interlayer spacing. The terms *basal*, *inter*, and *intra* represent basal, interlayer, and intralayer spacing, respectively.

Cross-linked normal and anomalous 11 Å tobermorite structures⁹ are reported to have bulk moduli of 71(4) GPa (normal) and 63(2) GPa (anomalous)¹⁵, which is within the range defined by the moduli of AlO5 and Al10. The difference between normal and anomalous 11 Å tobermorite may be attributed to different concentrations of zeolitic content (i.e., Ca²⁺ and water) in their interlayer space: Ca_{zeolitic}/Si = 0.08 and 0 in normal and anomalous, respectively, and H₂O_{zeolitic}/Si = 0.83 for both⁹. The presence of zeolitic contents would enhance the steric constraints of the interlayer, thus increasing the bulk modulus. As a comparison, AlO5 and Al10 studied herein have more zeolitic contents (Ca_{zeolitic}/Si+Al = 0.25-0.3, and H₂O_{zeolitic}/Si = 1.1-1.2⁶), but their bulk moduli are not higher than normal 11 Å tobermorite because the cross-linking sites in C-A-S-H samples are not as abundant as that found in normal 11 Å tobermorite due to the missing bridging tetrahedral, as indicated by the black dashed lines in Figure 6.4.

Atomistic simulations of defective tobermorite with Ca/Si \approx 1.0 yield results (53-62 GPa¹⁶ and 55-65 GPa¹⁷) consistent with the bulk modulus of AlO_C1 measured herein (50 \pm 2 GPa). Calculated values of the bulk modulus of crystalline 14 Å tobermorite (35.91 GPa¹⁸ and 46 GPa¹⁹) are also consistent with the measured value of AlO_C2 here (36 \pm 1 GPa). Therefore, it is concluded that the current computational simulations provide reliable predictions of C-S-H. In comparison, the Al-incorporated structure has not been modelled as much as C-S-H. Here, experiment evidence on C-A-S-H is provided to validate future simulations. It is reasonable to conclude that this ‘bottom-up’ approach to simulate and thus optimize the mechanical properties of C-(A-)S-H-based cementitious material is currently promising given accurate atomistic representations of the C-(A-)S-H phase, which can be derived from experimental results discussed herein.

6.3 Discussions and Conclusion

This paper reports on an analysis of the mechanical behavior of nano-crystalline C-(A-)S-H under hydrostatic load with synchrotron radiation-based HP-XRD; results are supported by ptychographic imaging. These experiments test the lattice deformation of nano-crystalline C-(A-)S-H and for the first time systematically correlates its atomistic structures and mechanical properties. The work contributes fundamental knowledge to the understanding of the morphology and structure of nano-crystalline C-(A-)S-H, which can be used to build and validate more realistic simulation models of this material at atomistic- and nano-scales. Highlights are summarized as follows:

1. Through Rietveld refinement, it is verified that Al-incorporation increases the crystallinity of C-(A-)S-H, especially along the *c*-axis. Al-induced cross-linking is

observed in C-A-S-H synthesized at 80 °C, which has a similar basal spacing to 11 Å tobermorite. The cross-linked AlO_4 and SiO_4 tetrahedra may act as supporting ‘columns’ along the *c*-axis that resist closing of the interlayer space subjected to hydrostatic compression, thus increasing the overall bulk modulus. The overall bulk modulus is also correlated to the concentration of the zeolitic contents (i.e., water and Ca^{2+}) and negatively correlated to the interlayer spacing.

2. The *ab*-planar deformation under hydrostatic pressure reported herein is highly reproducible throughout all of the reported HP-XRD studies of C-(A-)S-H and tobermorite crystals synthesized in distinct conditions, leading to the conclusion that the dreierketten chain defects, e.g., bridging site vacancies and Si for Al substitution, do not change the stiffness of these materials along the *a*- and *b*-axes.

3. Atomistic simulations of C-S-H using defective tobermorite structures as a starting point yield generally comparable bulk moduli values to those determined here. Experimental discoveries of Al-incorporated samples reported have not been reported previously, and these simulations may help to improve current simulating packages to better serve the purpose of designing innovative C-(A-)S-H-based cementitious materials using a ‘bottom-up’ approach.

6.4 References

1. Taylor, H.F.W. *Cement chemistry, second ed.* (Thomas Telford 1997).
2. Grangeon, S., Claret, F., Linard, Y. & Chiaberge, C. X-ray diffraction: a powerful tool to probe and understand the structure of nanocrystalline calcium silicate hydrates. *Acta Crystallogr. Sect. B-Struct. Sci.* **69**, 465-473 (2013).
3. Battocchio, F., Monteiro, P.J. & Wenk, H.R. Rietveld refinement of the structures of 1.0 CSH and 1.5 CSH. *Cem. Concr. Res.* **42**, 1534-1548 (2012).
4. Merlino, S., Bonaccorsi, E. & Armbruster, T. The real structure of tobermorite 11 Å normal and anomalous forms, OD character and polytypic modifications. *Eur. J. Mineral.* **13**, 577-590 (2001).
5. Lutterotti, L. & Scardi, P. Profile fitting by the interference function. *Adv. X-Ray Anal.* **35**, 577-584 (1991).
6. Lutterotti, L., Matthies, S. & Wenk, H.R. MAUD: a friendly Java program for material analysis using diffraction. *IUCr: Newsletter of the CPD*, **21**, 14-15 (1999).
7. Myers, R.J., L'Hôpital, E., Provis, J.L. & Lothenbach, B. Effect of temperature and aluminium on calcium (alumino) silicate hydrate chemistry under equilibrium conditions. *Cem. Concr. Res.* **68**, 83-93 (2015).

8. Lager, G.A., Armbruster, T. & Faber, J. Neutron and X-ray diffraction study of hydrogarnet $\text{Ca}_3\text{Al}_2(\text{O}_4\text{H}_4)_3$. *Am. Mineral.* **72**, 756-765 (1987).
9. Wenk, H.R., Lutterotti, L. & Vogel, S.C. Rietveld texture analysis from TOF neutron diffraction data. *Powder Diffr.* **25**, 283-296 (2010).
10. Oh, J. E., Clark, S.M., Wenk, H.R. & Monteiro, P.J. Experimental determination of bulk modulus of 14Å tobermorite using high pressure synchrotron X-ray diffraction. *Cem. Concr. Res.* **42**, 397-403 (2012).
11. Oh, J.E., Clark, S.M. & Monteiro, P.J. Does the Al substitution in C–S–H (I) change its mechanical property? *Cem. Concr. Res.* **41**, 102-106 (2011).
12. Mitsuda, T. & Taylor, H.F.W. Influence of aluminium on the conversion of calcium silicate hydrate gels into 11 Å tobermorite at 90 °C and 120 °C. *Cem. Concr. Res.* **5**, 203-209 (1975).
13. Prewitt, C.T. & Downs, R.T. High-pressure crystal chemistry. *Rev. Mineral.* **37**, 284-318 (1998).
14. York, D. Least-squares fitting of a straight line. *Can. J. Phys.* **44**, 1079-1086 (1966).
15. Moon, J. Experimental and Theoretical Studies on Mechanical Properties of Complex Oxides in Concrete. PhD thesis, 2013, University of California, Berkeley: Civil and Environmental Engineering, <http://escholarship.org/uc/item/6z52s8zg>.
16. Pellenq, R. J. M., Lequeux, N. & Van Damme, H. Engineering the bonding scheme in C–S–H: The iono-covalent framework. *Cem. Concr. Res.* **38**, 159-174 (2008).
17. Qomi, M. A., *et al.* Combinatorial molecular optimization of cement hydrates. *Nat. Commun.* **5**, (2014).
18. Shahsavari, R., Buehler, M. J., Pellenq, R. J. M. & Ulm, F. J. First-principles study of elastic constants and interlayer interactions of complex hydrated oxides: Case study of tobermorite and jennite. *J. Am. Ceram. Soc.* **92**, 2323-2330 (2009).
19. Manzano, H., Dolado, J.S., Guerrero, A. & Ayuela, A. Mechanical properties of crystalline calcium-silicate-hydrates: comparison with cementitious C-S-H gels. *Phys. Status Solidi A*, **204**, 1775-1780 (2007).

7. A nano- and micro-structural study of a 50-year-old hydrated C₃S paste

Most existing studies of C₃S hydration focus on the first few months of C₃S hydration. Following the service life timeline, this chapter investigates a 50-year-old hydrated alite (96% C₃S) paste, at the nano- and micro-scale, aiming at understanding the chemistry and microstructure of C₃S hydrates at the late age of concrete service life. Lab XRD was used to characterize the crystalline phases in the paste. SEM and TEM were used to image the microscale and nanoscale morphology of CH and C-S-H. NMR was used to investigate the silicate chain linkage of C-S-H after 50 years storage. STXM experiments provided the chemical environmental information of C, Ca and Si. An atomic configuration of the 50-year-old C-S-H was then proposed based-on the experimental evidences.

7.1 XRD

XRD measurements were conducted for the core part (CP) and surface part (SP) of a 50-year-old C₃S paste cylinder, using a Co *k* α wave. In the XRD shown in Figure 7.1, for both CP and SP, three phases can be identified, Ca(OH)₂ (CH), C₃S and C-S-H. Unsurprisingly, CH is the most dominant phase in both plots, since this is the major crystalline hydration product. As it would be expected due to its lack of crystallinity, the C-S-H phase exhibits no sharp peaks on the plots. Instead, a broad peak from 33 ° to 38 ° can be assigned to the C-S-H structure. With a corresponding spacing of 2.7 to 3.1 Å, which confirms the poorly crystallized nature of C-S-H in hardened C₃S paste. Similarly broad peaks were observed by Bergold¹, where the C-S-H (alite paste at 23 °C with w/s = 0.5 after 65h of hydration) peak values are almost identical with those reported herein.

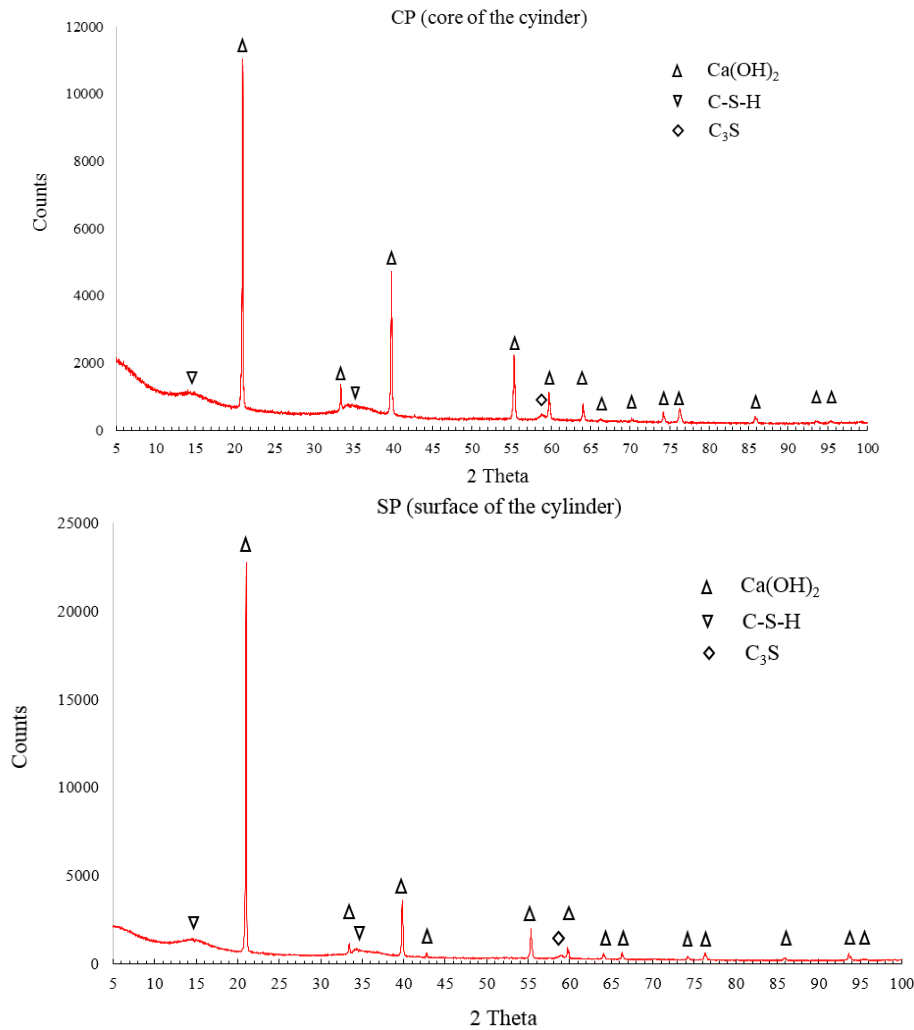


Figure 7.1 XRD results of CP (core of the cylinder) and SP (surface of the cylinder). A $Co\ k\alpha$ wave was used.

A small peak at $2\theta = 59^\circ$ is assigned to C_3S ^{1,2}. The intensity is significantly low so that hydration degree can be concluded to near 100%. Note that there are no peaks that can be assigned to $CaCO_3$. It can be claimed that the paste is not carbonated even after 50 years; this is also supported by the results of the NMR and STXM study, discussed below. In summary, the XRD study proves that, over the span of 50 years almost complete hydration has occurred with zero carbonation. The C-S-H remains poorly crystalline as at the very early age.

7.2 SEM

Usually under the secondary electron (SE) mode, different components, such as unreacted C_3S , Ip C-S-H and Op C-S-H, are less distinguishable. Only under back scattered electron

(BSE) mode can they be identified by greyscale value. However, in this 50-year-old C_3S paste sample, SE images show unique features that allow identification of different components (Figure 7.2).

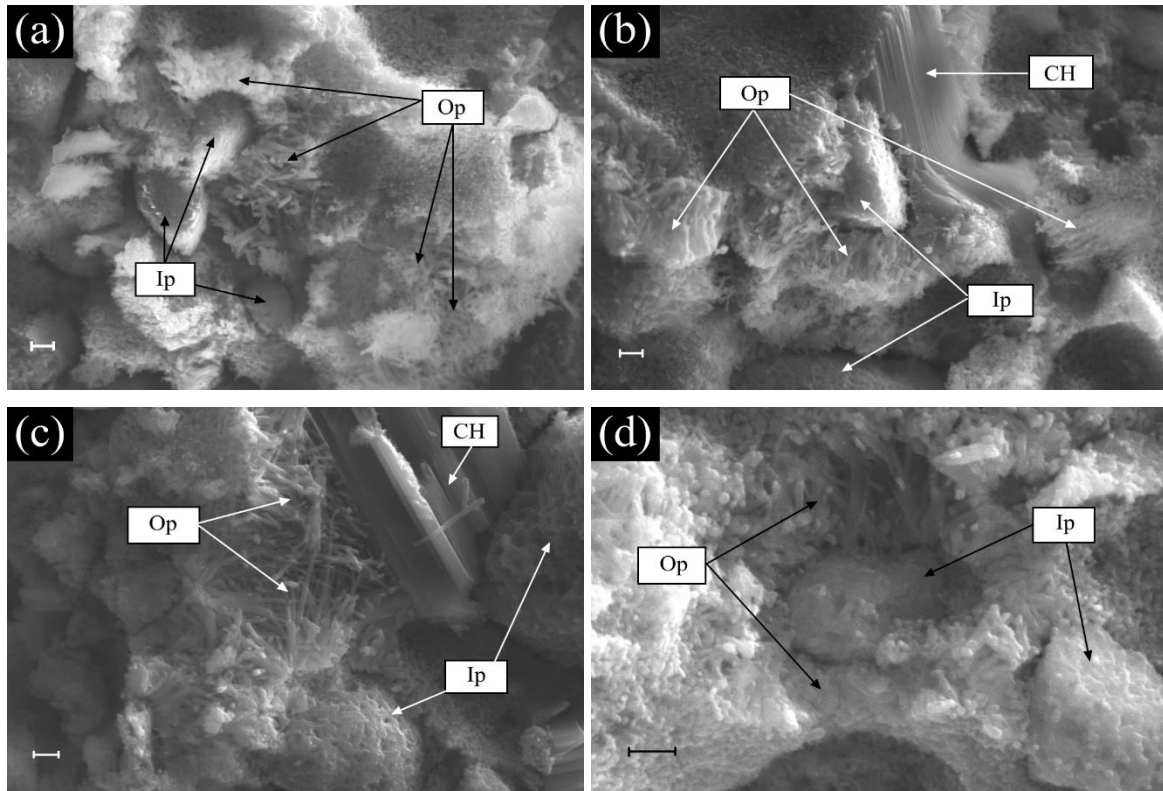


Figure 7.2 Secondary electron image on different locations in CP (core of the cylinder), scale bar of 1 μm

The SEM results support those indicated by XRD data, in that the sample contained almost no unreacted C_3S . As shown in Figure 7.2, three features are exposed on the broken surface: 1) interlaced fibers that form the matrix; 2) globular core with rough surfaces, surrounded by fibrillar matrix; and 3) a crystalline phase in plate-shape. These are identified as Op C-S-H, Ip C-S-H and CH respectively. The reasoning is as follows: The fibrillar material distributed throughout the whole matrix is oriented in a radial fashion outside the globular core. The thickness of the fibers is approximately 150-250 nm (most fibers are of uniform thickness). Recall that in the early age hydration that fibrillar Op roots on the boundary between Ip and Op C-S-H, in a radial format³. When the Op of adjacent C_3S particles interlaces with each other, the mixture sets and begins to gain strength. Therefore, the universally existing fibrillar material in the 50-year-old sample most probably comes from the early age fibrillar Op. Because the XRD results determined that the amount of unreacted C_3S is negligible, the globular core must be the inner product, containing, most likely, very small amount of C_3S . Lastly, being the only crystalline phase in the sample, CH must

account for the large plates in the images, whose smooth surface and sharp edge strongly indicate crystalline morphology.

The EDS data were collected at various locations in Figure 7.2 (the labels of these locations are assigned according to the above analysis), as summarized in Table 7.1. The Ca/Si ratio of Ip and Op C-S-H is consistent with other studies⁴. Reported Ca/Si ratio of C-S-H in pure C₃S paste is ~1.7, which is about the same as the Ip C-S-H (~1.68), but smaller than the Op C-S-H (~2.02) in this study. The highly observed Ca/Si ratio in Op C-S-H indicates a higher Ca-OH bonds content in the Op zone. These bonds are either in solid solution state inside C-S-H (as suggested by Richardson⁵) or have formed nanoscale fine crystalline CH which is too small to be distinguished from C-S-H.

Table 7.1 Statistics of EDS data of the 50-year-old C₃S paste

Phases	# of testing	Average atomic Ca/Si	Standard Deviation
Ip C-S-H	11	1.68	0.15
Op C-S-H	6	2.02	0.15
CH	3	14.12	2.41

Many researchers have suggested that the Ip is more likely to form in an *in-situ* reaction pattern, i.e. product forms where reactant is. However, the Ca/Si ratio (~1.68) of Op C-S-H is much smaller than the original C₃S. This suggests that, although the Ip is denser than Op^{6,7}, Ca²⁺ ions are efficient in migrating to the Op zone. It is worth mentioning that EDS under SE model is more qualitative than quantitative, due to shadowing effect of uneven surface. Besides, the signal comes from 0-3 μm beneath the surface, while the material of interests could be only 1 μm thick⁷. But considering the standard deviation, the tendency is reliable as a comparison within this study and other published SEM-EDS results.

7.3 TEM

In conducting the TEM measurement, great care was taken in order to find a particle that contained both Ip and Op C-S-H but no CH. The crystal structure of CH would greatly affect tomographic collection and introduce artifacts. Images of particles at various rotation angles are shown in Figure 7.3 in series from (a) to (f). Slice images from the 3D acquisition are provided here instead of the 3D reconstruction, this is because there was no single complete data set collected from -65 °to 65 °, without beam damage or the gain moving from view. As a result the missing wedge of the sample largely decreases the resolution of the 3D reconstruction, and therefore in this case 2D images are better in showing details. As the sample rotates from (a) to (f), one part (area P) of the particle disappears and the other (area Q) appears. It is concluded that the observed particle is a conjunction of Op C-S-H (area P) and Ip C-S-H (area Q) with a total dimension of about 150nm. White arrows in Figure 7.3(b) mark the boundary between Ip and Op C-S-H. The rationale is explained as follows.

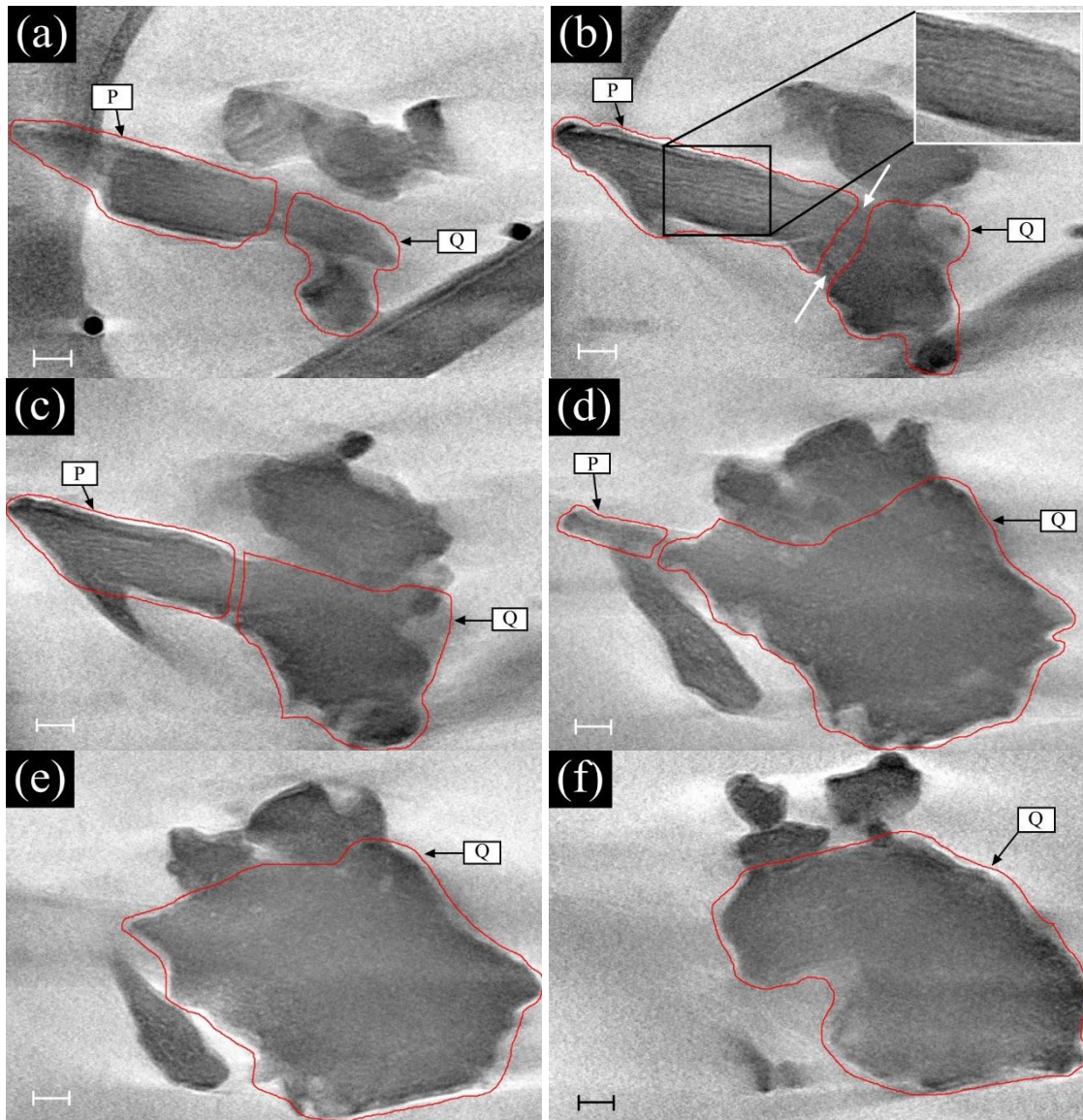


Figure 7.3 A series of slices from the reconstruction of a particle in C_3S paste, which is unidirectionally rotated from (a) to (f); bar length is 20nm. Area P and Q are, respectively Op and Ip C-S-H respectively. During rotation the feature of area Q increases while that of area P fades.

The determination of Ip and Op C-S-H in the image series is based on the TEM morphological observation of C_3S pastes obtained from the literature^{5,3,9}. The Op C-S-H of C_3S paste in previous research always exhibits a fibrillar shape, rooting on the surface of Ip-Op boundary. Although it can alter to foil-like Op C-S-H when the hydration environment is rich in Ca^{2+} , Al^{2+} (for instance in the case of $CaCl_2$ or alkali activation / Slag addition⁵), the Op C-S-H in pure C_3S paste (and in also C_2S paste⁵) is fibrillar all through the hydration process. The diameter seems to grow from several tens of

nanometers at very early age to about 100nm at eight years old, and eventually to ~200 nm at 50-year-old, as indicated by the SEM results in this work.

The Ip C-S-H in this sample, meanwhile, appears to be the aggregation of globular particles. At a finer scale (<10nm), the Op C-S-H fibers are composed of large numbers of long thin particles aligned along its length. The particles are about 1.5-2 nm in their smallest dimension and can be a few nanometers to many tens of nanometers long. Adjacent particles are separated by a transparent layer around 1.5 nm thick, which is most likely to be water layers when the sample is in moisture¹⁰. Based on these observations, area P is considered to be Op C-S-H because of its alternating lamellar structure of long-thin particles and water layer. The thickness of the particle is 1.5-2 nm and the water layer 1.5 nm, which is in good agreement with Richardson's work on C₃S pastes⁵.

Area Q has similar morphology as the Ip C-S-H reported in other studies^{5,9}. Unlike the fibrillar Op C-S-H, the Ip C-S-H appears to be the aggregation of globular particles. This results in a denser packing than Op. Besides, the texture of Ip is rather homogenous, while that of Op is with a preferred growing direction.

7.4 NMR

To determine the silicon anion structure present in the C-S-H phases, ²⁹Si MAS NMR was used to obtain quantitative information of the fraction of silicon present in different tetrahedral environments. The original spectrum shown in Figure 7.4 has only two resolvable peaks at shifts of -79.0 and -85.1 ppm. Anhydrous C₃S contains nine distinctive silicate anion environments, which are represented in a spectrum as five resolvable peaks in the range of around -68 to -75 ppm¹¹. As there is no indication of any peaks in this range, it can be concluded that the C₃S was fully reacted, which is in agreement with the results obtained from the XRD. Because the spectrum has zero intensity in the range of -89 to -103 ppm there are no Si anions in either chain branching sites or three dimensional frameworks (Q³ or Q⁴) that form when pastes carbonate¹², confirming that the C-S-H has not been carbonated, which is also in agreement with XRD results.

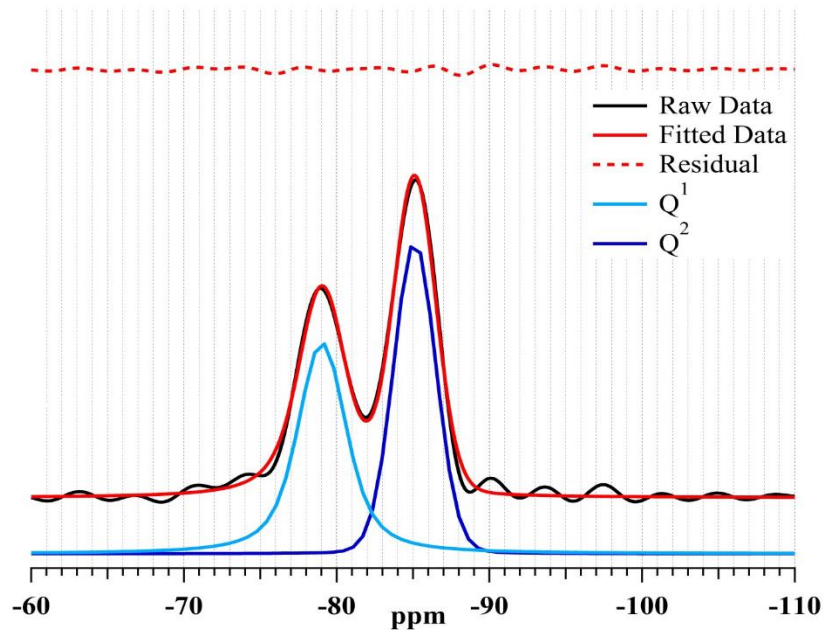


Figure 7.4 ^{29}Si NMR spectrum of 50-year-old C_3S paste, deconvoluted to Q^1 (-79.0) and Q^2 (-85.1). All y-axis are set to the same intensity.

From integration of the areas under each deconvoluted peak, it is possible to calculate the percentage of Si atoms in each environment, and compare this with a sample of C_3S over a range of hydration length from 12 hours to 26 years¹³. The results obtained from that study are given in Figure 7.4 with the additions of the MCL. The 50-year-old sample was cured in saturated limewater for three years and then sealed in a plastic bottle. After half-century hydration, the Mean Si tetrahedron Chain Length (MCL) is only 4.18, compared with 2 at 12 hours and 3.27 at 1 year¹³. The polymerization process is so slow, that one can expect within the normal service life time (50 to 100 years), C-S-H in C_3S hydration product would always remain low degree of polymerization.

The results in Table 7.2 suggest that dimers are formed first from monomers (Q^0), then longer chains can be formed (Q^2) from the linking of dimers with monomers, but chains longer than dimers do not form directly from monomers alone. This is verified by the work of Lippmaa *et al*, who reported a reduction but not a complete halt in monomer consumption and Q^1 production during the formation of Q^2 units¹¹. If Q^2 units were formed directly from monomers, the consumption of monomers would most likely increase, as more units are needed in chains than in dimers. The results in the table also show that significant quantities of Q^2 units are not formed until a minimal amount of monomers remain. As Lippmaa *et al* found Q^1 production declines with initial Q^2 production; there is the indication that regardless of the degree of hydration of the paste, C_3S systems are not able to form both dimers and longer chain simultaneously.

Table 7.2 Quantity of Si anions in each environment as a percentage obtained from integration of the peak areas. Data from 12 hours to 26 years are from Rodger¹³.

Age	Q ⁰	Q ¹	Q ²	MCL
12 hours	89	11.0	0.0	2.00
1 day	68	30.0	2.0	2.13
7 days	48	43.0	9.0	2.42
14 days	33	52.0	15.0	2.58
1 month	30	53.0	17.0	2.64
3 month	18	62.0	20.0	2.65
6 month	14	65.0	21.0	2.65
1 year	10	55.0	35.0	3.27
2 years	6	52.0	42.0	3.62
26 years	0	42.0	58.0	4.76
50 years	0	47.9	52.1	4.18

The formation of Q² units does not start until over 30% of anions are present as dimers, once this has occurred the percentage of dimers present never falls below 40%, even after 40 years; see Taylor et al.¹⁴. As the method of polymerization is that of linking dimers and monomers, the most likely reason for the discontinuation of dimer consumption in order to form longer chains is the absence of any monomer species at this stage. If this is the case, it would also indicate that dimers cannot link with each other and as such the sequence of chain lengths is possible (3n-1). As observed by TEM, the fine particles in Op C-S-H can be as long as several tens of nanometers, much longer than the MCL (4.18 SiO₄⁴⁻ tetrahedrons, which is about 1.1nm¹⁵). There is a missing link from this short SiO₄⁴⁻ tetrahedron chain to the long-thin particle. According to Richardson^{5,16}, this can be explained by Ca²⁺ replacing the bridging SiO₄⁴⁻ tetrahedron in the regular tobermorite structure, or the protonation of oxygen atom that decreases the length of Si chain. This model explains the phenomena (such as MCL and Ca/Si) but it has been difficult to prove experimentally. The STXM results discussed below provide some new evidence.

7.5 STXM

NEXAFS (near edge x-ray absorption fine structure) provides abundant information about bonding and coordination state of absorbing atoms and STXM allows *in-situ* NEXAFS study at local area of solid material¹⁷. Multiple factors can affect the fine structure of absorption spectra. Absorption peaks can either be assigned to the excitation of inner-shell electrons to outer-shell energy levels, or the multi-scattering process of photon-electron interaction. These fine structures are sensitive to the electron structure; e.g., when the degree of polymerization increases, the major peak in Si K-edge increases also. In Ca L_{3,2}-edge, when the symmetry of coordination is altered, a split in major-absorption peaks can

be observed and the difference in the intensity ratio among the peaks can provide qualitative information on the degree of structural distortion. In the research reported here, the results of NEXAFS of Ca $L_{3,2}$ -edge, Si K -edge and C K -edge of 50-year-old hydrated C_3S sample (C_3S50) were studied; a 1.5 year C_3S paste ($C_3S1.5$) was also studied for comparison.

Ca $L_{3,2}$ -edge

STXM results of Ca $L_{3,2}$ -edge are shown in Figure 7.5. Stack data were collected from two particles: (a) C_3S50 and (b) $C_3S1.5$. As described in previous section, stack data contain the NEXAFS information of each pixel in the field of view. By comparing the spectra of different area, one can distinguish between various components. The hydrated particles in Figure 7.5(a) were not damaged during sample preparation, enabling *in-situ* observation. Through investigating the NEXAFS spectra of each pixels of the whole image, two representative spectra were extracted, as shown in Figure 7.5(c). One was collected from site 1, a margin area of a particle in Figure 7.5(a), and the other from site 2 on a bulk particle. In Figure 7.5(b), two representative spectra were also extracted, after examining spectra of each local area in the field of view.

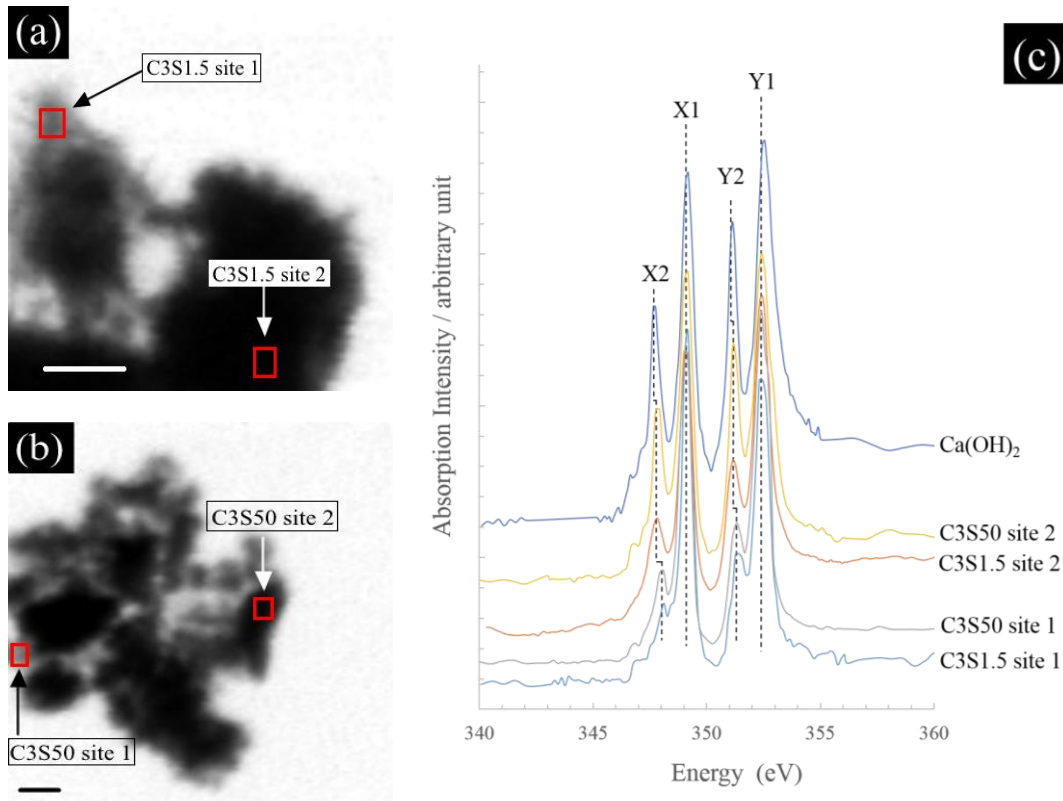
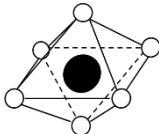
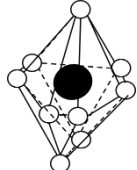


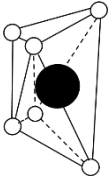
Figure 7.5 Ca $L_{3,2}$ -edge, scale bar length 500nm: absorption image of (a) $C_3S1.5$ and (b) C_3S50 ; (c) NEXAFS spectra of hydrated C_3S samples, compared with that of pure CH. Spectra of CH is from reported data¹⁹.

The Ca $L_{3,2}$ -absorption edge spectra corresponds to the excitation from Ca 2p to 3d orbitals. Two major peaks (X1 and Y1) can always be observed due to of the loss of degeneracy of 2p orbitals by spin-orbital interaction¹⁸. Despite the chemical status of Ca, these two major peaks are observed in the $L_{3,2}$ -edge spectra of most Ca-containing minerals. The symmetry of CaO_x coordination complex could further break the degeneracy of states, resulting in two minor peaks to the left of major ones. This phenomena was well explained by crystal field theory, which was later combined with molecular orbital theory and developed to ligand field theory¹⁸. In case of perfect octahedral symmetry, two major peaks are strongly splitted so that the intensity of the minor peaks are comparable to those of the major peaks. Besides, the energy differences between major and minor peaks are also significant.

Table 7.3 classifies the Ca coordination status into two categories based on their coordination symmetry. When the coordination is in octahedral symmetry (or near octahedral symmetry), such as the case of CH, calcite and dolomite, the spectra will be strongly affected by “crystal field” effect. Significant splitting in major peaks X1 and Y1 is allowed, and strong minor peaks X2 and Y2 could be observed in this case. The energy difference between adjacent major and minor peaks is 1.2~1.4 eV. Spectra of CH is shown in Figure 7.5(c). Examples of calcite and dolomite can be found in^{18,21}. Meanwhile in aragonite and gypsum, the coordination symmetry of Ca is rather irregular, which is considered to be a “weak crystal field”. In this case, the 3d orbital is less degenerated and minor peaks (X2 and Y2) change in two ways: they decrease in intensity, and they shift to higher energy. This makes the minor peaks less distinguishable on the NEXAFS spectra, as well as shorten the distance between major and minor peaks. This observation, verified by study of many minerals, can therefore be applied to the interpretation of Ca coordination status in C-S-H and CH.

Table 7.3 Peak characters from the Ca $L_{3,2}$ -edge spectra, some data are from reported results^{18,21}. The solid spheres are Ca at center atoms, and the hollow ones are ligand atoms.

Compound	$\Delta X/\text{eV}$	$\Delta Y/\text{eV}$	Symmetry of coordination
Pure CH	1.4	1.4	Octahedral 
CH in C ₃ S50 (site 2)	1.3	1.3	
CH in C ₃ S1.5 (site 2)	1.3	1.3	
Calcite	1.2	1.3	
Dolomite	1.3	1.3	
Aragonite	0.8	0.8	Irregular 

Gypsum	0.9	0.9	Irregular	
C-S-H in C ₃ S50 (site 1)	0.9	1.1	Unknown	
C-S-H in C ₃ S1.5 (site 1)	1.0	0.9		

C-S-H and CH are the two main hydration products. Ca in CH is in perfect octahedral symmetry and a strong splitting is observed in its $L_{3,2}$ -edge spectra, as shown in Figure 7.5(c). Energy difference between major and adjacent minor peak is ~ 1.4 eV. $L_{3,2}$ -edge spectra of C-S-H was also reported in earlier literatures^{22,20}, which exhibited weak splitting. In Figure 7.5, spectra of site 1 in both samples exhibit weak splitting, with energy difference between major and minor peaks of 0.9-1.1 eV, while energy differences on spectra of site 2 in both samples are ~ 1.3 eV. Therefore we assign site 1 in to C-S-H-rich region and site 2 to CH-rich region. Also from a morphological point of view, site 1 in Figure 7.5(a) locates on fibrillar margin area of hydrated particle, resembling the morphology of Op C-S-H. In Figure 7.5(b), not much morphological information is evident, since the grinding process largely altered the microstructure.

The small energy difference and the low intensity of minor peaks, of C-S-H in both C₃S50 and C₃S1.5, are similar with the spectra of aragonite and gypsum, as shown in Table 7.3. The relative weak crystal field effect in C-S-H indicates poor symmetry of Ca coordination structure. Spectra of Ca in CH of both samples share the same feature with spectra of pure CH, as well as calcite and dolomite¹⁸. It's worth pointing out that the major peaks X2 and Y2 are consistent among all spectra. Changing of chemical environment seems to be solely indexed by intensity and energy values of minor peaks.

Si *K*-edge

STXM results at Si *K*-edge are shown in Figure 7.6. Since Si *K*-edge has a higher absorption energy (compared to Ca $L_{3,2}$ -edge) and therefore ensures greater penetration depth, resulting in more morphological details under microscope in the absorption images. In C₃S1.5 (Figure 7.6(a) and (b)), fibrillar Op C-S-H covers the surface of C₃S particles, while the core area appears to be featureless. In C₃S50 ((c) and (d)), the morphology is not well retained after sample preparation.

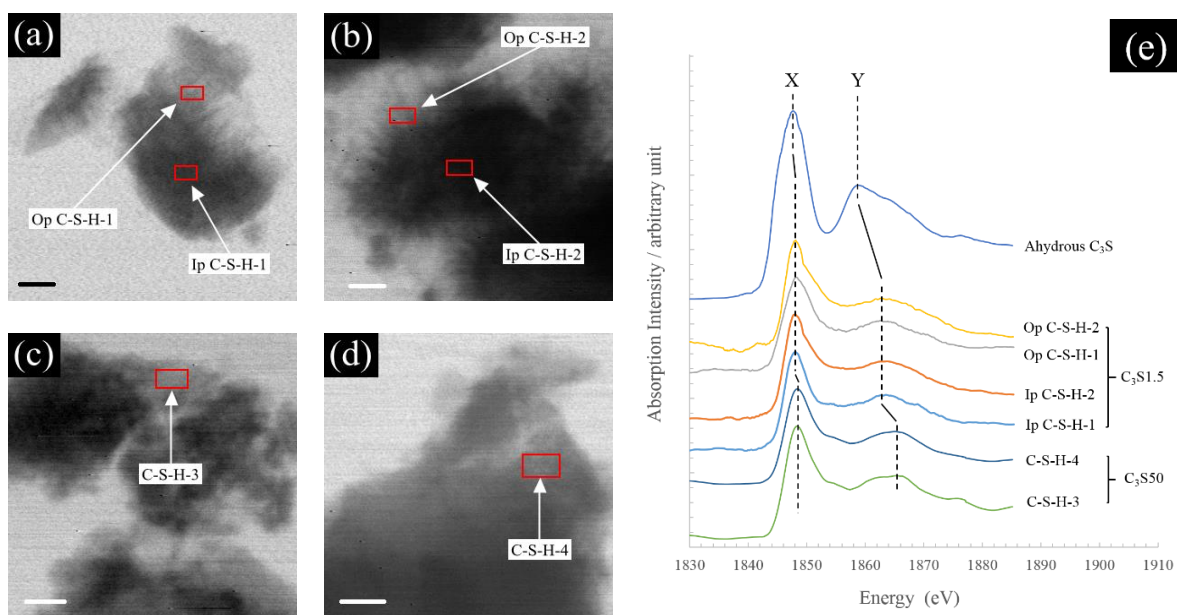


Figure 7.6 Si *K*-edge, scale bar length 1 μm : (a) (b) absorption image of $\text{C}_3\text{S}_{1.5}$; (c) (d) absorption image of C_3S_{50} ; (e) NEXAFS spectra of various locations.

Absorption at Si *K*-edge has only a single absorption edge with no splitting. A designation of the major peak as X and the minor peak as Y in Figure 7.6(e) is given. The major peak is due to excitation from 1s orbital to 3p orbital and minor peaks are due to multi-scattering phenomena^{23,24}. Both peaks shift to higher energy along with the hydration process. Li et al.²³ reported that major peak X shifts to higher energy when the degree of polymerization increases, which is in good agreement with the results of this study. Peak X of C-S-H gel in 1.5-year-old sample locates at 1848.1 eV, 0.4 eV higher than that of anhydrous C_3S . At 50 years, it changes to 1848.3 eV. As the degree of polymerization increases, energy level of Si 1s orbital decreases, which increasing the excitation energy. Note that the change is not high, suggesting that Si is always in 4-fold tetrahedron coordination in C_3S hydration system.

The minor peak Y also increases with hydration at a higher rate compared to that of peak X, so that the energy difference, ΔE , between peak X and Y increases. As shown in Table 7.4 the hydration reaction increases ΔE from 11.2 eV (C_3S) up to 12.8~13.0 eV (1.5-year-old), and eventually to 16.5 eV at later age (50-year-old), indicating significant alternation in multi-scattering behavior around Si atoms. According to the NMR study, the MCL is about 4.2, compared with ~3.5 at 1.5 year. The multi-scattering phenomenon is affected by the closest several neighboring atoms, and seems fairly sensitive to the degree of polymerization. An increase in the MCL increases by 0.7 results in an increase in the ΔE 3.5 eV. It is not fully understood how the atomic structure changes the multi-scattering behavior. More work is worth doing if this linear relationship holds for various hydration age of C-S-H. Future research will focus on the multi-scattering behavior, and how it is related to the atomic structure, especially the SiO_4^{4-} linkage of C-S-H.

Table 7.4 Energy difference ΔE , between minor and major peak at Si *K*-edge.

Sample	X(eV)	Y(eV)	ΔE (eV)	Hydration time (years)
C ₃ S	1847.7	1858.9	11.2	0
Ip C-S-H-1	1848.1	1860.9	12.8	1.5
C ₃ S1.5	1848.1	1860.9	12.8	1.5
Op C-S-H-1	1848.1	1861.1	13.0	1.5
Op C-S-H-2	1848.1	1861.1	13.0	1.5
C ₃ S50	1848.3	1864.8	16.5	50
C-S-H-3	1848.3	1864.8	16.5	50
C-S-H-4	1848.3	1864.8	16.5	50

C *K*-edge

To complement the carbonation study of C₃S50, the NEXAFS spectra of Carbon at *K*-edge was investigated, as shown in Figure 7.7 (a). A line scan was conducted crossing the border of a gel cluster, as marked by the red arrow. The absorption spectrum of each pixel on the arrow was recorded by line scan. Spectra of a thin area at location *b* and a slightly thicker area at location *a* were shown in Figure 7.7 (b). If the sample were significantly carbonated, two distinguishable peaks would be expected near 285.0 eV and 290.0 eV²⁵. On the contrary, the spectra of both location *a* and *b* exhibit no obvious peak near 285.0 eV and only a weak peak at 290.2 eV, whose intensity is of the same order as the noise of the spectra. Comparing with the unambiguous peaks of carbonated C-S-H gel²⁵, it could be concluded that the sample contains negligible amount of carbon, in agreement with NMR and XRD.

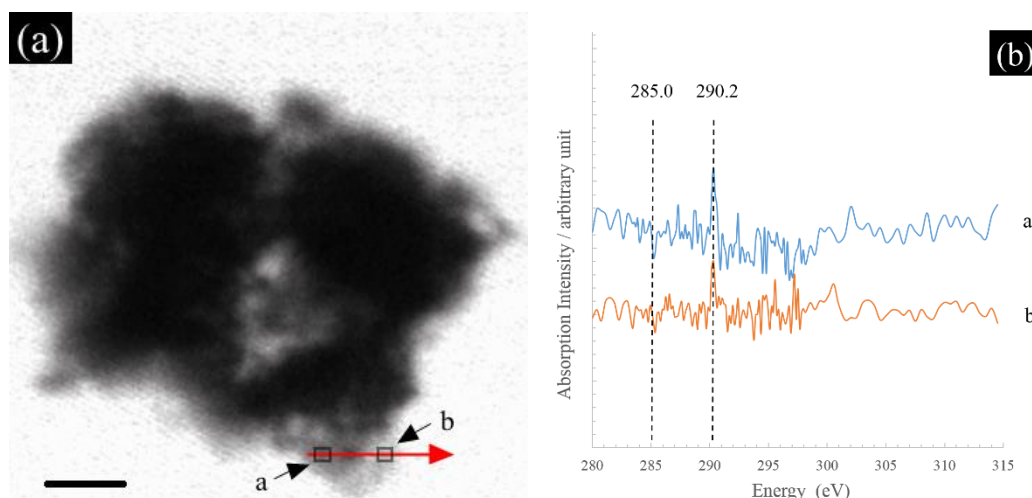


Figure 7.7 C *K*-edge, scale bar length 1 μm : (a) absorption image, red arrow indicates the route of line scan; (b) NEXAFS spectra of location *a* and *b* on the scan route.

7.6 Discussions

Results obtained from both XRD and NMR studies indicate that the 50-year-old paste has not been altered by carbonation. No peak seen on either the diffraction spectra or the ^{29}Si NMR spectrum can be assigned to CaCO_3 . From the chemical composition point of view, the sample is merely a mixture of C-S-H, CH with negligible amount of unreacted C_3S . NEXAFS spectra of carbon *K*-edge support this conclusion, as no specific absorption of carbon atom was observed.

In XRD results, only one broad peak is assigned to C-S-H in this study. Compared with previous research on calcium silicate hydrate crystals¹⁶ and synthesized C-S-H (I)¹⁰, the hydration products (both Ip and Op) remain disordered along all three-crystal axes, even after 50 years curing. Meanwhile the MCL remains below 5, despite almost full hydration. This indicates that at ambient temperature and pressure, the poorly crystalline nature of C-S-H gel almost remains unchanged throughout concrete's typical service life.

Many researchers have discussed atomic models of C-S-H gel, most starting with the structures of tobermorite or jennite¹⁶. The amorphous nature is accounted by the omission of bridging tetrahedrons and the variation of interlayer Ca and water. However, no direct evidence was previously given as to which structure fits C-S-H gel better. In this study, an important clue was found in the NEXAFS spectra.

As shown in Figure 7.5 and Table 7.3, C-S-H falls into the category of aragonite and gypsum, where the coordination structure of Ca is in poor symmetry. As shown in Figure 7.8, the coordination structure of Ca is 7-fold in tobermorite and 6-fold in jennite. The latter has an octahedral symmetry, as is found for Ca in CH and calcite. If the modeling of C-S-H gel starts with jennite, it should be expected that its NEXAFS spectra is analogous to CH and calcite. The NEXAFS spectra of Al-tobermorite were validated by Jackson et al.²⁶, exhibiting minor peaks that are less intensive and less distinguishable. Therefore, the Ca coordination in atomic structure of C-S-H in this sample can be better described by tobermorite structure rather than jennite structure. This is the first time NEXAFS spectra is applied to demonstrating that at atomic scale C-S-H resembles more of tobermorite structure where Ca atom has irregularity in its symmetry. As reported herein, this is important evidence unraveling the structural information of C-S-H, since the relation between coordination symmetry and NEXAFS has been proved by both theory and experimental results of many other chemicals^{27,18,21}.

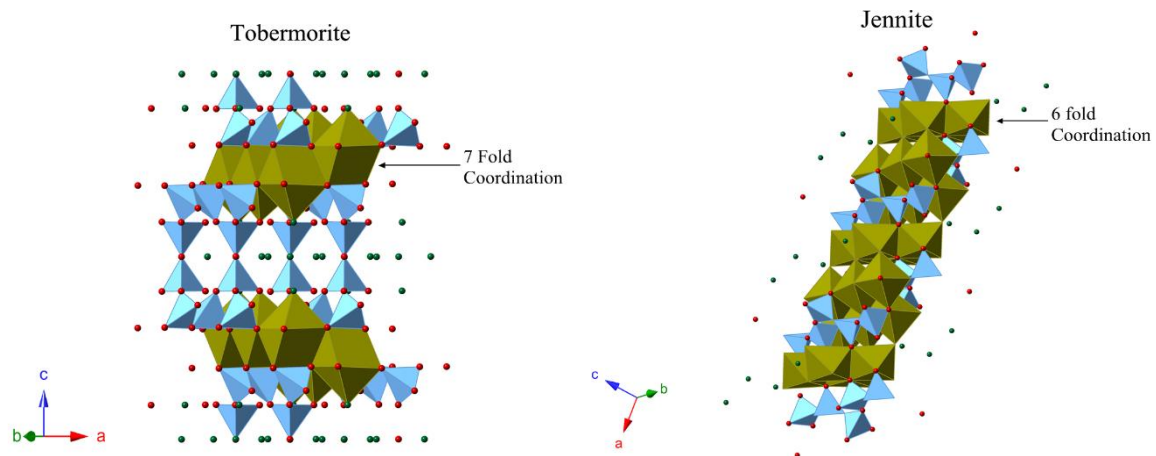


Figure 7.8 Atomic structure of 11Å-Tobermorite and Jennite

The tobermorite model has a limitation in explaining the Ca/Si ratio of C-S-H. Richardson 5 demonstrated in his model that Ca/Si ratio of tobermorite can be largely increased by a variation in the degree of protonation or by Ca replacing the bridging SiO_4^{4-} tetrahedron. These bridging Ca ions also contribute to NEXAFS spectra; therefore they must also be in poorly symmetric coordination, for example the 7-fold irregular symmetry as seen in the intralayer Ca sheets in tobermorite (Figure 7.9). Due to the same reason, “tobermorite- $\text{Ca}(\text{OH})_2$ solid solution” model seems questionable, since the octahedral coordinated Ca atoms in $\text{Ca}(\text{OH})_2$ would yield a strong peak-splitting, which is not the case for C-S-H.

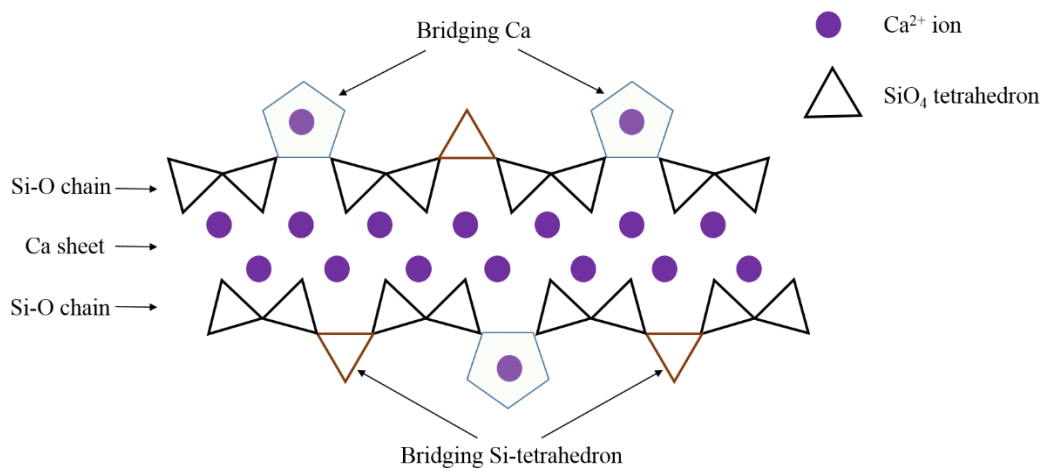


Figure 7.9 Scheme of short chain in tobermorite-based C-S-H

Previous research results using SAXS (small angle x-ray scattering)²⁸ and SANS (small angle neutron scattering)²⁹ strongly indicate that there exists two successive levels of organization in C-S-H gel (Ip and Op) of OPC. At atomic level (<5nm), disordered Si chains, Ca sheets and water layers form nano particles. Jennings⁶ claims this particle to be

globular particle of about 5 nm. In contrast, Richardson's results⁵ indicate it to be long thin fibers of 2.5-3.5 nm thick and tens of nanometers long. It should be clarified that Richardson's observations quoted here focuses on the fibrillar Op C-S-H of pure C₃S paste, while Jennings' results are based on homogenized information of various types of C-S-H paste. Despite the shape of the particles, they are the "building blocks" of C-S-H. At a coarse level (5-200nm), the fine particles form the microstructure of C-S-H. Using pure C₃S paste as an example, the Op C-S-H fibers are formed by the alignment of the long-thin particles along their longitudinal direction. The featureless microstructure of Op C-S-H in C₃S paste can be described by the packing of globular particles (several nanometers large). Given the fact that the C₃S in this study comes from different source compared to Richardson's work, and that the age is also different, it can be concluded that these long-thin particles are naturally the basic building blocks of fibrillar Op C-S-H in C₃S paste. The dimension of these particles and the way they are aligned do not change during the hydration process. The thickening of the Op C-S-H fibers is accomplished by more long-thin particles aligning on the fiber, rather than thickening of the particles. However, these particles can alter significantly when the contents of Ca²⁺ and Al³⁺ increase in the reaction system. Increasing amounts of mineral admixture (fly ash, slag, natural pozzolan, silica fume, and so on) are now used as supplementary cementitious material. It is thus critical to understand the mechanism of how SiO₄⁴⁻ tetrahedron and Ca²⁺ form the fine particles and why these particles keep a constant size during the hydration, and the mechanism how the addition of Ca²⁺ and Al³⁺ favors the formation of globular particles rather than long-thin particles in pure C₃S paste.

7.7 Conclusion

A multi-scale analysis was conducted that compared the structure of a late-age C₃S paste to similar paste at earlier age. No evidence of carbonation was observed in the 50-year-old sample; unreacted C₃S was also rare. The atomic structure of the late-age C-S-H gel can be described as repeated units of SiO₄⁴⁻ tetrahedron, CaO_x polyhedron and H₂O molecules. Even after 50 years of hydration, the structure was still ordered only at short length. The coordination state of Ca²⁺ has irregular symmetry, rather than octahedral symmetry. Since Ca²⁺ in tobermorite shows 7-fold irregular symmetry compared to jennite that has an octahedral symmetry, the short-range atomic scale of the samples is more an analogy to that of tobermorite rather than jennite. The MCL increased along with degree of hydration, from ~3.5 at 1.5 years to 4.18 at 50 years. It is possible that the bridging SiO₄⁴⁻ tetrahedron is replaced by bridging Ca²⁺ at multi locations, which explains both the short chain length and Ca/Si ratio. The bridging Ca²⁺ is also in non-octahedral symmetry, as indicated by Ca L_{3,2}-edge NEXAFS. In Si K-edge, major peak shifts to higher energy with increasing MCL, and so does the minor peak.

At nano scale, Ip C-S-H is featureless and seems to be the flocculation of globular particles. In contrast, Op C-S-H showed clear radial growing fashion, rooting on surface of Ip-Op boundary. Thickness of Op C-S-H fibers increase along with hydration, from several tens of nanometers, to ~100 nm at 8 years and eventually to ~200 nm at 50 years. The fiber was

composed, at a finer scale, of thin fibrillar particles (1.5-2 nm thick and several tens of nanometers long). These particles are the basic building blocks of Op fibers and tend to align along longitudinal direction. Between the fibrillar particles there exist layers of empty space with thickness of about 1.5 nm, which could be filled with water before sample was dried out. Considering such a narrow space, they are most probably physically absorbed water. The growth of Op fibers is accomplished by more particles aligned on the fibers, instead of the thickening of the particles themselves.

7.8 References

1. Bergold, S.T., Goetz-Neunhoeffler, F. & Neubauer, J. Quantitative analysis of C–S–H in hydrating alite pastes by in-situ XRD. *Cem. Con. Res.* **53**, 119-126 (2013).
2. Courtial, M., De Noirfontaine, M-N., Dunstetter, F., Gasecki, G. & Signes-Frehel, M. Polymorphism of tricalcium silicate in Portland cement: a fast visual identification of structure and superstructure. *Powder Diffraction*, **18**, 7-15 (2003).
3. Taylor, R., Richardson, I.G. & Brydson R.M.D. Composition and microstructure of 20-year-old ordinary Portland cement–ground granulated blast-furnace slag blends containing 0 to 100% slag. *Cem. Con. Res.* **40**, 971-983 (2010).
4. Thomas, J.J., Chen J.J., Jennings, H.M. & Neumann, D.A. Ca-OH bonding in the C-S-H gel phase of tricalcium silicate and white portland cement pastes measured by inelastic neutron scattering. *Chem. Mat*, **15**, 3813-3817 (2003).
5. Richardson, I.G. Tobermorite/jennite-and tobermorite/calcium hydroxide-based models for the structure of C-S-H: applicability to hardened pastes of tricalcium silicate, β -dicalcium silicate, Portland cement, and blends of Portland cement with blast-furnace slag, metakaolin, or silica fume. *Cem. Con. Res.* **34.9** (2004): 1733-1777.
6. Jennings, H.M. Refinements to colloid model of C-S-H in cement: CM-II. *Cem. Con. Res.* **38**, 275-289 (2008).
7. Constantinides, G. & Ulm, F.-J. The nanogranular nature of C–S–H. *J. Mech. Phy. Solids*, **55**, 64-90 (2007).
8. Scrivener, K.L. Backscattered electron imaging of cementitious microstructures: understanding and quantification. *Cem. Con. Res.* **26**, 935-945 (2004).
9. Groves, G.W. TEM studies of cement hydration. *MRS proceedings.* **85**, (Cambridge University Press, 1986).
10. Taylor, H.F.W. *Cement chemistry* (Thomas Telford, 1997).
11. Lippmaa, E., Mägi, M., Tarmak, M., Wieker, W. & Grimmer, A.R. A high resolution ^{29}Si NMR study of the hydration of tricalciumsilicate. *Cem. Con. Res.* **12**, 597-602 (1982).

12. Groves, G.W., Brough, A., Richardson, I.G. & Dobson, C.M. Progressive Changes in the Structure of Hardened C₃S Cement Pastes due to Carbonation. *J. Am. Ceram. Soc.* **74**, 2891-2896 (1991).
13. Rodger, S.A., Groves, G.W., Clayden, N.J. & Dobson, C.M. Hydration of Tricalcium Silicate Followed by ²⁹Si NMR with Cross-Polarization. *J. Am. Ceram. Soc.* **71**, 91-96 (1988).
14. Taylor, H., *et al.* The hydration of tricalcium silicate, *Materials and Structures.* **17**, 457-468 (1984).
15. Jennings, H.M. A model for the microstructure of calcium silicate hydrate in cement paste. *Cem. Con. Res.* **30**, 101-116 (2000).
16. Richardson, I.G. The calcium silicate hydrates. *Cem. Con. Res.* **38**, 137-158 (2008).
17. Chae, S.R., Moon, J., Yoon, S., Bae, S., Levitz, P., Winarski, R. & Monteiro, P.J.M. Advanced nanoscale characterization of cement based materials using x-ray synchrotron radiation: a review. *Int. J. Con. Struct. Mat.* **7**, 95-110 (2013).
18. Fleet, M.E. & Liu, X. Calcium L_{2, 3}-edge XANES of carbonates, carbonate apatite, and oldhamite (CaS). *Am. Mineral.* **94**, 1235-1241 (2009).
19. Bae, S. *Synchrotron X-ray Spectro-microscopy and Micro-diffraction Study on the Hydration of Tricalcium Silicate including High-Volume Fly Ash* (Dissertation, University of California Berkeley, 2014).
20. Ha, J., Chae, S., Chou, K.W., Tyliczszak, T. & Monteiro, P.J.M. Scanning Transmission X-Ray Microscopic Study of Carbonated Calcium Silicate Hydrate. *Transport. Res. Rec.* **2142**, 83-88 (2010).
21. Hanhan, S., Smith, A.M., Obst, M. & Hitchcock, A.P. Optimization of analysis of soft X-ray spectromicroscopy at the Ca 2p edge. *J. Elect. Spect. Related Phen.* **173**, 44-49 (2009).
22. Ha, J., Chae, S., Chou, K.W., Tyliczszak, T. & Monteiro, P.J.M. Effect of polymers on the nanostructure and on the carbonation of calcium silicate hydrates: a scanning transmission X-ray microscopy study. *J. Mater. Sci.* **47**, 976-989 (2012).
23. Li, D., *et al.* Silicon K-edge XANES spectra of silicate minerals." *Phy. Chem. Mineral.* **22**, 115-122 (1995).
24. Li, D., Bancroft, G.M., Kasrai, M., Fleet, M.E., Secco, R.A., Feng, X.H., Tan, K.H. & Yang, B.X. X-ray absorption spectroscopy of silicon dioxide (SiO₂) polymorphs: The structural characterization of opal. *Am. Mineral.* **79**, 622-632 (1994).
25. Monteiro, P.J.M., Clodic, L., Battocchio, F., Kanitpanyacharoen, W., Chae, S.R., Ha, J. & Wenk, H.-R. Incorporating carbon sequestration materials in civil infrastructure: A micro and nano-structural analysis. *Cem. Con. Res.* **40**, 14-20 (2013).

26. Jackson, M.D., Chae S.R., Mulcahy, S.R., Meral, C., Taylor, R. & Li P. Unlocking the secrets of Al-tobermorite in Roman seawater concrete. *Am. Mineral.* **98**, 1669-1687 (2013).
27. Naftel, S.J., Sham, T.K., Yiu, Y.M. & Yates, B.W. Calcium L-edge XANES study of some calcium compounds. *J. Syn. Rad.* **8**, 255-257 (2001).
28. Sebastien, B., Chae, R.S., Bihannic, I., Michot, L., Guttman, P., Thieme, J., Schneider, G., Monteiro, P.J.M & Levitz, P. Morphological quantification of hierarchical geomaterials by X-ray nano-CT bridges the gap from nano to micro length scales. *Am. Mineral.* **97**, 480-483 (2012).
29. Allen A.J., Thomas, J.J. & Jennings, H.M. Composition and density of nanoscale calcium–silicate–hydrate in cement. *Nat. Mat.* **6**, 311-316 (2007).

8. Concluding remarks

In this thesis, a suite of synchrotron-radiation-based methods were utilized to study 1) the hydration chemistry of C_3A in the presence of gypsum, 2) the structure-mechanical property correlation of C-(A-)S-H, and 3) the chemistry and microstructure of a 50-year-old C_3S hydration pastes. These topic are critical to the early-age, mature-age and late-age performance of PC concrete, respectively. Apart from the detailed results and discussions in chapter 4-7, herein the most significant conclusions are summarized.

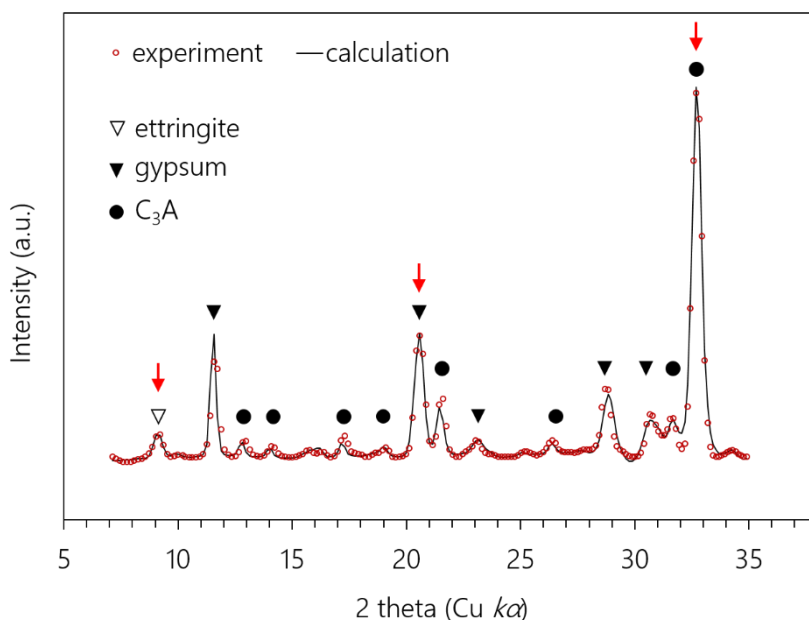
1. The long-standing hypothesis, that gypsum retards C_3A hydration by forming a diffusion barrier on the C_3A surface, is clearly disproved. Ettringite is the only stable hydrate of C_3A in the induction period inh the presence of gypsum. Ettringite needles nucleate heterogeneously on C_3A , and its length is very much limited by the local ion concentration. The ettringite product layer is highly porous.
2. The bulk modulus of pore-free C-S-H solid ranges from ~58 to ~80 GPa, increases with the densification of the layer structure, and decreases with the increase in the interlayer spacing. Contrary to the most computational simulation, the crystallinity defects, such as bridging site SiO_4 vacancies, do not change the stiffness along the *a* and *b* direction. Al-induced crosslinking also increases the bulk modulus of C-A-S-H. Validating the interlayer spacing and crosslinking conditions is critical to build realistic simulation models of C-(A-)S-H.
3. Even after 50 years curing, the C-S-H gel from hydration of C_3S remains highly amorphous, and the MCL of the dreierketten chain is below 5. The crystallization and polymerization processes are negligible beyond the initial several months of hydration. Evidence from the Ca $L_{2,3}$ -edge X-ray absorption indicates that the C-S-H resembles the molecular configuration of tobermorite.

A few suggestions for future studies can be readily made, based on the existing conclusions. 1) Since diffusion barrier hypothesis is disproved for C_3A hydration, more evidence is needed to validate another hypothesis that the active dissolution site on C_3A surface is blocked by sulfate. Surface chemistry experiments should be conducted on fresh C_3A surface that is in contact with gypsum solution for very short period of time (<1 second), so that the complexation structure of Ca^{2+} and SO_4^{2-} on C_3A surface can be detected without being shadowed by large quantities of hydration products. 2) The densification of the C-(A-)S-H interlayer spacing is proven to the dominant to the overall bulk modulus. More HP-XRD needs to be conducted to verify the influence of conditions that change the interlayer spacing, for example the drying history and intercalated polymers.

9. Appendix

For the better organizing purpose, some details of calculation/analysis algorithm and/or software settings are summarized here in the appendix, instead of in the main text.

In-situ wide angle X-ray scattering (WAXS). Rietveld refinement of mass percentage was conducted for WAXS data at 120 min hydration, using reported atomistic structural files of ettringite¹, gypsum² and C₃A³ (Appendix Figure 1). The *MAUD* package was used for the refinement, where all phases were defined as isotropic macro-crystals with micro-strain fitted to match the observed peak width.⁴ For all other WAXS results (from 2 to 110 min), the mass percentage of each phase was estimated by linear proportioning of the intensity of the strongest diffraction peak (red arrows in Appendix Figure 1), with respect to the relevant peak in 120 min results.



Appendix Figure 1 Rietveld refinement of in-situ WAXS data at 120 min hydration. The mass percentages of individual phases were fit for 120 min hydration, and were then estimated, at other hydration time, by linear proportioning of the intensities of the strongest diffraction peaks (red arrows), with respect to the relevant peaks at 120 min.

Small angle scattering (SAS) calculation algorithm. Theoretical calculation of SAS from 2D transmission image has been proven useful to yield quantitative morphological information.⁵ For a transmission image with intensity P at the point (x, y) , the attenuation U is⁶:

$$U(x, y) = -\ln[P(x, y)/P_0] = \int_{-\infty}^{+\infty} \mu(x, y, z) dz \quad (9-1)$$

where P_0 is the intensity of the background, and μ is the attenuation coefficient. Taking the Fourier transform of U gives:

$$FT[U](q_x, q_y) = \int_{-\infty}^{+\infty} \int_{-\infty}^{+\infty} [\int_{-\infty}^{+\infty} \mu(x, y, z) dz] \exp(-i[q_x x + q_y y]) dx dy \quad (9-2)$$

On the other hand the small angle scattering spectrum I is:

$$I(\mathbf{q}) = \frac{1}{V_0} |A(\mathbf{q})|^2 \text{ with } A(\mathbf{q}) = \iiint \rho(\mathbf{r}) \exp(-i\mathbf{q}\mathbf{r}). \quad (9-3)$$

with \mathbf{q} being the scattering vector and ρ the density of scattering objects. Assuming that $\mu(x, y, z) = K \rho(x, y, z)$ with K a constant,

$$A(q_x, q_y, q_z = 0) = K \cdot FT[U](q_x, q_y) \quad (9-4)$$

Considering an isotropic material, $\rho(\mathbf{r}) = \rho(r)$ with $r = |\mathbf{r}|$, hence:

$$A(\mathbf{q}) = A(q) = K \cdot FT[U](q) \left(= \frac{K}{2\pi} \int_0^{2\pi} FT[U](q \cos\theta, q \sin\theta) d\theta \right) \quad (9-5)$$

And therefore:

$$I(q) = \frac{1}{V_0} K^2 |FT[U](q)|^2 = \frac{1}{V_0} K^2 |FT[-\ln[P/P_0]](q)|^2 \quad (9-6)$$

This algorithm is embedded in *ImageJ*TM as a plug-in.

Guinier-Porod model for SAS of rod/cylinder agglomeration.

Guinier and Porod analyses of SAS data yield good estimates of particle size. this work follows a recently proposed Guinier-Porod model which considers contributions from a low- q Guinier region, an intermediate- q Guinier region and a linear Porod region. Adjacent two regions intersect at successive at q_2 and q_1 , respectively⁷.

$$\begin{aligned} I(q) &= \frac{G_2}{q^{s_2}} \exp\left(\frac{-q^2 R_{g2}^2}{3-s_2}\right) & \text{for } q \leq q_2 \\ I(q) &= \frac{G_1}{q^{s_1}} \exp\left(\frac{-q^2 R_{g1}^2}{3-s_1}\right) & \text{for } q_2 \leq q \leq q_1 \\ I(q) &= \frac{D}{q^a} & \text{for } q \geq q_1 \end{aligned} \quad (9-7)$$

where q is the scattering variable; $I(q)$ is the scattered intensity; R_{g1} and R_{g2} are the radii of gyration for the short and overall size of the scattering object. The parameters s_1 and s_2

helps to model nonspherical objects and d is the Porod exponent. G_1 and G_2 are the Guinier scale factors of intermediate- q and low- q region, respectively; D is the scale factor of the Porod region. To guarantee zero and first order continuity at q_1 and q_2 , following equations hold.

$$\begin{aligned}
 q_2 &= [(s_1 - s_2) / (\frac{2}{3-s_2} R_{g_2}^2 - \frac{2}{3-s_1} R_{g_1}^2)]^{0.5} \\
 q_1 &= \frac{1}{R_{g_1}} \left[\frac{(d-s_1)(3-s_1)}{2} \right]^{0.5} \\
 D &= \frac{G_1}{R_{g_1}^{(d-s_1)}} \exp\left[\frac{-(d-s_1)}{2} \right] \left[\frac{(d-s_1)(3-s_1)}{2} \right]^{(d-s_1)/2} \quad (9-8) \\
 G_2 &= G_1 \exp\left[-q_2^2 / \left(\frac{R_{g_1}^2}{3-s_1} - \frac{R_{g_2}^2}{3-s_2} \right) \right] q_2^{2(s_2-s_1)}
 \end{aligned}$$

In case of cylindrical scattering object with radius r and length l , following equation holds.

$$\begin{aligned}
 R_{g_2} &= \left(\frac{l^2}{12} + \frac{r^2}{2} \right)^{0.5} \\
 R_{g_1} &= \left(\frac{r^2}{2} \right)^{0.5} \quad (7-9)
 \end{aligned}$$

$$s_2 = 0 \text{ and } s_1 = 1$$

Eq. (9-8) can be rewritten as

$$\begin{aligned}
 q_2 &= \left[\frac{2}{3} \left(\frac{l^2}{12} + \frac{r^2}{2} \right) - \left(\frac{r^2}{2} \right) \right]^{-0.5} \\
 q_1 &= \left(\frac{2(d-1)}{r^2} \right)^{0.5} \quad (7-10)
 \end{aligned}$$

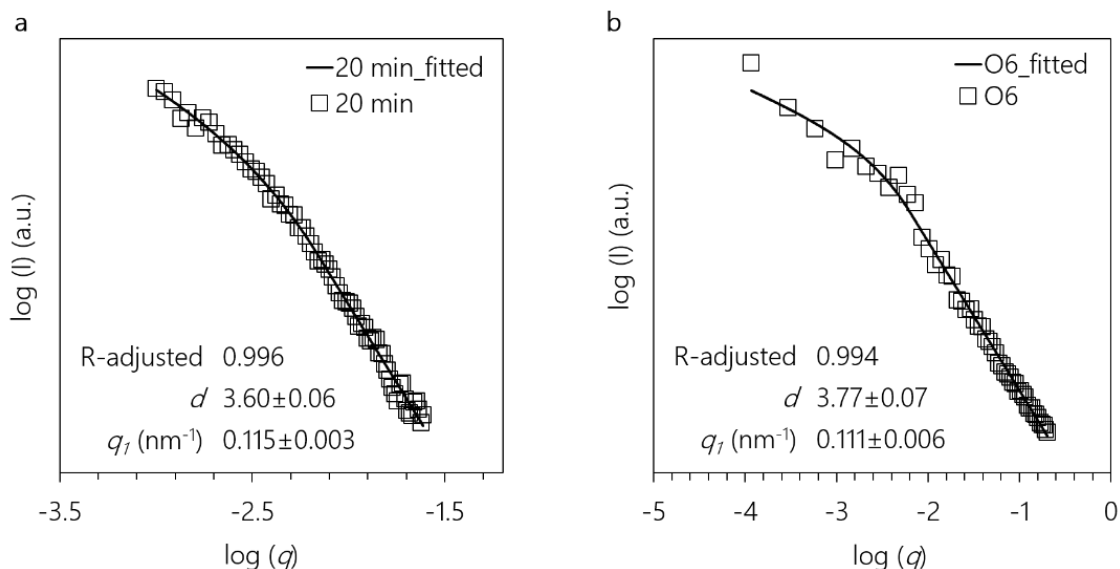
from which r and l can be calculated as

$$\begin{aligned}
 r &= \frac{\sqrt{2(d-1)}}{q_1} \\
 l &= \left[6 \left(\frac{3}{q_2^2} + \frac{d-1}{q_1^2} \right) \right]^{0.5} \quad (9-11)
 \end{aligned}$$

The above equations assume the situation of isometric cylinders/rods agglomeration. With q_1 and q_2 being reliably fitted, r and l can be reasonably estimated.

In the current work, both measured and calculated SAS has limited extension at low- q region, which limits the fitting of q_2 and thus l . Only the linear high- q region and the exponential region between q_1 and q_2 are identified. Least square fitting were conducted

on q_1 , l and G_l with commercial software (*OriginPro 9*, OriginLab Corporation). Examples of 20 min *in-situ* SAXS and calculated SAS from ptychographic image region O6 are shown in Appendix Figure 2.



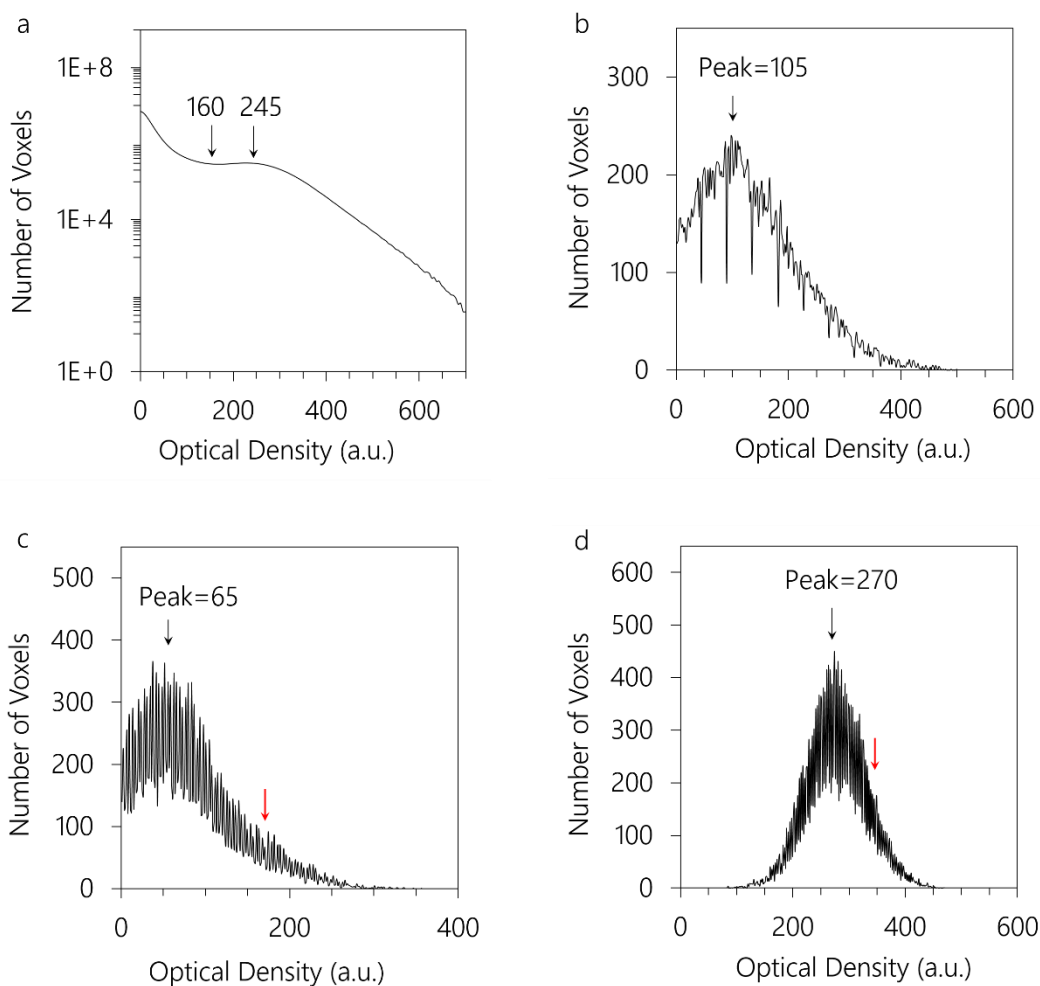
Appendix Figure 2 Least square model fitting of d and q_1 . Examples of a, 20 min in-situ SAXS and b, calculated SAS from ptychographic image region O6.

Reconstruction and analysis of 3D TXM data.

To overcome the limitation of the conventional approaches, which typically depend on fiducial markers or the cross-correlation between sequential projections⁸, an iterative method with intensity-base automatic registration is adopted here, which is able to align the tilt series at sub-pixel resolution. First, the tilt series were roughly registered using alignment features, which were positioned at the common rotation axis with a resolution of a few pixels. Then, the reference images for the fine registration were generated from the computed 2D projections of the reconstructed 3D volume with rough alignments. The second alignment were performed with intensity-based automatic image registration, which is an iterative process brings the 2D projections of the tomographic tilt series into alignment with the computed 2D projections. The alignment procedures were performed by a commercial software package (MATLAB R2015b, the MathWorks Inc.). All tomographic 3D volume reconstructions were performed by algebraic reconstruction technique (ART) with 20 iterations⁹.

Histograms of the full image and extracted sub-volumes of the reconstructed 3D TXM result are calculated with software *ImageJ*TM (Appendix Figure 3). The reconstructed optical density (OD_{recon}) values displayed here are linearly related to the real OD values through a positive constant. For the purpose of color rendering, the threshold OD_{recon} value differentiating hydration product and unhydrated phase is determined to be 160 (Appendix

Figure 3a). Hydration product has rather continuously distributed OD_{recon} values since, at nano-scale, the porosity and size of hydrates vary in different hydration location. For those precipitating in confined space (V1), the peak OD_{recon} value is 105 and the average is 117.4 (Appendix Figure 3b). Whereas the product on open surface (V2) has peak OD_{recon} value 65 (Appendix Figure 3c). The core region of a remnant C_3A particle (V3) has peak OD_{recon} value at 270 (Appendix Figure 3d), consistent with the hump at 245 in Appendix Figure 3a. For hydration product in confined space (V2, Appendix Figure 3b), small amount of voxels with $OD_{recon}>300$ is observed, which are not observed in Appendix Figure 3c, due to the existence of small quantity of C_3A in V2.



Appendix Figure 3 Histograms of the reconstructed 3D TXM result. a, full image (y-axis plotted with log values). b, sub-volume V1, corresponding to hydration product formed in confined space. c, sub-volume V2, corresponding to hydration product formed on open surface. d, sub-volume V3, corresponding to the core region of remnant C_3A . The x-axis represents the reconstructed optical density value (OD_{recon}) in arbitrary unit, which is

linearly related to the real optical density value (OD). The red arrows in c and d indicate the estimated OD_{recon} values for porosity-free ettringite and C_3A voxels, respectively.

According to attenuation law (eq. (7-12) and (7-13)), the real OD is linearly proportional to sample thickness t by attenuation coefficient μ . A positive constant α links OD with OD_{recon} . The attenuation coefficient μ is linked with the maximum attenuation coefficient μ_{max} by the porosity φ (eq. (7-14)).

$$I = I_0 e^{-\mu t} \quad (9-12)$$

$$OD = \mu t = \ln(I/I_0) \quad (9-13)$$

$$OD_{recon} = \alpha OD = \alpha (1-\varphi) \mu_{max} t \quad (9-14)$$

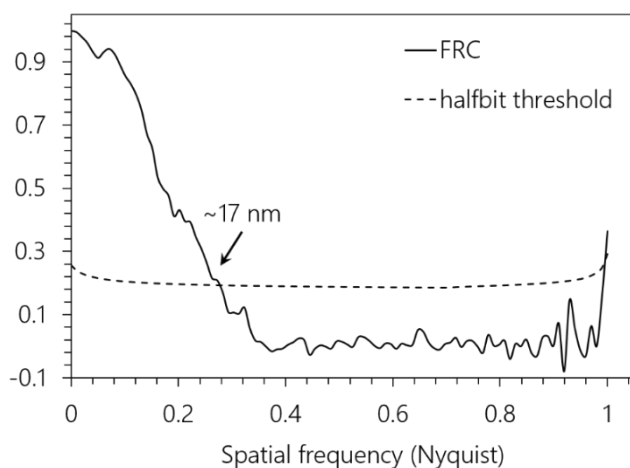
where I_0 and I are the incident and transmitted beam intensities, respectively. Given that α is related to the reconstruction algorithm (constant for all voxels), μ_{max} remains constant for each phase, and t equals to the voxel edge size (10 nm), it's readily seen that the OD_{recon} of a sub-volume is related to its porosity φ through eq. (9-15).

$$\varphi = 1 - OD_{recon_mean} / OD_{recon_max} \quad (9-15)$$

Where OD_{recon_mean} is the average OD_{recon} per pixel of a sub-volume, and OD_{recon_max} is the OD_{recon} of a zero-porosity voxel of the studied phase (i.e. ettringite or C_3A). Determining the exact value of OD_{recon_max} is not applicable here, and therefore the 90% threshold of the accumulated OD_{recon} distribution in V2 and V3 (red arrows in Appendix Figure 3c and 3d) is adopted as the OD_{recon_max} values of ettringite (165) and C_3A (345), respectively. The OD_{recon_mean} of each sub-volume are calculated to be 117.4, 69.2 and 278.8 for sub-volumes V1, V2 and V3, respectively. Using eq. (9-15), the porosities are calculated to be 29% for V1, 58% for V2 and 19% for V3. A positive error of ~10% is estimated, which mainly comes from the uncertainty (~ 50) of estimating the OD_{recon_max} values.

Resolution of ptychographic images estimated by Fourier Ring Correlation (FRC)

The raw diffraction dataset of Figure 4.3c was separated to two individual subsets by selecting every other measurement, and were then reconstructed to two independent 2D images of the same field of view¹⁰. The resolution (~17 nm) was determined by Fourier Ring Correlation of the two images with half-bit threshold¹¹ (Appendix Figure 4). The real resolution is higher than ~17 nm since the signal-to-noise ratio of the image reconstructed with full data set is better than the images from the separated subsets.



Appendix Figure 4 Resolution of the ptychographic image determined by Fourier Ring Correlation and half-bit criterion.

Al *K*-edge XANES peak determination.

For reading convenience, Al *K*-edge XANES of studied compounds (Figure 4.2b) are listed in Supplementary Table 1.

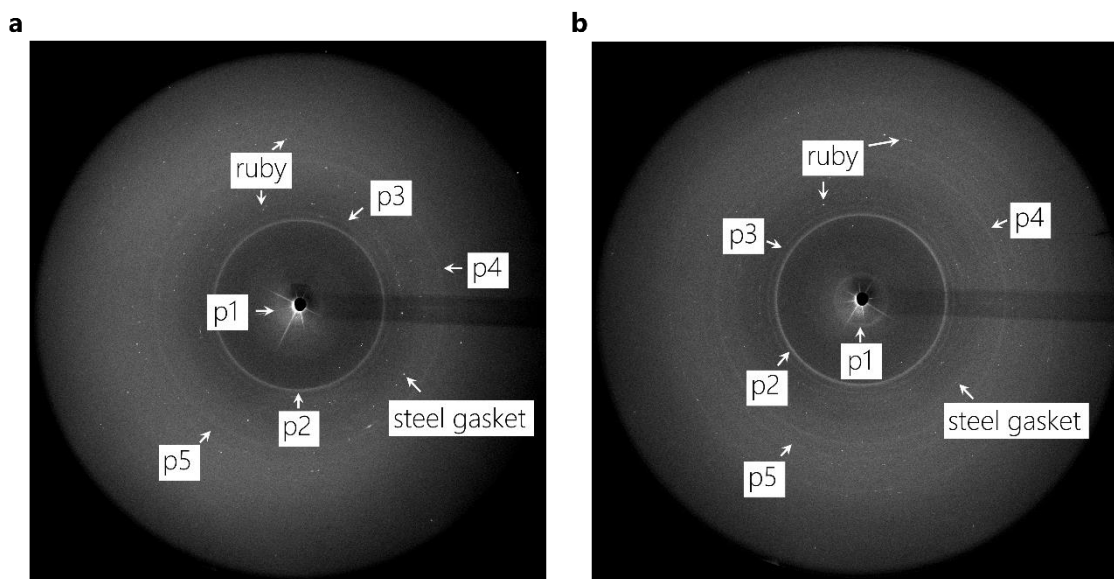
Supplementary Table 1 Al *K*-edge XANES Peak positions of studied compounds determined from Figure 4.2, with unit of eV. The uncertainty is estimated to be 0.3 eV.

	A	C	D	E
C ₃ A	1568.6	1572.5	1579.3	1587.4
ettringite	1569.4	1574.9	-	1585.9
\bar{S} -AFm	1569.4	1574.7	-	1587.0
C ₃ AH ₆	1572.4	1576.0	-	1588.0
C ₄ AH ₁₃ *	1572.0	1575.8	-	1588.2

* Spectra of C₄AH₁₃ is adapted from reported work.¹²

The 2D raw diffraction data of 1.0CSH and 1.3CSH at ambient pressure

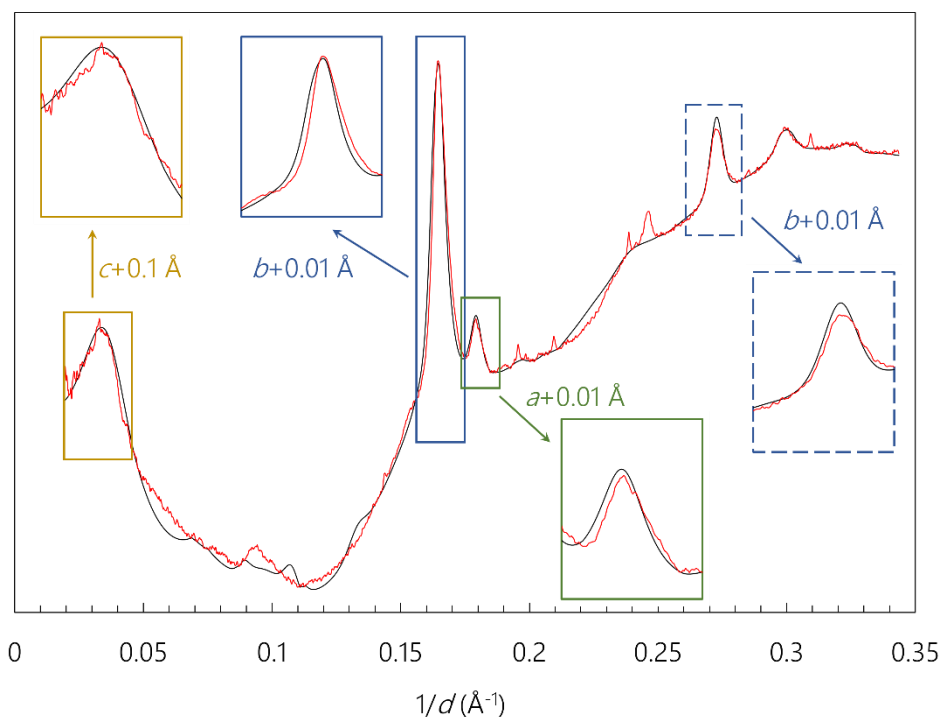
The raw diffraction data of 1.0CSH and 1.3CSH at ambient pressure are shown in, instead in the main text for purpose of conciseness.



Appendix Figure 5 The 2D raw diffraction data of 1.0CSH and 1.3CSH at ambient pressure. Ruby and steel gasket yield multiple diffraction spots, and the arrows only point out a few of them as demonstration. The labelling of the diffraction rings of C-S-H (p1-p5) is consistent with Figure 5.1c.

Determining the uncertainty of lattice parameter refinement

The lattice parameters a , b , and c are refined with the *MAUD* package¹³, using the integrated XRD diffractogram at each pressure. To address the anisotropic crystallite size effect, the “anisotropic – no rules” line broadening models was used, where the crystallite sizes, anisotropic micro-strains and the lattice parameters are readily defined.⁵ The uncertainties of refining a , b , and c are conservatively determined as 0.01 Å, 0.01 Å and 0.1 Å. Changing the lattice parameters by such values results in a noticeable peak shifting, as shown in an example in Appendix Figure 6.



Appendix Figure 6 Determining the uncertainties of refining the lattice parameters. Red and black curves are the calculated and experimental diffractograms, respectively, of 0.8CSH at 2.14 GPa. The insets are the local peak shifting resulting from changes of the lattice parameters as indicated, compared with the best fitting results.

Details of interatomic interactions

The computational strategy used here, aiming to vary Ca/Si systematically and explore resulting properties, is a combination of several classical atomistic simulation techniques. These methods are deployed at different stages of the model preparation. The complex hydrate materials have different types of atoms with varying chemical environments, which is discussed in details in following subsections. These simulations, which have classical nature, are performed using CSH-FF potentials.¹⁵ The main chemical elements in C-S-H are Si, Ca, O and H atoms. These atoms adopt different characteristics depending on their local chemical environments. To appropriately address such variations, classical potentials utilize different labels for a given element to describe these chemical environments. Due to charge compensation, the O-H bonding would be different inside a water molecule and a hydroxyl group. Therefore, for classical simulations using CSH-FF potential, one needs the prior knowledge about the local atomic environments in the molecular structure of material. More specifically, CSH-FF uses nine labels to describe the four types of elements in C-S-H. Our convention for these nine labels is as follows: Ca (intralayer calcium), Cw (interlayer calcium), Si (silicon), Oh (oxygen in hydroxyl group), H (hydrogen in hydroxyl groups), Ob (bridging oxygen in silica chain), Ow (oxygen in water molecules), Hw

(hydrogen in water molecule), O (oxygen other than Ow, Oh and Ob). The partial charges of all species are provided in Supplementary Table 2. The partial charges of all species are constant except oxygen atoms. In fact, the partial charges of oxygen species in calcium-silicate layers are set to vary in order to ensure charge-neutrality within numerical samples. A comprehensive sensitivity analysis on the elastic properties is carefully performed with different charge-balancing schemes. Due to the small charge-imbalance in the samples, charge-neutralization schemes do not strongly affect the elastic properties. In this work, the excess charge is equally distributed among O, Ob and Oh atoms.

Supplementary Table 2 Partial Charges in CSH-FF potential.

Species	Charge	Species	Charge
Si	1.722357	H	0.425
Ca	1.435466	O	[-1.15,-1.26]
Cw	1.705529	Oh	[-0.93,-0.97]
Ow	-0.82	Ob	[-1.01,-1.13]
Hw	0.41		

The CSH-FF interatomic/intermolecular potential is a core-only model for hydrated calcium-silicates, in which atoms are described as interacting points through Columbic and short-range potential functions. The total interatomic potential for CSH-FF potential reads:

$$E_{tot}^{CSHFF} = E_{Col} + E_{lj} + E_{radial} + E_{angular} \quad (9-16)$$

where E_{Col} , E_{lj} , E_{radial} , and $E_{angular}$ are the electrostatic, short-range Van der Waals in the form of Lennard-Jones potential, bond stretching and bond bending contributions to the potential energy, respectively. CSH-FF potential is a customized force field for hydrated calcium-silicates, and it is not transferable to other oxides with different chemical environments. Therefore, CSH-FF can be seen as an improved version of the generic ClayFF potential¹⁶ (originally developed for structural properties of clay minerals) for hydrated calcium-silicates such as cement hydrates. To describe the molecular structure of water and its interaction with other water molecules, both CSH-FF and Clay-FF potential models are built around the flexible SPC model for water.¹⁷ In particular, CSH-FF was designed to reproduce both structural and elastic data of Tobermorite minerals obtained from ab initio calculations.

In order to extend the predictability of the CSH-FF model, the latter was slightly modified to include a couple of new features. Primarily to reduce the computational costs incurred by the calculation of long-range forces using Ewald summation technique, the columbic interactions are calculated using Wolf method.¹⁸ While Ewald summation scales with

$O(N^{3/2})$, Wolf summation scales with $O(N)$. To apply a uniform cut-off radius in the simulation box for both long- and short-range interactions, R_c is set to 12\AA . The Wolf damping factor, η , is set to 0.25 in all simulations. The second modification in the CSH-FF potential pertains to incorporation of hydroxyl groups. The force field parameters for hydroxyl groups are included in the extended form of the CSH-FF potential.

The short-range interactions in CSH-FF and ClayFF force fields are described via Lennard-Jones potential:

$$E_{ij} = 4\epsilon \sum_i \sum_{j>i} \left[\left(\frac{\sigma}{r_{ij}} \right)^{12} - \left(\frac{\sigma}{r_{ij}} \right)^6 \right] \quad (9-17)$$

where σ and ϵ have the dimensions of distance and energy, respectively. These parameters are provided for short-range interactions between pairs of elements in the model. The potential parameters are provided in Supplementary Table 3.

Supplementary Table 3 Lennard-Jones potential parameters used in CSH-FF potential.

spec _i	spec _j	ϵ (kcal/mol)	σ (Å)	spec _i	spec _j	ϵ (kcal/mol)	σ (Å)
O	Ca	8.694E-4	4.365	Oh	Oh	6.180E-2	3.448
Ca	Ob	7.057E-4	5.452	O	Ob	4.543E-2	3.626
Ca	Oh	8.694E-4	4.365	O	Oh	4.543E-2	3.626
O	Cw	1.460E-3	4.365	O	Ob	6.180E-2	3.448
Cw	Ob	1.040E-3	4.446	Ca	Ow	8.760E-4	4.365
Cw	Oh	1.040E-3	4.446	Cw	Ow	6.042E-4	4.472
O	Si	5.604E-4	3.270	O	Ow	5.258E-3	4.241
Si	Ob	5.950E-4	3.261	Ow	Ob	8.717E-1	2.895
Si	Oh	5.950E-4	3.261	Ow	Oh	8.717E-1	2.895
Si	Ow	5.950E-4	3.235	Ow	Ow	1.540E-1	3.163
Ob	Ob	6.180E-02	3.448	O	O	1.243E+0	2.735

Similar to ClayFF potential, the hydrogen species do not have short-range interactions. The radial and angular excursions in water molecules and hydroxyl groups are described via simple harmonic potentials:

$$E_{radial} = \sum_{i=1}^{N_{OH}} \frac{1}{2} k_r (r_{ij} - r_0)^2 \quad (9-18)$$

$$E_{angular} = \sum_{i=1}^{N_{H_2O}} \frac{1}{2} k_\theta (\theta_{ij} - \theta_0)^2 \quad (9-19)$$

where k_r and k_θ are radial and angular stiffness, respectively. Parameters r_0 and θ_0 denote the equilibrium hydroxyl bond length and Hw-Ow-Hw angle in water molecules, respectively. N_{OH} and N_{H_2O} are the total number of O-H bonds in hydroxyl groups and water molecules and total number of water molecules, respectively. The radial and angular constants are provided in the Supplementary Table 4 and 5.

Supplementary Table 4 Radial interaction Constants in CSH-FF potential.

spec _i	spec _j	k_r (Kcal/mol/Å ²)	r_0 (Å)
Hw	Ow	554.13	1
H	Oh	554.135	1

Supplementary Table 5 Angular interaction within water molecules in CSH-FF potential.

spec _i	spec _j	spec _k	k_θ (Kcal/mol/θ ²)	θ_0
Hw	Ow	Hw	45.770	109.47

Initial atom positions for molecular calculation

The initial atom positions for calculation are determined in the following steps:

Step 1, choosing the starting configuration from published tobermorite structure, which are generally classified into three groups according to the basal spacing, i.e. 9.3 Å, 11.3 Å, 14.0 Å tobermorite.⁶⁻¹⁰ We start from tobermorite structures with the best match to the measured crystal-chemical features of the C-S-H samples. The 0.8CSH has basal spacing is ~14.42 Å at ambient pressure, and therefore the 14 Å tobermorite structure was chosen as the starting configuration.¹⁰ Similarly the 9 Å tobermorite structure (basal spacing ~9.57 Å) was used for the 1.3CSH (basal spacing ~9.97 Å at ambient pressure).⁶ The ambient pressure basal spacing of 1.0CSH is ~11.07 Å, close to that of 11 Å tobermorite (~11.24 Å) of both normal and anomalous polymorph.^{8,9} However, the NMR data of 1.0CSH

confirm no dreierketten chain crosslinking, in contrast to these two 11 Å tobermorite structures. Therefore, the 14 Å tobermorite structure is also used as the starting configuration for 0.8CSH.

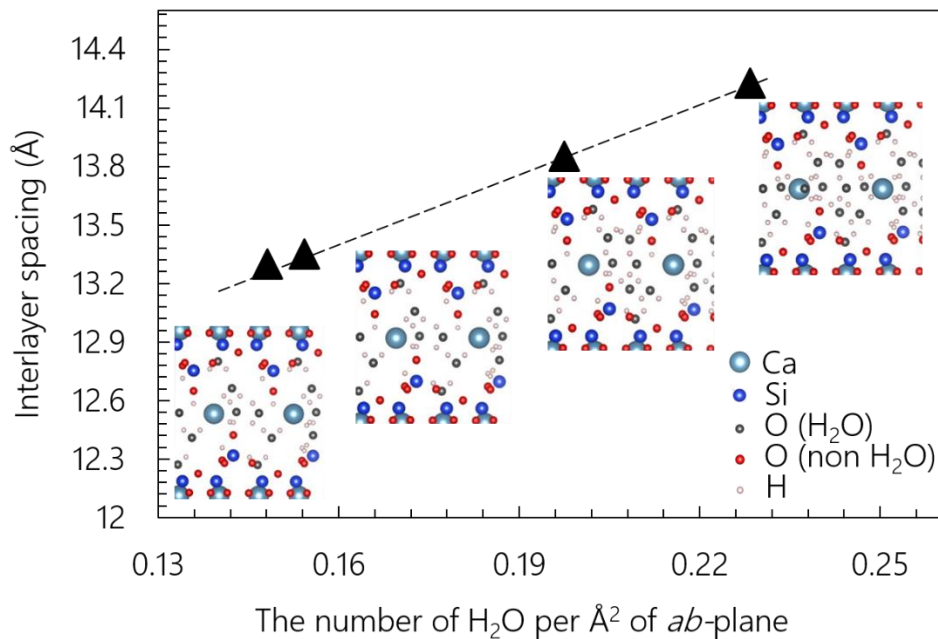
Step 2, modifying the dreierketten chain. To guarantee similar dimensions along each axis, $2 \times 2 \times 1$ supercells were constructed for 0.8CSH and 1.0CSH, and a $2 \times 2 \times 2$ supercell was constructed for 1.3CSH, using the starting configurations determined in step 1. The size of the supercell also enables adjusting the mean dreierketten-chain length (MCL) to the measured values of all samples. The measured MCL are 19, 5 and 2 with increasing Ca/Si.²⁴ For non-crosslinked CSH, the MCL is related to the bridging site omission percentage (α) by equation (5):

$$MCL = (3 - \alpha) / \alpha \quad (9-20)$$

The omission percentages are back-calculated as 15%, 50% and 100% for samples with increasing Ca/Si. Therefore the corresponding amount of bridging site Si was removed in the starting configuration. The vacancies of bridging site are assumed not agglomerating but rather in homogeneous distribution in the models of 0.8CSH and 1.0CSH, as the agglomeration of the same type of defects is proven not energetically favored²⁵. Note that the 1.3CSH has a completely dimeric structure.

Step 3, determining the amount of interlayer contents. The intralayer CaO_7 double sheets were kept unchanged. The existing interlayer Ca atoms in the starting crystal structure of tobermorite were also conserved, and a certain number of extra Ca atoms were placed at a position with biggest distance to existing interlayer Ca, so that the total Ca/Si molar ratios matches the measure bulk Ca/Si ratios.

The conventional thermal gravity data exhibit significant deviations in determining the amount of water in the interlayer of C-S-H.²⁶ Determining the amount of interlayer water requires extra care here, as it strongly correlates with the interlayer spacing.²⁷ It is of major purpose to study the correlation between the mechanical responses of C-S-H with the interlayer spacing. Difference amount of interlayer water is used as input for molecular simulation and, from the relaxed structure, determine the amount of interlayer water that outputs an interlayer spacing within 2% difference from the XRD refined value at ambient pressure.



Appendix Figure 7 GULP relaxed basal spacing of 0.8CSH as a function of the amount of interlayer water molecules per Å² of *ab*-plane per interlayer. The dash line is for eye-guide of the trend.

As shown in Appendix Figure 7, the basal spacing increases linearly with increasing the amount of interlayer water per Å² of *ab*-plane. The 0.23 H₂O / Å² per interlayer is adopted as the value used in the initial structure for 0.8CSH, since the relaxed basal spacing (~14.23 Å) is close enough (within 2% difference) to the XRD measured value (~14.42 Å). No intentional attempt was made to match the exact value from XRD measurement. Similarly, the number density of interlayer water in 1.0CSH is determined to be 0.15 H₂O / Å² per interlayer, and in 1.3CSH to be 0.05 H₂O / Å² per interlayer, corresponding to relaxed basal spacings of ~11.30 Å and ~9.99 Å, respectively. The measured basal spacings are ~11.07 Å for 1.0CSH and ~9.97 Å for 1.3CSH, both within 2% deviation compared with the relaxed model.

Step 4, to balance the sampling size and computation efficiency, 2×2×1 supercells are used for 0.8CSH and 1.0CSH, and 2×2×2 supercell for 1.3CSH (after modification of previous steps) as the starting model of calculation. To insure smooth loading curve, the models undergoes two simulative loading-unloading cycles, up to 8 GPa hydrostatically. The obtained atom positions at 0 GPa are then used as the initial models for simulation. They are listed in Supplementary Table 6-7 in the form of fractional coordinates.

Calculating the pair distribution function (PDF)

A number of different formalisms for PDFs exist in the literature. Keen performed an extensive survey of these and his recommendations are adopted here.²⁸ The calculation of Pair Distribution Functions is in accordance with the theory of Chung and Thorpe.²⁹ It makes use of phonon information calculated within GULP,³⁰ for an optimized structure, using a Monkhorst-Pack grid. Chung and Thorpe state that the probability of finding a pair of atoms i and j , with position \mathbf{r}_i and \mathbf{r}_j respectively, at position \mathbf{r} is given by

$$\rho_{ij}(\mathbf{r}) = \langle \delta(\mathbf{r} - (\mathbf{r}_j - \mathbf{r}_i)) \rangle \quad (9-21)$$

where $\langle \dots \rangle$ is the statistical average implying both configurational and thermal averages. To account for thermal motion, Chung and Thorpe demonstrated that, within the harmonic approximation, the Debye-Waller theorem can be used to justify the use of a series of weighted Gaussian peaks $\rho_{ij}(\mathbf{r})$, centered at \mathbf{r}_{ij} to be the unit vector between atoms i and j , and $\mathbf{u}_{ij} = \mathbf{u}_j - \mathbf{u}_i$, where \mathbf{u}_i is the displacement of atom i . then the width is given by

$$\sigma_{ij} = \langle \mathbf{u}_{ij} \cdot \mathbf{r}_{ij} \rangle \quad (9-22)$$

Therefore, we can express $\rho_{ij}(\mathbf{r})$ as the sum of the Gaussian peaks for each pair in the main unit cell and its periodic images, as follows:

$$\rho_{ij}(r) = \sum_i \sum_j \sum_l \frac{1}{\sqrt{2\pi\sigma_{i_0j_l}^2}} \exp\left[-\frac{|r_{i_0j_l} - r|^2}{2\sigma_{i_0j_l}^2}\right] \quad (9-23)$$

where subscripts 0 and l pertain to the unit cell and its l th periodic image. The pair distribution function is subsequently calculated following:

$$g_{ij}(r) = 4\pi r [\rho_{ij}(r) - \rho_0] \quad (9-24)$$

where ρ_0 is the average number density, $\rho_0 = n/V_{unitcel}$.

Supplementary Table 6 Atom positions of 0.8CSH

$a=13.466 \text{ \AA}, b=14.979 \text{ \AA}, c=28.455 \text{ \AA}, \alpha=90.2^\circ, \beta=87.3^\circ, \gamma=124.3^\circ$			
Name of atoms	X	Y	Z
Ca	0.3685	0.2125	0.2836
Ca	0.36504	0.71231	0.27814
Ca	0.86752	0.21362	0.28566
Ca	0.86342	0.71005	0.28268
Ca	0.27831	0.46108	0.73064
Ca	0.27719	0.95887	0.72716
Ca	0.77587	0.45894	0.72452
Ca	0.77941	0.96263	0.72783
Ca	0.021	0.20982	0.79507
Ca	0.01531	0.70403	0.78908

Ca	0.51716	0.20404	0.79568
Ca	0.51681	0.70918	0.7911
Ca	0.12514	0.46659	0.21848
Ca	0.12138	0.96562	0.22026
Ca	0.62367	0.4651	0.21979
Ca	0.62248	0.96612	0.22327
Ca	0.13614	0.21858	0.21859
Ca	0.1338	0.71893	0.21809
Ca	0.63044	0.21319	0.2244
Ca	0.63394	0.72136	0.21961
Ca	0.03002	0.45821	0.79241
Ca	0.02912	0.95984	0.79242
Ca	0.52959	0.46064	0.79257
Ca	0.52584	0.95792	0.78727
Ca	0.28752	0.2133	0.73004
Ca	0.28429	0.71214	0.72681
Ca	0.7834	0.21111	0.73403
Ca	0.78454	0.71355	0.72776
Ca	0.3759	0.46501	0.2805
Ca	0.37182	0.96366	0.28627
Ca	0.88	0.46692	0.28439
Ca	0.8726	0.9656	0.28898
Si	0.38745	0.19739	0.17851
Si	0.39436	0.70532	0.17208
Si	0.88671	0.20142	0.18077
Si	0.88666	0.70223	0.1763
Si	0.27772	0.44098	0.83684
Si	0.26331	0.93159	0.83331
Si	0.77648	0.4397	0.83015
Si	0.76651	0.94044	0.83293
Si	0.0453	0.19822	0.68856
Si	0.04096	0.69414	0.68464
Si	0.53728	0.19406	0.68792
Si	0.54084	0.70032	0.68634
Si	0.12368	0.44704	0.32459
Si	0.11445	0.94109	0.32538
Si	0.62236	0.44153	0.32737
Si	0.60532	0.93703	0.32976
Si	0.47599	0.38561	0.10679
Si	0.46669	0.89508	0.10066
Si	0.98167	0.38968	0.10564
Si	0.95512	0.88729	0.10422
Si	0.32582	0.10278	0.90902
Si	0.34001	0.62473	0.90506

Si	0.82894	0.11385	0.90996
Si	0.13899	0.38933	0.61486
Si	0.12292	0.8836	0.61606
Si	0.61139	0.38096	0.61411
Si	0.60186	0.87122	0.60271
Si	0.17685	0.62189	0.39888
Si	0.62172	0.0846	0.41134
Si	0.6716	0.62047	0.40087
Si	0.38758	0.49154	0.17379
Si	0.38187	0.98659	0.18001
Si	0.89035	0.49208	0.17237
Si	0.88135	0.99063	0.18225
Si	0.27311	0.22728	0.83744
Si	0.26548	0.72546	0.83294
Si	0.76986	0.2292	0.84068
Si	0.76214	0.73013	0.83422
Si	0.04001	0.48188	0.6842
Si	0.03695	0.98495	0.68667
Si	0.53659	0.48767	0.68592
Si	0.54127	0.98712	0.68039
Si	0.1215	0.23734	0.32645
Si	0.11358	0.73186	0.32646
Si	0.62242	0.23179	0.3296
Si	0.60836	0.72777	0.325
Ob	0.39987	0.26417	0.12994
Ob	0.42847	0.77792	0.12219
Ob	0.90181	0.2745	0.13416
Ob	0.91119	0.76913	0.12568
Ob	0.26158	0.99315	0.88037
Ob	0.29559	0.5057	0.88725
Ob	0.76074	0.00384	0.87951
Oh	0.80817	0.52346	0.87847
Ob	0.0707	0.26962	0.63993
Ob	0.05888	0.76221	0.63581
Ob	0.54648	0.26239	0.63927
Ob	0.55382	0.76651	0.63786
Oh	0.11066	0.00328	0.37626
Ob	0.13196	0.51066	0.37345
Ob	0.57682	0.97763	0.38039
Ob	0.63342	0.50992	0.37478
Ob	0.38748	0.09326	0.15995
Ob	0.38082	0.59248	0.15515
Ob	0.88541	0.09648	0.16177
Ob	0.87819	0.59236	0.159

Ob	0.26668	0.33005	0.85425
Ob	0.25473	0.82325	0.85407
Ob	0.7653	0.33436	0.85256
Ob	0.75925	0.83255	0.85446
Ob	0.0379	0.09025	0.67022
Ob	0.03731	0.5867	0.66817
Ob	0.53884	0.09285	0.66633
Ob	0.53514	0.59237	0.6685
Ob	0.11892	0.34038	0.34269
Ob	0.11003	0.83564	0.34458
Ob	0.61185	0.33219	0.34725
Ob	0.6045	0.82987	0.34559
O	0.49771	0.27143	0.21324
O	0.4986	0.77571	0.20939
O	0.99662	0.27229	0.21574
O	0.99597	0.77424	0.21117
O	0.38517	0.006	0.79914
O	0.39226	0.51668	0.80029
O	0.88867	0.01564	0.79985
O	0.89191	0.51023	0.79327
O	0.14903	0.26694	0.72565
O	0.14953	0.76819	0.71941
O	0.64811	0.26518	0.72232
O	0.65167	0.77315	0.72016
O	0.2352	0.02283	0.29368
O	0.23829	0.52282	0.28765
O	0.72939	0.0254	0.30077
O	0.73666	0.51314	0.28895
O	0.26621	0.15713	0.21098
O	0.26978	0.66675	0.20378
O	0.76376	0.15834	0.21308
O	0.76528	0.66334	0.20891
O	0.16132	0.40527	0.80662
O	0.152	0.89365	0.79987
O	0.66144	0.40525	0.80089
O	0.65581	0.90154	0.79937
O	0.91835	0.15957	0.71739
O	0.91773	0.65678	0.71601
O	0.41693	0.15223	0.72084
O	0.41904	0.65867	0.7194
O	0.00691	0.40759	0.29395
O	0.00138	0.90364	0.29402
O	0.50629	0.40384	0.29524
O	0.49854	0.89991	0.29378

O	0.3308	0.09326	0.96413
Oh	0.31855	0.62477	0.96366
O	0.83584	0.09849	0.9643
Ow	0.86361	0.58389	0.9781
Oh	0.4758	0.37053	0.04826
O	0.45082	0.89442	0.04498
O	0.98252	0.37928	0.04925
O	0.94881	0.89328	0.04849
Ow	0.19313	0.21102	0.48999
Oh	0.15964	0.60331	0.45744
Oh	0.5288	0.06077	0.45824
O	0.64983	0.61893	0.45668
O	0.15609	0.38669	0.55856
Oh	0.12965	0.8857	0.55713
Oh	0.60559	0.37665	0.55579
O	0.56076	0.83583	0.55055
Oh	0.1256	0.46215	0.12566
Oh	0.10796	0.97651	0.11864
Oh	0.61724	0.45287	0.12587
Oh	0.61944	0.99139	0.11023
Oh	0.98108	0.18644	0.88491
Oh	0.03773	0.67681	0.90102
Oh	0.48077	0.17917	0.8852
Oh	0.48755	0.70861	0.88718
Oh	0.27882	0.46826	0.639
Oh	0.26384	0.96478	0.63512
Oh	0.75679	0.45213	0.62876
Oh	0.76064	0.95371	0.60124
Oh	0.36576	0.28302	0.41313
Oh	0.32882	0.71268	0.38762
Oh	0.75335	0.11957	0.4331
Oh	0.82205	0.71725	0.38491
Ow	0.16217	0.21709	0.13124
Ow	0.15374	0.73122	0.12909
Ow	0.67549	0.25105	0.12587
Ow	0.65284	0.73787	0.13508
Ow	0.032	0.46843	0.88273
Ow	0.01848	0.01424	0.8888
Ow	0.52497	0.45401	0.87971
Ow	0.52663	0.95763	0.88824
Ow	0.31528	0.22214	0.63924
Ow	0.30876	0.70958	0.64041
Ow	0.83621	0.22509	0.62161
Ow	0.81746	0.72382	0.63495

Ow	0.37707	0.45654	0.36799
Ow	0.35438	0.93816	0.37678
Ow	0.87893	0.48301	0.37215
Ow	0.85447	0.93473	0.38183
Ob	0.40621	0.43929	0.12492
Ob	0.39002	0.92793	0.13252
Ob	0.92201	0.45694	0.12019
Ob	0.88291	0.92633	0.13532
Ob	0.2748	0.1716	0.88875
Ob	0.2628	0.66056	0.88025
Ob	0.77429	0.18202	0.89381
Oh	0.74691	0.66083	0.88646
Ob	0.05992	0.43598	0.63311
Ob	0.04589	0.92948	0.6367
Ob	0.54962	0.43734	0.63617
Ob	0.55521	0.93904	0.62969
Oh	0.14186	0.1922	0.38021
Ob	0.11018	0.67249	0.37696
Ob	0.63316	0.17452	0.37665
Ob	0.59494	0.65951	0.37355
O	0.26634	0.40945	0.20702
O	0.26116	0.91154	0.21369
O	0.7634	0.39523	0.19819
O	0.76218	0.91738	0.21747
O	0.1581	0.14745	0.80604
O	0.15395	0.64994	0.79971
O	0.65557	0.1431	0.80943
O	0.65403	0.65527	0.80097
O	0.91561	0.39432	0.71388
O	0.91598	0.90332	0.71957
O	0.41722	0.4058	0.71945
O	0.42071	0.9041	0.71377
O	0.00226	0.15219	0.29994
O	0.00211	0.65698	0.29334
O	0.50639	0.15252	0.29769
O	0.50034	0.65626	0.29025
O	0.49379	0.02524	0.21368
O	0.4969	0.5278	0.20879
O	0.99403	0.02821	0.21496
O	0.99308	0.52551	0.20972
O	0.38983	0.26623	0.80261
O	0.386	0.77033	0.79942
O	0.88697	0.26536	0.80535
O	0.88475	0.7669	0.80459

O	0.14778	0.02032	0.72012
O	0.14625	0.51619	0.71991
O	0.65253	0.02474	0.71514
O	0.64899	0.52397	0.71907
O	0.23596	0.27113	0.29116
O	0.23275	0.76874	0.29308
O	0.73934	0.27678	0.29293
O	0.73187	0.76972	0.29399
Ow	0.38291	0.32344	0.95905
Ow	0.54985	0.85762	0.96962
Ow	0.85706	0.38314	0.95317
Ow	0.96533	0.82877	0.92126
Ow	0.48878	0.12834	0.06907
Ow	0.34397	0.49199	0.04314
Ow	0.93767	0.11043	0.06718
Ow	0.98226	0.66017	0.06257
Ow	0.98342	0.32053	0.43446
Ow	0.02381	0.80709	0.43725
Ow	0.58068	0.29925	0.44505
Ow	0.64793	0.84354	0.44019
Ow	0.16571	0.09798	0.57189
Ow	0.22517	0.66143	0.54971
Ow	0.6602	0.2051	0.57411
Ow	0.58437	0.60468	0.57011
Ow	0.0889	0.10815	0.98721
Ow	0.08733	0.60305	0.98107
Ow	0.60148	0.11183	0.97231
Ow	0.61116	0.60945	0.06274
Ow	0.27449	0.0254	0.43968
Ow	0.4292	0.62607	0.44349
Ow	0.85688	0.19246	0.5251
Ow	0.79977	0.63917	0.522
Cw	0.40715	0.00926	0.00609
Cw	0.9108	0.48974	0.02625
Cw	0.88518	0.99206	0.00666
Cw	0.05456	0.25954	0.49303
Cw	0.57072	0.70161	0.50687
Ow	0.26254	0.14074	0.0451
Ow	0.25462	0.69208	0.0452
Ow	0.77024	0.17434	0.03581
Ow	0.78552	0.72657	0.00139
Ow	0.008	0.43015	0.52169
Ow	0.00441	0.94934	0.49052
Ow	0.48155	0.42239	0.49003

Ow	0.4502	0.82848	0.47375
Ow	0.4774	0.55298	0.9565
Ow	0.36705	0.5879	0.54041
Ow	0.96869	0.55113	0.57683
Ow	0.43372	0.06394	0.55186
Ow	0.99808	0.13328	0.56525
Ow	0.70903	0.36863	0.04554
Ow	0.13052	0.30941	0.05534
Ow	0.71233	0.89146	0.05584
Ow	0.23441	0.92036	0.0567
Ow	0.22733	0.40943	0.44921
Ow	0.81553	0.51107	0.45845
Ow	0.25682	0.84082	0.46918
Ow	0.94305	0.08651	0.45541
Ow	0.62809	0.33276	0.94911
Ow	0.17606	0.29772	0.94505
Ow	0.75228	0.85996	0.95258
Ow	0.28683	0.86389	0.95505
Ow	0.34164	0.35486	0.56885
Ow	0.35843	0.86502	0.57465
Ow	0.02711	0.69555	0.50996
Ow	0.38663	0.17985	0.50148
Ow	0.76974	0.32454	0.49404
Ow	0.77444	0.82796	0.52723
Ow	0.09371	0.41474	0.96397
Ow	0.06303	0.82531	0.99711
Ow	0.4939	0.70488	0.04451
Ow	0.6333	0.50694	0.97409
H	0.89496	0.57471	0.88992
H	0.10947	0.07104	0.38242
H	0.30393	0.64776	0.99609
Hw	0.78335	0.57616	0.97541
H	0.44226	0.34909	0.01494
Hw	0.21177	0.17734	0.51641
H	0.18623	0.63123	0.49101
H	0.4821	0.04986	0.48959
H	0.09652	0.8211	0.53504
H	0.56855	0.38086	0.52571
H	0.21808	0.5082	0.12506
H	0.16491	0.05414	0.1052
H	0.70813	0.51015	0.12244
H	0.68846	0.06431	0.09559
H	0.05559	0.23209	0.90445
H	0.11905	0.73942	0.88625

H	0.54695	0.23886	0.90562
H	0.57658	0.74677	0.89352
H	0.3709	0.51227	0.63462
H	0.35047	0.01452	0.62111
H	0.83861	0.49362	0.60948
H	0.84496	0.01943	0.59086
H	0.43928	0.27917	0.41153
H	0.40998	0.78379	0.39251
H	0.81276	0.10185	0.44329
H	0.89917	0.74944	0.40327
Hw	0.15306	0.25407	0.10341
Hw	0.22343	0.80889	0.12156
Hw	0.70226	0.31409	0.14803
Hw	0.73521	0.80779	0.12831
Hw	0.1038	0.54713	0.88192
Hw	0.99748	0.06527	0.8773
Hw	0.59114	0.5269	0.89144
Hw	0.53702	0.0285	0.88123
Hw	0.333	0.28553	0.61814
Hw	0.32252	0.77267	0.62084
Hw	0.90249	0.30431	0.62625
Hw	0.87894	0.80459	0.63079
Hw	0.45991	0.52641	0.37013
Hw	0.29869	0.87586	0.39965
Hw	0.83571	0.48383	0.40251
Hw	0.78594	0.90775	0.4067
H	0.76336	0.60108	0.88976
H	0.22362	0.22711	0.39588
Hw	0.31016	0.32751	0.96368
Hw	0.52523	0.87925	0.9408
Hw	0.91411	0.42777	0.925
Hw	0.98537	0.89991	0.9066
Hw	0.4331	0.10721	0.09884
Hw	0.389	0.57419	0.04361
Hw	0.91702	0.1025	0.10288
Hw	7.51E-04	0.71374	0.03581
Hw	0.89805	0.28312	0.42421
Hw	0.06812	0.81766	0.40526
Hw	0.60744	0.31945	0.41022
Hw	0.59008	0.86289	0.45288
Hw	0.2311	0.15162	0.59343
Hw	0.27542	0.74371	0.55357
Hw	0.6094	0.21239	0.59966
Hw	0.59342	0.62958	0.60411

Hw	0.15183	0.11789	0.00944
Hw	0.1631	0.65614	0.99838
Hw	0.66364	0.13713	0.99752
Hw	0.55812	0.63501	0.05456
Hw	0.20614	0.01569	0.42107
Hw	0.38651	0.66023	0.43292
Hw	0.83807	0.19243	0.56019
Hw	0.76357	0.64966	0.5518
Hw	0.33759	0.19317	0.06222
Hw	0.22766	0.68128	0.07984
Hw	0.84854	0.24567	0.04269
Hw	0.85254	0.7882	0.02035
Hw	0.07054	0.42398	0.53802
Hw	0.07167	0.97505	0.51281
Hw	0.44698	0.37701	0.46104
Hw	0.48276	0.83961	0.50698
Hw	0.42119	0.52984	0.98579
Hw	0.3252	0.62726	0.54342
Hw	0.00764	0.56779	0.60871
Hw	0.40917	0.11136	0.53756
Hw	0.02093	0.1789	0.59486
Hw	0.67793	0.32246	0.07583
Hw	0.2148	0.37767	0.04775
Hw	0.63747	0.81453	0.05606
Hw	0.20203	0.94351	0.08375
Hw	0.2998	0.48469	0.45579
Hw	0.80127	0.55052	0.48418
Hw	0.25478	0.90771	0.4681
Hw	0.93925	0.064	0.42134
Hw	0.62649	0.39965	0.95368
Hw	0.14783	0.3477	0.95269
Hw	0.67488	0.85798	0.9575
Hw	0.29869	0.8554	0.91996
Hw	0.27503	0.36438	0.5613
Hw	0.43866	0.89864	0.59022
Hw	0.01915	0.64215	0.53495
Hw	0.33571	0.11873	0.47884
Hw	0.7208	0.28301	0.52423
Hw	0.77902	0.87578	0.55368
Hw	0.04224	0.39384	0.9951
Hw	0.02374	0.85804	0.01596
Hw	0.46103	0.72405	0.0734
Hw	0.6008	0.47966	0.00769
Hw	0.91992	0.63718	0.95193

Hw	0.26183	0.23571	0.46533
Hw	0.24675	0.2346	0.12732
Hw	0.09248	0.70796	0.10413
Hw	0.74511	0.24205	0.12542
Hw	0.64235	0.68315	0.11076
Hw	0.05328	0.43254	0.9069
Hw	0.10773	0.06377	0.8948
Hw	0.48254	0.40714	0.90922
Hw	0.60984	0.97167	0.88324
Hw	0.39437	0.228	0.63867
Hw	0.38635	0.71312	0.63693
Hw	0.86193	0.18427	0.63987
Hw	0.86626	0.69169	0.63253
Hw	0.3834	0.39728	0.3818
Hw	0.43542	0.94736	0.37809
Hw	0.96233	0.55205	0.37432
Hw	0.86819	0.87491	0.37965
Hw	0.3521	0.26238	0.9359
Hw	0.51907	0.8805	0.99792
Hw	0.82008	0.30715	0.94141
Hw	0.88395	0.76915	0.91002
Hw	0.56937	0.16961	0.08457
Hw	0.3699	0.47462	0.07326
Hw	0.01465	0.18669	0.06303
Hw	0.94024	0.67602	0.08893
Hw	0.03668	0.38123	0.41016
Hw	0.02594	0.74988	0.45545
Hw	0.65079	0.30313	0.45943
Hw	0.63018	0.83358	0.4051
Hw	0.11069	0.03426	0.59467
Hw	0.19764	0.63326	0.58345
Hw	0.72087	0.2035	0.59396
Hw	0.54403	0.52421	0.57572
Hw	0.12666	0.18293	0.97158
Hw	0.09156	0.63999	0.95015
Hw	0.65257	0.13928	0.9415
Hw	0.68154	0.64717	0.03778
Hw	0.32489	0.0156	0.41499
Hw	0.48483	0.63692	0.415
Hw	0.77975	0.16604	0.50905
Hw	0.74593	0.63599	0.49641
Hw	0.29216	0.12631	0.01355
Hw	0.32753	0.7714	0.04233
Hw	0.79793	0.1417	0.01057

Hw	0.76766	0.76281	0.97612
Hw	0.05344	0.48097	0.49332
Hw	0.01346	0.9012	0.46753
Hw	0.55087	0.49768	0.47709
Hw	0.38251	0.84028	0.47586
Hw	0.42356	0.52052	0.929
Hw	0.29641	0.50877	0.54481
Hw	0.98365	0.49825	0.56061
Hw	0.52239	0.11585	0.55901
Hw	0.05859	0.11221	0.56457
Hw	0.64203	0.32944	0.02275
Hw	0.07524	0.33397	0.04854
Hw	0.69528	0.92715	0.08261
Hw	0.16472	0.87961	0.03464
Hw	0.23601	0.40642	0.41355
Hw	0.79685	0.44183	0.47424
Hw	0.17559	0.78012	0.48377
Hw	0.9616	0.03754	0.47211
Hw	0.71604	0.36235	0.94154
Hw	0.22028	0.32306	0.91233
Hw	0.76293	0.85767	0.91673
Hw	0.20113	0.84385	0.9585
Hw	0.39396	0.3756	0.53822
Hw	0.36637	0.93263	0.56178
Hw	0.94095	0.67683	0.51252
Hw	0.46398	0.23246	0.48155
Hw	0.85624	0.35343	0.50135
Hw	0.85995	0.86843	0.51227
Hw	0.16191	0.49309	0.96813
Hw	0.03107	0.82188	0.96433
Hw	0.49732	0.74854	0.01628
Hw	0.58502	0.53746	0.96477

Supplementary Table 7 Atom positions of 1.0CSH.

$a=13.449 \text{ \AA}$, $b=14.815 \text{ \AA}$, $c=22.595 \text{ \AA}$, $\alpha=91.6^\circ$, $\beta=86.5^\circ$, $\gamma=125.1^\circ$			
Name of atoms	X	Y	Z
Ca	0.3685	0.2125	0.29452
Ca	0.35644	0.70357	0.29067
Ca	0.8685	0.2125	0.29452
Ca	0.85644	0.70357	0.29067
Ca	0.34761	0.3776	0.69942
Ca	0.3279	0.86039	0.69883
Ca	0.84761	0.3776	0.69942

Ca	0.8279	0.86039	0.69883
Ca	0.07996	0.12852	0.78069
Ca	0.07816	0.61772	0.78792
Ca	0.57996	0.12852	0.78069
Ca	0.57817	0.61772	0.78792
Ca	0.14098	0.45792	0.20252
Ca	0.14913	0.97134	0.19729
Ca	0.64098	0.45792	0.20252
Ca	0.64913	0.97134	0.19729
Ca	0.17642	0.22937	0.20559
Ca	0.17064	0.71889	0.19888
Ca	0.67642	0.22937	0.20559
Ca	0.67064	0.71889	0.19888
Ca	0.0947	0.38042	0.76993
Ca	0.08751	0.87502	0.77106
Ca	0.5947	0.38042	0.76993
Ca	0.58751	0.87502	0.77106
Ca	0.36548	0.13657	0.69944
Ca	0.37895	0.63422	0.69178
Ca	0.86548	0.13657	0.69944
Ca	0.87895	0.63422	0.69178
Ca	0.4018	0.49587	0.27725
Ca	0.39578	0.97605	0.28431
Ca	0.9018	0.49587	0.27725
Ca	0.89578	0.97605	0.28431
Si	0.44508	0.21911	0.16804
Si	0.42793	0.69043	0.16791
Si	0.94508	0.21911	0.16804
Si	0.92793	0.69043	0.16791
Si	0.33128	0.35816	0.83657
Si	0.33049	0.8573	0.83154
Si	0.83128	0.35816	0.83657
Si	0.83049	0.8573	0.83154
Si	0.14688	0.14655	0.65043
Si	0.13779	0.62532	0.66032
Si	0.64688	0.14655	0.65043
Si	0.63779	0.62532	0.66032
Si	0.12028	0.44384	0.34482
Si	0.12242	0.93858	0.32979
Si	0.62028	0.44384	0.34482
Si	0.62242	0.93858	0.32979
Si	0.41093	0.04427	0.9225
Si	0.42937	0.5551	0.9248
Si	0.91093	0.04427	0.9225

Si	0.92937	0.5551	0.9248
Si	0.18962	0.1121	0.43048
Si	0.20448	0.63495	0.43781
Si	0.68962	0.1121	0.43048
Si	0.70448	0.63495	0.43781
Si	0.40783	0.48299	0.14589
Si	0.4163	0.99492	0.15293
Si	0.90783	0.48299	0.14589
Si	0.9163	0.99492	0.15293
Si	0.33049	0.1471	0.83824
Si	0.33851	0.64593	0.83931
Si	0.83049	0.1471	0.83824
Si	0.83851	0.64593	0.83931
Si	0.11598	0.40606	0.6361
Si	0.10651	0.90928	0.63849
Si	0.61598	0.40606	0.6361
Si	0.60651	0.90928	0.63849
Si	0.12265	0.23436	0.35754
Si	0.11089	0.72155	0.35681
Si	0.62265	0.23436	0.35754
Si	0.61089	0.72155	0.35681
O	0.52675	0.32841	0.12897
O	0.51816	0.81304	0.1424
O	0.02675	0.32841	0.12897
O	0.01816	0.81304	0.1424
Ob	0.33913	0.92455	0.89265
Ob	0.34798	0.43205	0.89703
Ob	0.83913	0.92455	0.89265
Ob	0.84798	0.43205	0.89703
O	0.22784	0.24118	0.60157
O	0.1968	0.73994	0.62637
O	0.72784	0.24118	0.60157
O	0.6968	0.73994	0.62637
Ob	0.11538	0.00883	0.38857
Ob	0.13502	0.51806	0.40664
Ob	0.61538	0.00883	0.38857
Ob	0.63502	0.51806	0.40664
Ob	0.41941	0.10617	0.1335
Ob	0.41313	0.59539	0.11854
Ob	0.91941	0.10617	0.1335
Ob	0.91313	0.59539	0.11854
Ob	0.30875	0.24263	0.86087
Ob	0.32803	0.75122	0.85622
Ob	0.80875	0.24263	0.86087

Ob	0.82803	0.75122	0.85622
Ob	0.11292	0.02478	0.62006
Ob	0.13208	0.52937	0.61532
Ob	0.61292	0.02478	0.62006
Ob	0.63208	0.52937	0.61532
Ob	0.12173	0.34283	0.37337
Ob	0.12182	0.83945	0.36183
Ob	0.62173	0.34283	0.37337
Ob	0.62182	0.83945	0.36183
O	0.523	0.24896	0.22775
O	0.48243	0.67892	0.22776
O	0.023	0.24896	0.22775
O	0.98243	0.67892	0.22776
O	0.44741	0.93424	0.78496
O	0.45122	0.42516	0.79116
O	0.94741	0.93424	0.78496
O	0.95122	0.42516	0.79116
O	0.23202	0.18299	0.70657
O	0.22536	0.65558	0.71421
O	0.73202	0.18299	0.70657
O	0.72536	0.65558	0.71421
O	0.24624	0.0201	0.29019
O	0.23103	0.5131	0.29625
O	0.74624	0.0201	0.29019
O	0.73103	0.5131	0.29625
O	0.31368	0.18698	0.19481
O	0.29559	0.6599	0.19057
O	0.81368	0.18698	0.19481
O	0.79559	0.6599	0.19057
O	0.21933	0.32607	0.79561
O	0.21351	0.81534	0.79214
O	0.71933	0.32607	0.79561
O	0.71351	0.81534	0.79214
O	0.0212	0.12093	0.67933
O	0.00318	0.57375	0.68984
O	0.5212	0.12093	0.67933
O	0.50318	0.57375	0.68984
O	0.99543	0.40345	0.31357
O	0.01118	0.89177	0.28681
O	0.49543	0.40345	0.31357
O	0.51118	0.89177	0.28681
Oh	0.41438	0.03519	0.99468
Oh	0.43655	0.55529	0.99699
Oh	0.91438	0.03519	0.99468

Oh	0.93655	0.55529	0.99699
Oh	0.16653	0.07235	0.50158
Oh	0.20426	0.63504	0.51241
Oh	0.66653	0.07235	0.50158
Oh	0.70426	0.63504	0.51241
Oh	0.22909	0.56786	0.05199
Oh	0.22258	0.04579	0.07892
Oh	0.72909	0.56786	0.05199
Oh	0.72258	0.04579	0.07892
Oh	0.06093	0.11865	0.89541
Oh	0.07741	0.62189	0.89646
Oh	0.56093	0.11865	0.89541
Oh	0.57741	0.62189	0.89646
Ow	0.43353	0.48496	0.55734
Ow	0.40701	0.9963	0.56541
Ow	0.93353	0.48496	0.55734
Ow	0.90701	0.9963	0.56541
Ow	0.3468	0.17142	0.41171
Ow	0.36041	0.70179	0.41299
Ow	0.8468	0.17142	0.41171
Ow	0.86041	0.70179	0.41299
Ow	0.18701	0.21696	0.09166
Ow	0.20264	0.73701	0.08793
Ow	0.68701	0.21696	0.09166
Ow	0.70264	0.73701	0.08793
Ow	0.1035	0.43632	0.93031
Ow	0.11704	0.9904	0.95666
Ow	0.6035	0.43632	0.93031
Ow	0.61704	0.9904	0.95666
Ow	0.38136	0.42565	0.4131
Ow	0.37619	0.91125	0.38567
Ow	0.88136	0.42565	0.4131
Ow	0.87619	0.91125	0.38567
O	0.39727	0.40891	0.09204
O	0.41981	0.93114	0.09616
O	0.89727	0.40891	0.09204
O	0.91981	0.93114	0.09616
Ob	0.35037	0.10461	0.90223
Ob	0.3785	0.62164	0.90202
Ob	0.85037	0.10461	0.90223
Ob	0.8785	0.62164	0.90202
O	0.10511	0.34557	0.57476
O	0.09749	0.8477	0.57747
O	0.60511	0.34557	0.57476

O	0.59749	0.8477	0.57747
Ob	0.16286	0.20322	0.42521
Ob	0.15701	0.70808	0.42317
Ob	0.66286	0.20322	0.42521
Ob	0.65701	0.70808	0.42317
O	0.28936	0.41939	0.19228
O	0.29068	0.91306	0.19432
O	0.78936	0.41939	0.19228
O	0.79068	0.91306	0.19432
O	0.21531	0.0514	0.80388
O	0.20959	0.54218	0.81971
O	0.71531	0.0514	0.80388
O	0.70959	0.54218	0.81971
O	0.99375	0.33609	0.67874
O	0.98384	0.82954	0.68047
O	0.49375	0.33609	0.67874
O	0.48384	0.82954	0.68047
O	0.98707	0.13428	0.34229
O	0.96868	0.62143	0.35301
O	0.48707	0.13428	0.34229
O	0.46868	0.62143	0.35301
O	0.52687	0.0376	0.19674
O	0.5223	0.52324	0.1863
O	0.02687	0.0376	0.19674
O	0.0223	0.52324	0.1863
O	0.4491	0.19246	0.79291
O	0.44488	0.68086	0.78772
O	0.9491	0.19246	0.79291
O	0.94488	0.68086	0.78772
O	0.21908	0.94413	0.67942
O	0.22668	0.44085	0.67733
O	0.71908	0.94413	0.67942
O	0.72668	0.44085	0.67733
O	0.22067	0.25057	0.3068
O	0.19351	0.72031	0.30239
O	0.72067	0.25057	0.3068
O	0.69351	0.72031	0.30239
Ow	0.38024	0.16034	0.58454
Ow	0.40347	0.64404	0.5808
Ow	0.88024	0.16034	0.58454
Ow	0.90347	0.64404	0.5808
Ow	0.15931	0.32364	0.00492
Ow	0.14821	0.81671	0.99845
Ow	0.65931	0.32364	0.00492

Ow	0.64821	0.81671	0.99845
Ow	0.45695	0.33143	0.48978
Ow	0.44701	0.85255	0.50526
Ow	0.95695	0.33143	0.48978
Ow	0.94701	0.85255	0.50526
Cw	0.2723	0.33539	0.50988
Cw	0.24631	0.82375	0.53275
Cw	0.7723	0.33539	0.50988
Cw	0.74631	0.82375	0.53275
Cw	0.53915	0.3936	0.03273
Cw	0.54006	0.88193	0.04373
Cw	0.03915	0.3936	0.03273
Cw	0.04006	0.88193	0.04373
Ow	0.3712	0.22888	0.99922
Ow	0.37384	0.76756	0.9854
Ow	0.8712	0.22888	0.99922
Ow	0.87384	0.76756	0.9854
Ow	0.2467	0.47236	0.48695
Ow	0.24138	0.9364	0.46458
Ow	0.7467	0.47236	0.48695
Ow	0.74138	0.9364	0.46458
H	0.41647	0.00816	0.03613
H	0.43212	0.56038	0.0427
H	0.91647	0.00816	0.03613
H	0.93212	0.56038	0.0427
H	0.15671	0.06098	0.54757
H	0.1784	0.59246	0.553
H	0.65671	0.06098	0.54757
H	0.6784	0.59246	0.553
H	0.29745	0.57339	0.07411
H	0.30582	0.06974	0.09458
H	0.79745	0.57339	0.07411
H	0.80582	0.06974	0.09458
Hw	0.42497	0.54774	0.56916
Hw	0.39625	0.05908	0.57324
Hw	0.92497	0.54774	0.56916
Hw	0.89625	0.05908	0.57324
Hw	0.2734	0.29098	0.08988
Hw	0.28818	0.8106	0.089
Hw	0.7734	0.29098	0.08988
Hw	0.78818	0.8106	0.089
Hw	0.086	0.0278	0.93493
Hw	0.12479	0.48119	0.89224
Hw	0.586	0.0278	0.93493

Hw	0.62479	0.48119	0.89224
Hw	0.34254	0.94119	0.4155
Hw	0.4073	0.50327	0.40218
Hw	0.84254	0.94119	0.4155
Hw	0.9073	0.50327	0.40218
Hw	0.33138	0.19337	0.58576
Hw	0.35231	0.63699	0.54762
Hw	0.83138	0.19337	0.58576
Hw	0.85231	0.63699	0.54762
Hw	0.15429	0.27554	0.03843
Hw	0.16503	0.77682	0.02835
Hw	0.65429	0.27554	0.03843
Hw	0.66503	0.77682	0.02835
Hw	0.50916	0.33433	0.52222
Hw	0.49797	0.8415	0.53269
Hw	0.00916	0.33433	0.52222
Hw	0.99797	0.8415	0.53269
Hw	0.3164	0.15949	0.02457
Hw	0.31912	0.68594	0.99699
Hw	0.8164	0.15949	0.02457
Hw	0.81912	0.68594	0.99699
Hw	0.21215	0.97916	0.48604
Hw	0.18366	0.43743	0.52249
Hw	0.71215	0.97916	0.48604
Hw	0.68366	0.43743	0.52249
Hw	0.50525	0.49929	0.5795
Hw	0.47908	0.01741	0.58939
Hw	0.00525	0.49929	0.5795
Hw	0.97908	0.01741	0.58939
Hw	0.19946	0.15545	0.08776
Hw	0.21457	0.67668	0.07596
Hw	0.69946	0.15545	0.08776
Hw	0.71457	0.67668	0.07596
Hw	0.15645	0.40819	0.92447
Hw	0.2008	0.02263	0.93609
Hw	0.65645	0.40819	0.92447
Hw	0.7008	0.02263	0.93609
Hw	0.41762	0.4072	0.37771
Hw	0.468	0.95454	0.39027
Hw	0.91762	0.4072	0.37771
Hw	0.968	0.95454	0.39027
Hw	0.47011	0.22792	0.58201
Hw	0.48074	0.7247	0.57944
Hw	0.97011	0.22792	0.58201

Hw	0.98074	0.7247	0.57944
Hw	0.23882	0.34975	0.98219
Hw	0.20776	0.83527	0.96328
Hw	0.73882	0.34975	0.98219
Hw	0.70776	0.83527	0.96328
Hw	0.51286	0.40015	0.46399
Hw	0.50294	0.93552	0.49913
Hw	0.01286	0.40015	0.46399
Hw	0.00294	0.93552	0.49913
Hw	0.36479	0.19881	0.95726
Hw	0.37378	0.76549	0.94025
Hw	0.86479	0.19881	0.95726
Hw	0.87378	0.76549	0.94025
Hw	0.18837	0.89983	0.42864
Hw	0.20137	0.46144	0.4499
Hw	0.68837	0.89983	0.42864
Hw	0.70137	0.46144	0.4499
H	0.15494	0.17452	0.8924
H	0.17109	0.66797	0.89576
H	0.65494	0.17452	0.8924
H	0.67109	0.66797	0.89576
Hw	0.40885	0.23398	0.43857
Hw	0.42818	0.77297	0.43199
Hw	0.90885	0.23398	0.43857
Hw	0.92818	0.77297	0.43199
Hw	0.39841	0.1475	0.38959
Hw	0.40397	0.66699	0.39453
Hw	0.89841	0.1475	0.38959

Supplementary Table 8 Atom positions of 1.3CSH.

$a=22.348 \text{ \AA}$, $b=14.677 \text{ \AA}$, $c=19.983 \text{ \AA}$, $\alpha=102.4^\circ$, $\beta=94.6^\circ$, $\gamma=90.6^\circ$			
Name of atoms	X	Y	Z
Si	0.19295	0.1079	0.1117
Si	0.19668	0.09501	0.61876
Si	0.18987	0.60623	0.11013
Si	0.19105	0.59211	0.61372
Si	0.69235	0.10363	0.1075
Si	0.69318	0.09401	0.61767
Si	0.6906	0.60589	0.1119
Si	0.69097	0.59075	0.6108
Si	0.30552	0.3679	0.40789
Si	0.3063	0.38452	0.90532
Si	0.30057	0.87	0.40659

Si	0.29968	0.88334	0.90359
Si	0.80537	0.3695	0.40686
Si	0.805	0.38299	0.9071
Si	0.80251	0.87218	0.40734
Si	0.80186	0.88096	0.9017
Si	0.44181	0.35645	0.11136
Si	0.44885	0.34782	0.618
Si	0.44123	0.85571	0.10826
Si	0.44075	0.84201	0.6153
Si	0.94223	0.35476	0.11078
Si	0.94636	0.34052	0.61512
Si	0.9411	0.85229	0.10984
Si	0.94038	0.84208	0.61112
Si	0.05402	0.11854	0.40776
Si	0.0484	0.12937	0.89876
Si	0.05464	0.61628	0.40328
Si	0.04895	0.62787	0.89909
Si	0.55306	0.12036	0.40702
Si	0.55247	0.13338	0.9036
Si	0.55425	0.61968	0.39931
Si	0.54971	0.63286	0.90645
Si	0.19519	0.3142	0.11277
Si	0.19828	0.30273	0.61164
Si	0.19158	0.81917	0.11913
Si	0.19331	0.79958	0.61304
Si	0.69504	0.3138	0.11405
Si	0.69886	0.3004	0.61221
Si	0.69177	0.81786	0.11942
Si	0.69486	0.8001	0.6112
Si	0.30479	0.15588	0.39924
Si	0.30163	0.17425	0.89953
Si	0.29992	0.6588	0.39984
Si	0.29557	0.67414	0.90253
Si	0.80356	0.15638	0.39614
Si	0.80095	0.17248	0.90155
Si	0.80061	0.66032	0.39772
Si	0.79739	0.67157	0.90042
Si	0.44351	0.06788	0.11832
Si	0.44412	0.05264	0.61774
Si	0.44197	0.56927	0.12124
Si	0.4497	0.55277	0.6077
Si	0.94251	0.06542	0.11795
Si	0.94645	0.05289	0.61897
Si	0.94618	0.56541	0.11545

Si	0.94485	0.54933	0.60872
Si	0.05312	0.40268	0.39437
Si	0.05179	0.42001	0.90002
Si	0.0518	0.90997	0.40298
Si	0.05324	0.92442	0.90655
Si	0.55402	0.40452	0.39324
Si	0.54882	0.42514	0.90229
Si	0.55017	0.91143	0.40461
Si	0.54851	0.92284	0.90104
Oh	0.20137	0.06555	0.18589
Oh	0.2058	0.06279	0.69751
Oh	0.19051	0.56349	0.18472
Oh	0.18486	0.55309	0.69055
Oh	0.70053	0.0628	0.18437
Oh	0.68621	0.05591	0.69433
Oh	0.6921	0.56224	0.18623
Oh	0.68612	0.55072	0.68671
Oh	0.30056	0.40841	0.32977
Oh	0.3116	0.42248	0.82465
Oh	0.28642	0.90791	0.33014
Oh	0.28829	0.91856	0.82392
Oh	0.80433	0.41543	0.33378
Oh	0.80902	0.41919	0.82564
Oh	0.79308	0.91388	0.33106
Oh	0.79231	0.9166	0.82286
Oh	0.44992	0.31558	0.18772
Oh	0.46262	0.31417	0.69734
Oh	0.45003	0.81341	0.18468
Oh	0.43313	0.80486	0.69179
Oh	0.95031	0.31374	0.18599
Oh	0.95786	0.31338	0.69709
Oh	0.94331	0.80803	0.18347
Oh	0.93669	0.80311	0.69066
Oh	0.04536	0.15988	0.33179
Oh	0.0364	0.16244	0.82049
Oh	0.05195	0.65404	0.32519
Oh	0.03807	0.65897	0.8168
Oh	0.54664	0.16391	0.33376
Oh	0.54231	0.1652	0.82194
Oh	0.55285	0.65713	0.32205
Oh	0.5449	0.67359	0.82932
H	0.21282	0.00139	0.19616
H	0.18831	0.06018	0.74376
H	0.20165	0.49812	0.19345

H	0.14379	0.52476	0.69861
H	0.71049	0.99739	0.19382
H	0.64464	0.02519	0.69823
H	0.70294	0.4964	0.19424
H	0.64555	0.52401	0.69779
H	0.29086	0.47496	0.32211
H	0.35142	0.45492	0.81662
H	0.28624	0.97563	0.32215
H	0.28604	0.98903	0.82249
H	0.79323	0.47929	0.32225
H	0.85025	0.44717	0.81758
H	0.78225	0.97865	0.32114
H	0.78836	0.9871	0.82128
H	0.45707	0.24786	0.19471
H	0.46409	0.24329	0.69608
H	0.46064	0.74748	0.19276
H	0.39277	0.77482	0.7006
H	0.9621	0.24959	0.19585
H	0.95815	0.24269	0.69814
H	0.95275	0.74498	0.19745
H	0.89477	0.77545	0.69726
H	0.03714	0.2257	0.3217
H	0.03815	0.23334	0.82022
H	0.04703	0.72302	0.3203
H	0.0315	0.72941	0.81775
H	0.53172	0.22367	0.31902
H	0.53909	0.23656	0.82337
H	0.54699	0.72406	0.31323
H	0.5359	0.74124	0.82416
Oh	0.2179	0.39539	0.1956
Oh	0.21715	0.38575	0.68932
Oh	0.19787	0.89199	0.20381
Oh	0.20004	0.88253	0.69202
Oh	0.7165	0.39179	0.19641
Oh	0.71796	0.38372	0.68952
Oh	0.69988	0.89213	0.20544
Oh	0.70736	0.87904	0.6905
Oh	0.30589	0.07896	0.31782
Oh	0.29923	0.09433	0.81904
Oh	0.27975	0.57955	0.31927
Oh	0.2771	0.59191	0.82502
Oh	0.79567	0.08436	0.30963
Oh	0.79903	0.09328	0.82105
Oh	0.78099	0.58359	0.31572

Oh	0.77866	0.58976	0.82327
Oh	0.4504	0.14308	0.19945
Oh	0.44742	0.1331	0.70071
Oh	0.44773	0.64326	0.20409
Oh	0.47174	0.63738	0.68365
Oh	0.95091	0.13875	0.20357
Oh	0.95475	0.13386	0.69788
Oh	0.97119	0.64016	0.19681
Oh	0.95681	0.62884	0.69001
Oh	0.04661	0.32928	0.31236
Oh	0.05139	0.33757	0.81997
Oh	0.03559	0.82779	0.32355
Oh	0.0524	0.83766	0.82708
Oh	0.54605	0.33423	0.30727
Oh	0.54193	0.34226	0.82301
Oh	0.52859	0.83213	0.32461
Oh	0.53054	0.84665	0.81714
H	0.26186	0.42092	0.19746
H	0.20827	0.45642	0.69381
H	0.18516	0.93329	0.24927
H	0.2107	0.95312	0.69712
H	0.76152	0.41255	0.20072
H	0.70944	0.45432	0.69305
H	0.6841	0.93217	0.24963
H	0.7098	0.95148	0.69951
H	0.31028	0.0483	0.26668
H	0.29173	0.07541	0.76624
H	0.23457	0.55937	0.31292
H	0.28663	0.52192	0.82195
H	0.80953	0.04375	0.26454
H	0.8081	0.10388	0.77324
H	0.73603	0.56241	0.30921
H	0.78595	0.51909	0.82067
H	0.43767	0.17335	0.24775
H	0.43687	0.17158	0.74804
H	0.43221	0.67896	0.24929
H	0.46399	0.70864	0.69253
H	0.93357	0.18061	0.24598
H	0.97297	0.14522	0.74831
H	0.01398	0.67058	0.20034
H	0.95929	0.70032	0.69235
H	0.05625	0.29591	0.26333
H	0.05511	0.31384	0.76794
H	0.99119	0.80347	0.31406

H	0.09417	0.80761	0.81957
H	0.55953	0.29082	0.26307
H	0.52355	0.32826	0.77269
H	0.48586	0.80145	0.31815
H	0.54698	0.81759	0.77043
O	0.24745	0.32004	0.0649
O	0.25005	0.30169	0.56231
O	0.24554	0.83196	0.0749
O	0.24881	0.8049	0.56998
O	0.74688	0.32062	0.0656
O	0.7507	0.29786	0.56266
O	0.7462	0.82936	0.07556
O	0.74764	0.80341	0.56429
O	0.24934	0.14272	0.44119
O	0.2459	0.16662	0.94208
O	0.24839	0.65163	0.44871
O	0.24476	0.67268	0.95391
O	0.74965	0.14268	0.44035
O	0.74675	0.16317	0.94618
O	0.74853	0.65121	0.4455
O	0.74734	0.67324	0.95255
O	0.49738	0.07659	0.0724
O	0.49915	0.06168	0.5751
O	0.49564	0.57771	0.07519
O	0.49993	0.55043	0.55533
O	0.9969	0.07648	0.07393
O	1.467E-4	0.05886	0.57286
O	0.99796	0.56873	0.06609
O	0.99816	0.55355	0.56123
O	0.9994	0.39209	0.44013
O	0.99747	0.41047	0.94486
O	0.99871	0.90465	0.45051
O	0.99778	0.91797	0.94927
O	0.49981	0.39024	0.43682
O	0.49577	0.41836	0.94979
O	0.49775	0.90684	0.45325
O	0.49478	0.91956	0.94744
O	0.24687	0.07969	0.06553
O	0.24975	0.0642	0.57133
O	0.24568	0.57347	0.06791
O	0.2479	0.56063	0.57274
O	0.74714	0.07345	0.06388
O	0.74819	0.06156	0.57359
O	0.74639	0.57525	0.0691

O	0.74719	0.55849	0.56914
O	0.25042	0.40095	0.45033
O	0.24959	0.41731	0.94472
O	0.24751	0.89768	0.4538
O	0.24536	0.91702	0.94878
O	0.75005	0.39999	0.45015
O	0.74902	0.42033	0.94726
O	0.74794	0.90142	0.45191
O	0.74694	0.9094	0.94672
O	0.99666	0.32558	0.06533
O	0.00127	0.30928	0.56955
O	0.99646	0.82353	0.06604
O	0.99609	0.80813	0.56975
O	0.4972	0.32699	0.06782
O	0.50226	0.31446	0.5702
O	0.49604	0.82706	0.06425
O	0.49678	0.80753	0.57363
O	0.49907	0.14814	0.45337
O	0.49746	0.164	0.94785
O	0.49819	0.65423	0.44131
O	0.49503	0.66512	0.95093
O	0.9994	0.14699	0.4524
O	0.99591	0.15897	0.94714
O	0.99861	0.64992	0.44466
O	0.99602	0.66222	0.94591
O	0.13342	0.32585	0.07172
O	0.1354	0.31789	0.57374
O	0.13054	0.82622	0.0744
O	0.13288	0.8076	0.56838
O	0.63285	0.32887	0.0749
O	0.63646	0.31572	0.5735
O	0.63119	0.82874	0.07553
O	0.63224	0.81085	0.57088
O	0.36493	0.15142	0.4468
O	0.36167	0.16559	0.94572
O	0.36267	0.64624	0.43956
O	0.35862	0.65639	0.94022
O	0.86443	0.14587	0.44012
O	0.86205	0.1624	0.94579
O	0.86288	0.64603	0.43756
O	0.86083	0.65212	0.9367
O	0.38247	0.07549	0.07281
O	0.38343	0.06101	0.57372
O	0.38094	0.57981	0.07669

O	0.38661	0.56729	0.56999
O	0.88181	0.07359	0.07348
O	0.88481	0.06297	0.57528
O	0.88435	0.58333	0.07647
O	0.88349	0.56366	0.5675
O	0.1144	0.39423	0.43935
O	0.11267	0.41437	0.94562
O	0.11331	0.90094	0.44588
O	0.11364	0.91882	0.95154
O	0.61491	0.39441	0.43727
O	0.61042	0.41589	0.94571
O	0.61197	0.89955	0.44568
O	0.60934	0.90683	0.94276
O	0.13117	0.079	0.06638
O	0.13498	0.05965	0.57406
O	0.12987	0.5783	0.06147
O	0.13183	0.55847	0.56469
O	0.63121	0.07252	0.06268
O	0.63289	0.06195	0.56914
O	0.63013	0.57626	0.06464
O	0.63114	0.55946	0.56204
O	0.36656	0.39818	0.45318
O	0.36548	0.41707	0.95272
O	0.36272	0.90313	0.44882
O	0.36059	0.91765	0.94771
O	0.86626	0.39608	0.45439
O	0.86458	0.41656	0.95392
O	0.86367	0.9046	0.45149
O	0.86236	0.9159	0.9468
O	0.38129	0.32417	0.06599
O	0.38729	0.30993	0.57486
O	0.38003	0.82372	0.06363
O	0.38134	0.81178	0.56543
O	0.88098	0.32223	0.06615
O	0.88578	0.2995	0.57177
O	0.88051	0.82272	0.06194
O	0.88066	0.80954	0.56404
O	0.11519	0.14954	0.45301
O	0.11029	0.16786	0.94259
O	0.11478	0.64787	0.44954
O	0.11105	0.66771	0.93874
O	0.61476	0.15118	0.45251
O	0.61255	0.17055	0.94846
O	0.61412	0.65142	0.44717

O	0.6112	0.66676	0.94969
Ob	0.19367	0.22156	0.14697
Ob	0.1957	0.21067	0.64744
Ob	0.19368	0.71923	0.14578
Ob	0.19434	0.7056	0.64732
Ob	0.6936	0.21681	0.14388
Ob	0.69709	0.20852	0.64883
Ob	0.6931	0.71897	0.14723
Ob	0.69429	0.70416	0.64359
Ob	0.30232	0.25517	0.3713
Ob	0.30268	0.27196	0.8696
Ob	0.30082	0.75565	0.37057
Ob	0.29467	0.7699	0.87266
Ob	0.80185	0.25666	0.36989
Ob	0.7976	0.2709	0.87407
Ob	0.80139	0.75895	0.37036
Ob	0.80114	0.7667	0.86874
Ob	0.44248	0.46923	0.1474
Ob	0.45158	0.46184	0.64426
Ob	0.44363	0.96781	0.14579
Ob	0.44585	0.95638	0.64868
Ob	0.94245	0.46881	0.14524
Ob	0.94734	0.45445	0.63978
Ob	0.94348	0.96563	0.14586
Ob	0.94606	0.95466	0.64781
Ob	0.05229	0.0054	0.37077
Ob	0.05115	0.01469	0.86958
Ob	0.05183	0.50326	0.36896
Ob	0.04449	0.51483	0.86912
Ob	0.55219	0.00633	0.37177
Ob	0.55223	0.01968	0.87202
Ob	0.55166	0.50576	0.3683
Ob	0.54313	0.52063	0.87164
Oh	0.07905	0.48908	0.18942
Oh	0.08554	0.45027	0.70386
Oh	0.07853	0.01334	0.19248
Oh	0.08014	0.95293	0.69425
Oh	0.57839	0.4966	0.19277
Oh	0.58667	0.45594	0.70789
Oh	0.57902	0.0096	0.19268
Oh	0.58206	0.95887	0.6982
Oh	0.41851	0.97485	0.32105
Oh	0.41463	0.02072	0.82497
Oh	0.41673	0.46599	0.32315

Oh	0.40825	0.53013	0.81095
Oh	0.91705	0.96966	0.32104
Oh	0.91767	0.01156	0.81668
Oh	0.91883	0.46892	0.3222
Oh	0.90705	0.52536	0.81385
Oh	0.32834	0.24911	0.19067
Oh	0.32785	0.20786	0.69484
Oh	0.3271	0.76427	0.19152
Oh	0.33225	0.71139	0.70937
Oh	0.82817	0.24447	0.19035
Oh	0.83067	0.18655	0.72035
Oh	0.82659	0.76282	0.19333
Oh	0.83057	0.71048	0.69748
Oh	0.16883	0.21788	0.32359
Oh	0.16884	0.25792	0.82428
Oh	0.16722	0.73153	0.32501
Oh	0.15875	0.74567	0.82257
Oh	0.66749	0.21039	0.32242
Oh	0.66394	0.27767	0.82332
Oh	0.66753	0.73465	0.32643
Oh	0.66679	0.7311	0.82234
H	0.11866	0.52609	0.19018
H	0.09399	0.38641	0.67411
H	0.12412	0.02631	0.19734
H	0.12284	0.92816	0.69572
H	0.62067	0.52545	0.19285
H	0.59121	0.38811	0.68292
H	0.624	0.0255	0.1941
H	0.59857	0.89279	0.69146
H	0.37885	0.00918	0.32245
H	0.37397	0.05243	0.82857
H	0.37268	0.44276	0.31972
H	0.39697	0.59184	0.84198
H	0.87134	0.96481	0.32165
H	0.87983	0.04879	0.82675
H	0.87479	0.44622	0.32098
H	0.89376	0.58352	0.84747
H	0.37138	0.27509	0.19307
H	0.3631	0.16491	0.68487
H	0.37275	0.77538	0.19391
H	0.33772	0.64118	0.69093
H	0.86926	0.27674	0.19139
H	0.86464	0.15313	0.69449
H	0.87218	0.77581	0.19437

H	0.84014	0.64111	0.68231
H	0.1233	0.20533	0.31868
H	0.12836	0.2903	0.82683
H	0.12899	0.69077	0.32153
H	0.14131	0.69583	0.84506
H	0.62185	0.19907	0.32156
H	0.62438	0.31207	0.82886
H	0.6275	0.69798	0.32249
H	0.63627	0.69151	0.8401
Ow	0.07896	0.2139	0.19086
Ow	0.08189	0.21956	0.6934
Ow	0.07866	0.73488	0.19462
Ow	0.07667	0.71358	0.68671
Ow	0.57972	0.21181	0.1909
Ow	0.58205	0.21431	0.69333
Ow	0.5744	0.71974	0.18779
Ow	0.59363	0.75746	0.71016
Ow	0.41787	0.25425	0.32445
Ow	0.41631	0.25905	0.82048
Ow	0.41023	0.7774	0.32095
Ow	0.41924	0.7485	0.82752
Ow	0.91684	0.25835	0.32246
Ow	0.91976	0.27207	0.82575
Ow	0.9164	0.77752	0.32682
Ow	0.91816	0.74796	0.82712
Ow	0.32677	0.48579	0.19401
Ow	0.32671	0.50934	0.69236
Ow	0.32827	0.96581	0.19065
Ow	0.33036	0.95744	0.6946
Ow	0.82663	0.48181	0.19184
Ow	0.82654	0.50843	0.69218
Ow	0.82908	0.96306	0.19164
Ow	0.8297	0.95985	0.69035
Ow	0.16558	0.01397	0.32192
Ow	0.16279	0.05348	0.82169
Ow	0.1671	0.49022	0.32021
Ow	0.16886	0.49471	0.826
Ow	0.66531	0.01088	0.32384
Ow	0.67149	0.01204	0.82946
Ow	0.67025	0.49096	0.32128
Ow	0.66724	0.50716	0.82941
Hw	0.12209	0.21963	0.17901
Hw	0.12606	0.21312	0.68443
Hw	0.12249	0.72991	0.1847

Hw	0.12183	0.7128	0.68438
Hw	0.62321	0.21399	0.17954
Hw	0.62661	0.21236	0.68632
Hw	0.61965	0.7197	0.18728
Hw	0.62553	0.73331	0.67776
Hw	0.37406	0.25085	0.33412
Hw	0.37232	0.2575	0.83002
Hw	0.36968	0.75946	0.33531
Hw	0.38451	0.73586	0.7905
Hw	0.87319	0.26031	0.33338
Hw	0.88476	0.23749	0.79472
Hw	0.87368	0.75618	0.33043
Hw	0.87311	0.75436	0.82948
Hw	0.37131	0.48413	0.18686
Hw	0.36071	0.50861	0.7292
Hw	0.37229	0.97223	0.18217
Hw	0.37472	0.95807	0.68713
Hw	0.87125	0.4792	0.18523
Hw	0.85913	0.50908	0.73072
Hw	0.87272	0.96605	0.18086
Hw	0.87485	0.96792	0.69058
Hw	0.12315	0.00815	0.33585
Hw	0.11988	0.03352	0.8258
Hw	0.12337	0.49277	0.33087
Hw	0.13718	0.47417	0.78613
Hw	0.62271	0.00691	0.33788
Hw	0.62616	0.01178	0.82477
Hw	0.62543	0.49699	0.32458
Hw	0.63819	0.48185	0.78768
Hw	0.06993	0.14434	0.18444
Hw	0.07101	0.16449	0.71349
Hw	0.0773	0.77961	0.24088
Hw	0.06815	0.69175	0.72968
Hw	0.56873	0.14367	0.18882
Hw	0.57883	0.19657	0.73915
Hw	0.56222	0.6634	0.20558
Hw	0.61174	0.74389	0.7555
Hw	0.42958	0.32284	0.33211
Hw	0.42066	0.30627	0.79087
Hw	0.40696	0.84729	0.32224
Hw	0.44849	0.79157	0.81208
Hw	0.93026	0.32521	0.32435
Hw	0.94158	0.3051	0.79507
Hw	0.91364	0.84621	0.32453

Hw	0.92406	0.70752	0.78059
Hw	0.32213	0.53153	0.23913
Hw	0.29001	0.52481	0.71854
Hw	0.32009	0.89654	0.18714
Hw	0.32766	0.93634	0.73927
Hw	0.82148	0.53059	0.23535
Hw	0.78937	0.5277	0.71668
Hw	0.81895	0.89406	0.18679
Hw	0.82232	0.94461	0.73605
Hw	0.17533	0.08338	0.32883
Hw	0.1649	0.12399	0.83927
Hw	0.16741	0.45136	0.27178
Hw	0.19958	0.53538	0.81033
Hw	0.67459	0.08013	0.32859
Hw	0.68623	0.043	0.79298
Hw	0.67582	0.44458	0.27671
Hw	0.69948	0.54565	0.81405
Ca	0.1861	0.02781	0.46735
Ca	0.18344	0.04702	0.96135
Ca	0.18575	0.5272	0.46296
Ca	0.18255	0.54227	0.95781
Ca	0.6849	0.02854	0.46619
Ca	0.68386	0.03987	0.95705
Ca	0.68589	0.52743	0.45929
Ca	0.68223	0.5441	0.9598
Ca	0.31014	0.44714	0.05475
Ca	0.31484	0.43394	0.5605
Ca	0.30939	0.94993	0.05342
Ca	0.31011	0.93239	0.55848
Ca	0.81029	0.44742	0.05604
Ca	0.81314	0.43122	0.5588
Ca	0.80987	0.94564	0.05163
Ca	0.81057	0.932	0.55895
Ca	0.43711	0.27774	0.46714
Ca	0.43489	0.29265	0.96181
Ca	0.43415	0.78075	0.46459
Ca	0.43074	0.79334	0.95749
Ca	0.93645	0.27518	0.4649
Ca	0.93337	0.28981	0.95813
Ca	0.9351	0.7785	0.46147
Ca	0.93387	0.7926	0.95826
Ca	0.05935	0.19752	0.05077
Ca	0.06351	0.18063	0.558
Ca	0.05943	0.69611	0.05083

Ca	0.06034	0.68112	0.55374
Ca	0.56029	0.19843	0.05332
Ca	0.56274	0.18264	0.55861
Ca	0.55914	0.69903	0.05653
Ca	0.56052	0.68058	0.54805
Cw	0.24793	0.25153	0.25963
Cw	0.25051	0.27711	0.75918
Cw	0.24584	0.75616	0.25917
Cw	0.24274	0.76659	0.76135
Cw	0.74902	0.21893	0.25527
Cw	0.74938	0.27641	0.76221
Cw	0.74548	0.75942	0.2605
Cw	0.7458	0.76506	0.75848
Cw	0.99673	0.00805	0.25994
Cw	0.99806	0.93993	0.75894
Cw	0.99744	0.50035	0.25752
Cw	0.99547	0.50336	0.75414
Cw	0.50308	0.96323	0.25492
Cw	0.49834	0.00697	0.76117
Cw	0.49853	0.46872	0.25568
Cw	0.50024	0.52671	0.75712
Ca	0.18189	0.2774	0.45888
Ca	0.17953	0.29658	0.95999
Ca	0.17826	0.77887	0.46062
Ca	0.17819	0.80041	0.96875
Ca	0.68179	0.27744	0.45851
Ca	0.67922	0.29772	0.96027
Ca	0.67919	0.78038	0.45902
Ca	0.67796	0.79697	0.96683
Ca	0.31708	0.19483	0.05454
Ca	0.31898	0.18001	0.55445
Ca	0.31339	0.69607	0.0564
Ca	0.31636	0.67823	0.55035
Ca	0.81601	0.19291	0.05379
Ca	0.81732	0.17246	0.54752
Ca	0.81422	0.69535	0.05604
Ca	0.81549	0.6771	0.54831
Ca	0.42958	0.03198	0.46598
Ca	0.42786	0.04648	0.96307
Ca	0.43042	0.52839	0.45484
Ca	0.42899	0.54881	0.97122
Ca	0.93096	0.031	0.46647
Ca	0.92833	0.0446	0.96448
Ca	0.92979	0.52769	0.45669

Ca	0.93012	0.54349	0.96628
Ca	0.06654	0.44307	0.05339
Ca	0.06633	0.42653	0.54451
Ca	0.06536	0.94769	0.05866
Ca	0.06738	0.92955	0.55808
Ca	0.5656	0.44642	0.05597
Ca	0.56827	0.42515	0.54269
Ca	0.56436	0.94536	0.05306
Ca	0.5664	0.93117	0.5565

Appendix Reference

1. Moore, A.E. & Taylor, H.F.W. Crystal structure of ettringite. *Acta Crystallogr. Sec. B*, **26**, 386-393 (1970).
2. Comodi, P., Nazzareni, S., Zanazzi, P.F. & Speziale, S. High-pressure behavior of gypsum: A single-crystal X-ray study. *Am. Miner.* **93**, 1530-1537 (2008).
3. Mondal, P. & Jeffery, J.W. The crystal structure of tricalcium aluminate, $\text{Ca}_3\text{Al}_2\text{O}_6$. *Acta Crystallogr. Sec. B*, **31**, 689-697 (1975).
4. Lutterotti, L., Matthies, S. & Wenk, H.-R. MAUD: a friendly Java program for material analysis using diffraction. *IUCr: Newsletter of the CPD*, **21**, 14-15 (1999).
5. Brisard, S., *et al.* Morphological quantification of hierarchical geomaterials by X-ray nano-CT bridges the gap from nano to micro length scales. *Am. Mineral.* **97**, 480-483 (2012).
6. Kak, A.C. & Slaney, M. *Principles of Computerized Tomographic Imaging* (Society for Industrial and Applied Mathematics, Philadelphia, 2001).
7. Hammouda, B. A new Guinier-Porod model. *J. Appl. Cryst.* **43**, 716-719 (2010).
8. Brandt, S. *in Electron Tomography Ch. 3* (J. Frank, Ed. Springer New York, 2006).
9. Gordon, R., Bender, R. & Herman, G. T. Algebraic Reconstruction Techniques (ART) for three-dimensional electron microscopy and X-ray photography. *J. Theor. Biol.* **29**, 471-481 (1970).
10. Deng, J., *et al.* Simultaneous cryo X-ray ptychographic and fluorescence microscopy of green algae. *Proc. Natl. Acad. Sci.* **112**, 2314-2319 (2015).
11. Van Heel, M. & Schatz, M. Fourier shell correlation threshold criteria. *J. Struct. Biol.* **151**, 250-262 (2005).
12. Vespa, M., Wieland, E., Dähn, R., Grolimund, D. & Scheidegger, A.M. Determination of the elemental distribution and chemical speciation in highly heterogeneous cementitious materials using synchrotron-based micro-spectroscopic techniques. *Cem. Concr. Res.* **37**, 1473-1482 (2007).
13. Lutterotti, L., Matthies, S. & Wenk, H. R. MAUD: a friendly Java program for material analysis using diffraction. *IUCr: Newsletter of the CPD*. **21**, 14-15 (1999).
14. Lutterotti, L. & Scardi, P. Profile fitting by the interference function. *Adv. X-Ray Anal.* **35**, 577-584 (1991).
15. Shahsavari, R., Pellenq, R. J. M. and Ulm, F. J. Empirical force fields for complex hydrated calcio-silicate layered materials. *Phys. Chem. Chem. Phys.* **13**, 1002-1011 (2011).

16. Cygan, R. T., Liang, J. J. & Kalinichev, A. G. Molecular models of hydroxide, oxyhydroxide, and clay phases and the development of a general force field. *J. Phy. Chem. B*, **108**, 1255-1266 (2004).
17. Wu, Y., Tepper, H. L. & Voth, G. A. Flexible simple point-charge water model with improved liquid-state properties. *J. Chem. Phy.* **124**, 024503 (2006)
18. Wolf, D., Keblinski, P., Phillpot, S. R. & Eggebrecht, J. Exact method for the simulation of Coulombic systems by spherically truncated, pairwise r^{-1} summation. *J. Chem. Phy.* **110**, 8254-8282 (1999).
19. Merlino, S., Bonaccorsi, E. & Armbruster, T. The real structures of clinotobermorite and tobermorite 9 Å OD character, polytypes, and structural relationships. *Eur. J. Mineral.* **12**, 411-429 (2000).
20. Hamid, S. A. The crystal structure of the 11 Å natural tobermorite $\text{Ca}_{2.25}[\text{Si}_3\text{O}_{7.5}(\text{OH})_{1.5}] \cdot \text{H}_2\text{O}$. *Z. Kristallogr. Cryst. Mater.* **154**, 189-198 (1981).
21. Merlino, S., Bonaccorsi, E. & Armbruster, T. Tobermorites: their real structure and order-disorder (OD) character. *Am. Mineral.* **84**, 1613-1621 (1999).
22. Merlino, S., Bonaccorsi, E. & Armbruster, T. The real structure of tobermorite 11 Å normal and anomalous forms, OD character and polytypic modifications. *Eur. J. Mineral.* **13**, 577-590 (2001).
23. Bonaccorsi, E., Merlino, S. & Kampf, A. R. The crystal structure of tobermorite 14 Å (Plombierite), a C-S-H phase. *J. Am. Ceram. Soc.* **88**, 505–512 (2005).
24. L'Hôpital, E., Lothenbach, B., Kulik, D. A. & Scrivener, K. Influence of calcium to silica ratio on aluminium uptake in calcium silicate hydrate. *Cem. Concr. Res.* **85**, 111-121 (2016).
25. Pegado, L., Labbez, C. & Churakov, S.V. Mechanism of aluminium incorporation into C–S–H from ab initio calculations. *J. Mat. Chem. A* **2**, 3477-3483 (2014).
26. Richardson, I. G. Model structures for C-(A)-S-H (I). *Acta Crystallogr. Sect. B.* **70**, 903-923 (2014).
27. Alizadeh, R., Beaudoin, J. J. and Raki, L. C–S–H (I)—A Nanostructural Model for the Removal of Water from Hydrated Cement Paste? *J. Am. Ceram. Soc.* **90**, 670-672 (2007).
28. Keen, D. A. A comparison of various commonly used correlation functions for describing total scattering. *J. App. Cryst.* **34**, 172-177 (2001).
29. Chung, J. S. & Thorpe, M. F. Local atomic structure of semiconductor alloys using pair distribution functions. *Phy. Rev. B*, **55**, 1545 (1997).
30. Gale, J. D. GULP: A computer program for the symmetry-adapted simulation of solids. *J. Chem. Soc., Faraday Trans.* **93**, 629-637 (1997).